

**ON THE INTERPLAY BETWEEN MICROKINETICS AND  
TURBULENCE IN SPACE PLASMAS**

by

Ramiz Ahmad Qudsi

A dissertation submitted to the Faculty of the University of Delaware in partial fulfillment of the requirements for the degree of Doctor of Philosophy in Physics

Summer, 2021

© 2021 Ramiz Ahmad Qudsi  
All Rights Reserved



**ON THE INTERPLAY BETWEEN MICROKINETICS AND  
TURBULENCE IN SPACE PLASMAS**

by

Ramiz Ahmad Qudsi

Approved: \_\_\_\_\_

Edmund R. Nowak, Ph.D.  
Chair of the Department of Physics and Astronomy

Approved: \_\_\_\_\_

John A. Pelesko, Ph.D.  
Dean of the College of Arts and Sciences

Approved: \_\_\_\_\_

Louis F. Rossi, Ph.D.  
Vice Provost for Graduate and Professional Education and  
Dean of the Graduate College

I certify that I have read this dissertation and that in my opinion it meets the academic and professional standard required by the University as a dissertation for the degree of Doctor of Philosophy.

Signed: \_\_\_\_\_

Bennett A. Maruca, Ph.D.  
Professor in charge of dissertation

I certify that I have read this dissertation and that in my opinion it meets the academic and professional standard required by the University as a dissertation for the degree of Doctor of Philosophy.

Signed: \_\_\_\_\_

Daniel Verscharen, Ph.D.  
Member of dissertation committee

I certify that I have read this dissertation and that in my opinion it meets the academic and professional standard required by the University as a dissertation for the degree of Doctor of Philosophy.

Signed: \_\_\_\_\_

Michael A. Shay, Ph.D.  
Member of dissertation committee

I certify that I have read this dissertation and that in my opinion it meets the academic and professional standard required by the University as a dissertation for the degree of Doctor of Philosophy.

Signed: \_\_\_\_\_

Véronique Petit, Ph.D.  
Member of dissertation committee

I certify that I have read this dissertation and that in my opinion it meets the academic and professional standard required by the University as a dissertation for the degree of Doctor of Philosophy.

Signed: \_\_\_\_\_

William H. Matthaeus, Ph.D.

Member of dissertation committee



## ACKNOWLEDGEMENTS

I would like to thank my thesis supervisor, Dr. Bennett Maruca, for his constant support and understanding during the whole duration of my graduate education. He has been a source of inspiration and encouragement.

I would like to thank my colleagues in the department with whom I have had innumerable discussions on all topics, academic and otherwise. A lot of ideas presented in this thesis originated during one of those discussions. Coffee-shop meetings with Dr. Bill Matthaeus was THE place for such discussion. I am especially indebted to Tulasi Parashar and Rohit Chhiber, who were always very patient while explaining nuances of plasma physics to me. Alexandros Chasapis was always encouraging and informative as we discussed the subtleties of multi-spacecraft techniques. Discussion with Riddhi, Mark, Debanjan, and Manuel were always animated, fun, educational and diverse. I am specially indebted to Bill and Riddhi who always took time to explain finer points of turbulence. I am so glad to have been part of such a dynamic and diverse group.

I feel lucky to have had the chance to work with Dr. Peter Gary who was always excited about the kind of work we were doing. His comments on our results were always insightful and encouraging and his enthusiasm for discussion was contagious. He will be fondly remembered and dearly missed!

I am very thankful to the MMS and PSP teams for giving me the opportunity and most importantly data to work with.

Life in Newark was filled with fun and I depart here with lots and lots of memories. Thanks to all my friends who contributed to the joy of living there. Siddhi, Sucharita, Mehul, Abdul, Sameer, Mark, Khushboo, Aditya, Abhishek, Prasanna, Anitha, Vrathasha; thank you all for making my stay so much enjoyable.

Special thanks to Krishna who has been supportive and understanding throughout thesis writing process and helped in typing a not so insignificant part of this thesis.

I would also like to thank the staff of the Department of Physics and Astronomy, especially Maura, Elle, Angie and Linda, who have been extremely helpful over the years and very proactive in solving my non-academic issues. Sansern Somboonsong and Zelphia Johnson were always very responsive to my queries regarding the computer and network.

I would like to thank my family, who despite their own biases against science, have largely been supportive my own endeavors in the field.

And lastly I would like to thank my dear friend Abhishek Maniyar. I decided to leave my job, and a good job it was, because he insisted that I should and pursue my dream of a PhD in Physics. He guided me through the whole process and I am extremely thankful to him for making me do that. Thank you Maniyar for being the force behind this!

This research made use of PlasmaPy, a community-developed open source Python package for plasma science ([PlasmaPy Community, 2020](#)). I extensively used the SAO/-NASA [Astrophysics Data System \(ADS\)](#) in the preparation of this dissertation.

## TABLE OF CONTENTS

<b>LIST OF TABLES . . . . .</b>	<b>xi</b>
<b>LIST OF FIGURES . . . . .</b>	<b>xii</b>
<b>ABSTRACT . . . . .</b>	<b>xiv</b>
Chapter	
<b>1 INTRODUCTION . . . . .</b>	<b>1</b>
1.1 Prologue to Plasma . . . . .	1
1.2 Introduction To Plasma . . . . .	1
1.3 Plasma in Near-Earth Environment . . . . .	5
1.4 Studying Space Plasmas . . . . .	7
1.5 In This Thesis . . . . .	9
<b>2 KINETIC THEORY AND LINEAR MICROKINETIC INSTABILITIES . . . . .</b>	<b>11</b>
2.1 Introduction to Plasma Kinetic Theory . . . . .	11
2.1.1 Equations of motion . . . . .	11
2.1.2 Distribution Function and Other Definitions . . . . .	14
2.2 Linear Microkinetic Instabilities . . . . .	17
2.2.1 The Linear Dispersion Relation . . . . .	17
2.2.2 Temperature Anisotropy Induced Instabilities . . . . .	20
2.2.3 Computing Growth Rates . . . . .	21
2.3 Application of linear theory and observational evidence . . . . .	22
2.4 Limitations of linear theory . . . . .	28
<b>3 NON-LINEAR PLASMA DYNAMICS . . . . .</b>	<b>31</b>
3.1 Introduction to Turbulence . . . . .	31

3.2	Consequences of Turbulence in Space Plasmas . . . . .	32
3.2.1	Heating of plasma . . . . .	33
3.2.2	Anisotropy . . . . .	34
3.2.3	Intermittency . . . . .	35
3.3	Linear and Non-linear Time Scales . . . . .	35
<b>4</b>	<b>DATASETS AND ANALYSIS METHODS . . . . .</b>	<b>37</b>
4.1	Spacecraft datasets . . . . .	37
4.1.1	Wind . . . . .	37
4.1.2	MMS . . . . .	39
4.1.3	PSP . . . . .	40
4.2	Simulation datasets . . . . .	42
4.2.1	MHD Simulations . . . . .	42
4.2.2	Hybrid Simulations . . . . .	42
4.2.3	Kinetic Simulations . . . . .	42
<b>5</b>	<b>ASSOCIATION OF INTERMITTENCY AND MICROINSTABILITIES . . . . .</b>	<b>47</b>
5.1	Overview . . . . .	47
5.2	Introduction . . . . .	48
5.3	Data and Analysis . . . . .	48
5.3.1	PIC Simulation . . . . .	48
5.3.2	Space Observations . . . . .	49
5.4	Results . . . . .	50
5.4.1	PIC simulation . . . . .	50
5.4.2	Spacecraft Observations . . . . .	54
5.5	Discussions . . . . .	59
<b>6</b>	<b>TEMPERATURE ENHANCEMENT ALONG INTERMITTENT STRUCTURES . . . . .</b>	<b>63</b>
6.1	Overview . . . . .	63

6.2	Introduction . . . . .	63
6.3	Background . . . . .	65
6.4	Data Selection and Methodology . . . . .	66
6.5	Results . . . . .	68
6.6	Discussions . . . . .	74
<b>7</b>	<b>INTERPLAY BETWEEN LINEAR AND NON-LINEAR PROCESSES . . . . .</b>	<b>77</b>
7.1	Overview . . . . .	77
7.2	Introduction . . . . .	77
7.3	Data Selection and Methodology . . . . .	78
7.4	Results . . . . .	79
7.5	Discussions . . . . .	88
<b>8</b>	<b>MAGNETIC FIELD TOPOLOGY RECONSTRUCTION USING MACHINE LEARNING ALGORITHM . . . . .</b>	<b>93</b>
8.1	Overview . . . . .	93
8.2	Introduction . . . . .	93
8.3	Background . . . . .	95
8.3.1	Gaussian Processes Regression . . . . .	95
8.4	Kernels in Gaussian Processes . . . . .	97
8.5	Synthetic Data Generation . . . . .	99
8.6	Methodology . . . . .	100
8.7	Results . . . . .	102
8.8	Discussions . . . . .	105
<b>9</b>	<b>CONCLUSION . . . . .</b>	<b>111</b>
9.1	Broader Context . . . . .	111
9.2	Summary of Key Results . . . . .	112
<b>BIBLIOGRAPHY . . . . .</b>		<b>117</b>
<b>Appendix</b>		
<b>A BRAZIL PLOTS . . . . .</b>		<b>135</b>
<b>B CGL INVARIANTS . . . . .</b>		<b>141</b>
<b>C GAUSSIAN PROCESSES ALGORITHM . . . . .</b>		<b>143</b>
<b>D PERMISSION LETTER . . . . .</b>		<b>146</b>

## LIST OF TABLES

1.1	Plasma Parameters - Median values . . . . .	9
2.1	Microkinetic instabilities . . . . .	21
4.1	mms dataset details . . . . .	45
4.2	Datasets used in this study . . . . .	46
5.1	Average value of parameters for datasets . . . . .	58
7.1	Dataset detail for $\Gamma_{\max}$ and $\omega_{nl}$ . . . . .	85

## LIST OF FIGURES

1.1	Plasma parameter distributions at 1 au . . . . .	6
1.2	Earth's Magnetosphere's structure . . . . .	8
2.1	Temperature distribution at 1 au . . . . .	23
2.2	$R_p$ distribution at 1 au and in magnetosheath . . . . .	24
2.3	$\gamma$ Contours . . . . .	25
2.4	Brazil-plot at 1 au . . . . .	26
2.5	Brazil-plot in magnetosheath . . . . .	27
5.1	Plot of $\beta_{\parallel p}$ , $R_p$ , $J_z$ and $\gamma$ for <b>149p6</b> dataset . . . . .	51
5.2	Plot of $\beta_{\parallel p}$ , $R_p$ , $J_z$ and $\gamma$ for <b>kaw</b> dataset . . . . .	52
5.3	Plot of $\beta_{\parallel p}$ , $R_p$ , $J_z$ and $\gamma$ for <b>ros</b> dataset . . . . .	53
5.4	Time series plot of $\beta_{\parallel p}$ , $R_p$ , $J_z$ and $\gamma$ for <b>mms</b> dataset . . . . .	55
5.5	Time series plot of $\beta_{\parallel p}$ , $R_p$ , $J_z$ and $\gamma$ for <b>wnd</b> dataset . . . . .	56
5.6	Spacecraft and simulation comparison of $\gamma$ time series . . . . .	57
6.1	$\mathcal{I}$ comparisons for different $\tau$ . . . . .	67
6.2	Joint histogram of $T_{\parallel p}$ and $\mathcal{I}$ . . . . .	69
6.3	PDF of $T_{\parallel p}$ for various $\mathcal{I}$ for <b>psp</b> dataset . . . . .	70
6.4	PDF of $T_{\parallel p}$ for various $\mathcal{I}$ for <b>mms</b> dataset . . . . .	71
6.5	Conditionally averaged $T_{\parallel p}$ from a $\mathcal{I}$ event . . . . .	73

7.1	Comparison plot of $\Gamma_{\max}$ , $\omega_{\text{nl}}$ and $\Gamma_{\max}/\omega_{\text{nl}}$ for simulations . . . . .	81
7.2	Comparison plot of $\Gamma_{\max}$ , $\omega_{\text{nl}}$ and $\Gamma_{\max}/\omega_{\text{nl}}$ for <b>mms</b> dataset . . . . .	82
7.3	Comparison plot of $\Gamma_{\max}$ , $\omega_{\text{nl}}$ and $\Gamma_{\max}/\omega_{\text{nl}}$ for <b>wnd</b> dataset . . . . .	83
7.4	Comparison plot of $\Gamma_{\max}$ , $\omega_{\text{nl}}$ and $\Gamma_{\max}/\omega_{\text{nl}}$ for <b>psp</b> dataset . . . . .	84
7.5	KDE plots for all six datasets . . . . . . . . .	87
7.6	$(R_p, \beta_{\parallel p})$ -plot of $\Gamma_{\max}$ , $\omega_{\text{nl}}$ and $\Gamma_{\max}/\omega_{\text{nl}}$ for <b>mms</b> dataset . . . . .	89
7.7	$(R_p, \beta_{\parallel p})$ -plot of $\Gamma_{\max}$ , $\omega_{\text{nl}}$ and $\Gamma_{\max}/\omega_{\text{nl}}$ for <b>wnd</b> dataset . . . . .	90
7.8	$(R_p, \beta_{\parallel p})$ -plot of $\Gamma_{\max}$ , $\omega_{\text{nl}}$ and $\Gamma_{\max}/\omega_{\text{nl}}$ for <b>psp</b> dataset . . . . .	91
8.1	Configuration for 24 spacecraft . . . . . . . . .	101
8.2	Reconstructed field (x-component), linear configuration . . . . .	103
8.3	Reconstructed field (y-component), linear configuration . . . . .	104
8.4	Reconstructed field (z-component), linear configuration . . . . .	105
8.5	Reconstructed field, linear configuration . . . . .	106
8.6	Reconstructed field (x-component), circular configuration . . . . .	106
8.7	Reconstructed field (y-component), circular configuration . . . . .	107
8.8	Reconstructed field (z-component), circular configuration . . . . .	107
8.9	Reconstructed field, circular configuration . . . . .	108
A.1	Brazil-plot of <b>149p6</b> dataset . . . . . . . . .	136
A.2	Brazil-plot of <b>kaw</b> dataset . . . . . . . . .	137
A.3	Brazil-plot of <b>2dsim</b> dataset . . . . . . . . .	138
A.4	Brazil-plot of <b>ros</b> dataset . . . . . . . . .	139
A.5	Brazil-plot of <b>psp</b> dataset . . . . . . . . .	140

## ABSTRACT

Space plasmas in the inner heliosphere exist in a weakly collisional and turbulent state. Though energy transfer from large scales to smaller scales by turbulent cascade is widely accepted as an important feature of space plasmas, details of its exact dissipation process are lacking. Features arising because of turbulence, such as intermittency and temperature anisotropy, play important roles in the dynamics of space plasmas. Microkinetic linear instabilities induced by temperature anisotropy have been shown to change the statistical characteristics of plasma in a significant way.

Since the two processes, turbulence cascade and microkinetic instabilities, occur in the same physical and phase space, there is an interplay at work. In this study we investigated this interplay and the subsequent competition arising between the two, linear and nonlinear, processes. We found an explicit connection between intermittency and linear instability growth rates. We also showed localization of temperature enhancement regions along the intermittent structures, which in turn can trigger linear instabilities. Investigation of the two processes shed light on why linear theory works as well as it does, and shows the complicated nature of their interplay.

Information related to the exact spatial structure of the interplanetary magnetic field is vital to our understanding of the type of turbulence active in the space plasmas and the mechanism of turbulence cascade. This will help us discern the interplay between the two processes. We thus also report on a proof of concept study of magnetic field topology reconstruction using Gaussian Processes in machine learning.



اقرأ باسم ربك  
الذي علم البشر ما لم تعرفه  
ومنه علمًا بما لا تعلم  
وأعطاه حب الاستطلاع ليجد ما لا يعرفه  
وأعطاه حب التحقيق ليكتشفوا ويكتشفوا  
ما يكمن في الظل وأين يذهب النرد عندما يلعبها الآلهة!

Read, in the name of your God.  
Who taught mankind what they knew not.  
And gave them cognizance that they know not.  
And gave them curiosity so they may find what they know not.  
And gave them inquisitiveness so they may question and discover.  
What lies in the shadow and where do the dice go when Gods play them!



# Chapter 1

## INTRODUCTION

### 1.1 Prologue to Plasma

Our daily life is dominated by our interactions with the three classical states of matter: solid, liquid and gas. Plasma is the fourth state of matter and by far the most abundant one. In fact the observable universe is almost entirely made up of plasma (99.9% of the universe) ([Boulos et al., 1994](#)). From the HII region around a huge star to the surface of a star, from the super hot Inter Galactic Medium to the inside of a plasma TV, plasma is everywhere. Given its abundance and ubiquitous nature, it becomes vitally important to study and understand plasma. In the rest of this chapter we define what constitutes a plasma (Section [1.2](#)) and discuss some of its salient properties and the laws of physics that govern it. We also shed some light on the local regions around Earth that are made up of plasma (Section [1.3](#)) and discuss studying them (Section [1.4](#)). We conclude the chapter with with a brief discussion of topics covered in this thesis. (Section [1.5](#)).

### 1.2 Introduction To Plasma

The term “plasma” comes from the ancient Greek word “πλάσμα” that means something that is moldable. It was first used in the modern context by [Langmuir \(1928\)](#) to describe the “region (around electrodes) containing balanced charges of ion and electrons”.

A plasma is a sub-type of ionized gas; a gas where significant fraction of the atoms have been ionized. There are specific criteria that distinguishes plasmas from other ionized gases (discussed later in this section), but first we consider the equations that govern the dynamics of charged particles (electrons and ions).

As is with everything that has mass in the universe, a plasma's dynamics is governed by Newton's equation of motion:

$$\mathbf{F}_{\text{net}} = \frac{d\mathbf{P}}{dt} = m \frac{d^2\mathbf{x}}{dt^2} \quad (1.1)$$

where  $\mathbf{F}_{\text{net}}$  is the net external force acting on the system and  $\mathbf{P}$  is its momentum.  $t$  is time,  $\mathbf{x}$  is the position vector and  $\frac{d}{dt}$  is the derivative with respect to time.

For a charged particle with charge  $q$ , moving with velocity  $\mathbf{v}$  in an electromagnetic field with electric and magnetic field as  $\mathbf{E}$  and  $\mathbf{B}$  respectively, the electromagnetic force or Lorentz force is given as:

$$\mathbf{F}_{\text{EM}} = q(\mathbf{E} + \mathbf{v} \times \mathbf{B}) \quad (1.2)$$

These equations (Equations (1.1) to (1.2)) coupled with the four Maxwell's equations (Equations (1.3) to (1.6)) define the complete dynamics of a plasma.

$$\nabla \cdot \mathbf{E} = \frac{\rho}{\epsilon_0} \quad (1.3)$$

$$\nabla \cdot \mathbf{B} = 0 \quad (1.4)$$

$$\nabla \times \mathbf{E} = -\frac{\partial \mathbf{B}}{\partial t} \quad (1.5)$$

$$\nabla \times \mathbf{B} = \mu_0 \mathbf{J} + \frac{1}{c^2} \frac{\partial \mathbf{E}}{\partial t} \quad (1.6)$$

where,  $\rho$  is the charge density,  $\epsilon_0$  is the permittivity of free space,  $\frac{\partial}{\partial t}$  is the partial derivative with respect to time,  $\mathbf{J}$  is the current density, and  $c$  is the speed of light in vacuum.

The most accurate way to study the behaviour of plasma is to track each particle individually using Equations (1.1) to (1.6), all while accounting for all the fields, external as well as those arising because of the charge and motion of particles themselves. However, that method is almost impossible to implement not only because of difficulty in computing the field arising because of mutual interactions but also because

---

<sup>1</sup>  $\mathbf{F}_{\text{net}} = m \frac{d^2\mathbf{x}}{dt^2}$  is only valid when the particle is moving at speed much smaller than the speed of light.

of the huge number of particles involved. Consequently, scientists often fall back to statistical methods in their studies, such as applying kinetic equations that use physics based on ensemble averages (see Chapter 2) or by approximating the plasma as a fluid as is done in Magneto-hydrodynamics (MHD).

Since even the lightest ion, a proton, is nearly 2000 times more massive than an electron and the dynamics of particles are often governed by their masses, both the time and length scales at which dynamics occur in plasmas are extremely diverse, even when one is studying the same phenomena for ions and electrons. Values of some of the parameters associated with plasma (generally referred to as *plasma parameters*) can help in understanding the scales one is dealing with. Also, as will become apparent in Chapters 2 and 3, one may choose to focus on a specific scale depending on the interest or scope of the study. Here, we list some of the most relevant plasma parameters, what each one of them mean, and their mathematical expressions.

**Debye Length ( $\lambda_D$ ):** The Debye length is the scale above which a plasma (with no net charge) maintains near charge neutrality —  $\rho \approx 0$  when  $\rho$  is smoothed over a scale  $\gtrsim \lambda_D$ . On scales smaller than  $\lambda_D$ , particles behave as if it were interacting with other moving charges individually instead of a smooth macroscopic electromagnetic field. If we have sufficiently large number of particles inside a spherical volume with  $\lambda_D$  as the radius ( $n_p \lambda_D^3 > 1$ ), then particles are shielded by its neighbours from the surrounding plasma (called *Debye shielding*). On scales  $\lesssim \lambda_D$ , random thermal motions of the particles give rise to isolated regions of non-zero charge density. We would then expect  $\lambda_D$  to increase with plasma temperature. Indeed, for a plasma consisting of ionized hydrogen for which the protons and electrons have comparable temperatures, we define Debye length as:

$$\lambda_D = \frac{\epsilon_0 k_B T_p}{n_e e^2}^{1/2} \quad (1.7)$$

where  $k_B$  is the Boltzmann constant,  $n_e$  is the electron number density and  $T_p$  is the proton temperature. In order for a system to be classified as plasma, we must have the

physical length scale ( $L$ ) of the system much larger than its Debye length.

$$\lambda_D \ll L \quad (1.8)$$

**Ion-inertial Length ( $d_j$ ):** This is the length scale in plasma at which the electrons are decoupled from ions and the magnetic field is frozen in with the electrons. For species ‘ $j$ ’ of plasma (where  $j = p^+$  for protons and  $j = i^{n+}$  for any other ion with  $n$  positive charge)<sup>2</sup>, it can be written in terms of ion plasma frequency ( $\omega_{pj}$ ) as:

$$d_j = \frac{c}{\omega_{pj}} \quad (1.9)$$

**Plasma Frequency ( $\omega_{pj}$ )<sup>3</sup>:** It is the frequency at which any given species in plasma oscillates and is given by:

$$\omega_{pj} = \left( \frac{n_j q_j^2}{\epsilon_0 m_j} \right)^{\frac{1}{2}} \quad (1.10)$$

**Cyclotron Frequency ( $\Omega_{cj}$ ):** In a magnetized plasma (a plasma which has a background magnetic field), due to the perpendicular direction of the magnetic force with respect to the particle’s velocity, any non-stationary charged particle in a magnetic field gyrates around a point called the center of gyration. The frequency of gyration or cyclotron frequency is given by:

$$\Omega_{cj} = \frac{q_j B}{m_j} \quad (1.11)$$

where  $\mathbf{B}$  is the background magnetic field.

---

**Gyroradius ( $\rho_j$ ):** This is the radius of the circular path that a particle takes in

<sup>2</sup> In this thesis unless otherwise specified ion will refer to protons and two terms will be used interchangeably

<sup>3</sup> Note that ‘p’ in  $\omega_{pj}$  refers to plasma and not proton.

the presence of a magnetic field, and is dependent on the ratio of thermal speed to that of cyclotron frequency.

$$\rho_j = \frac{w_j}{\Omega_{cj}} \quad (1.12)$$

where  $w_j$  is the thermal speed of the particle.

**Alfvén Speed ( $V_{Aj}$ ):** It is the speed at which magnetic signals, like a fluctuation in the field, travel in a plasma. It depends on the strength of the magnetic field in the plasma as well the density and mass of the species and has the following expression:

$$v_{Aj} = \frac{B}{\sqrt{\mu_0 \sum_j n_j m_j}} \quad (1.13)$$

### 1.3 Plasma in Near-Earth Environment

The Sun is the largest source of plasma in our solar system. Huge amounts of charged particles emanate from the Sun originating in its outermost atmospheric layer, called the Corona (Parker, 1958, 1960, 1963; Gringauz et al., 1960; Neugebauer & Snyder, 1962). This constant outflow of particles is commonly called solar wind. The solar wind is often highly magnetized, is weakly collisional, travels at supersonic speed and is primarily composed of ionized hydrogen (i.e., protons) (Marsch et al., 1982a). Table 1.1 lists out some of the plasma parameters and their typical values for the solar wind at 1 au. Figure 1.1 shows the distribution of some of the parameters listed in Table 1.1.

The Earth's local magnetic field, which arises as a result of dynamo action of its molten core (Elsasser, 1956), extends far into space (roughly 10 earth radii in the direction of the sun and  $\sim 300$  earth radii in the anti-sunward direction) and interacts with the incoming solar wind. This interaction gives rise to a plethora of structures. Figure 1.2 shows an artistic rendition of Earth's magnetosphere. The layer along

<sup>4</sup> Figure 1.1 is based on data from Wind Spacecraft. See Section 4.1.1 for more details on data and spacecraft.

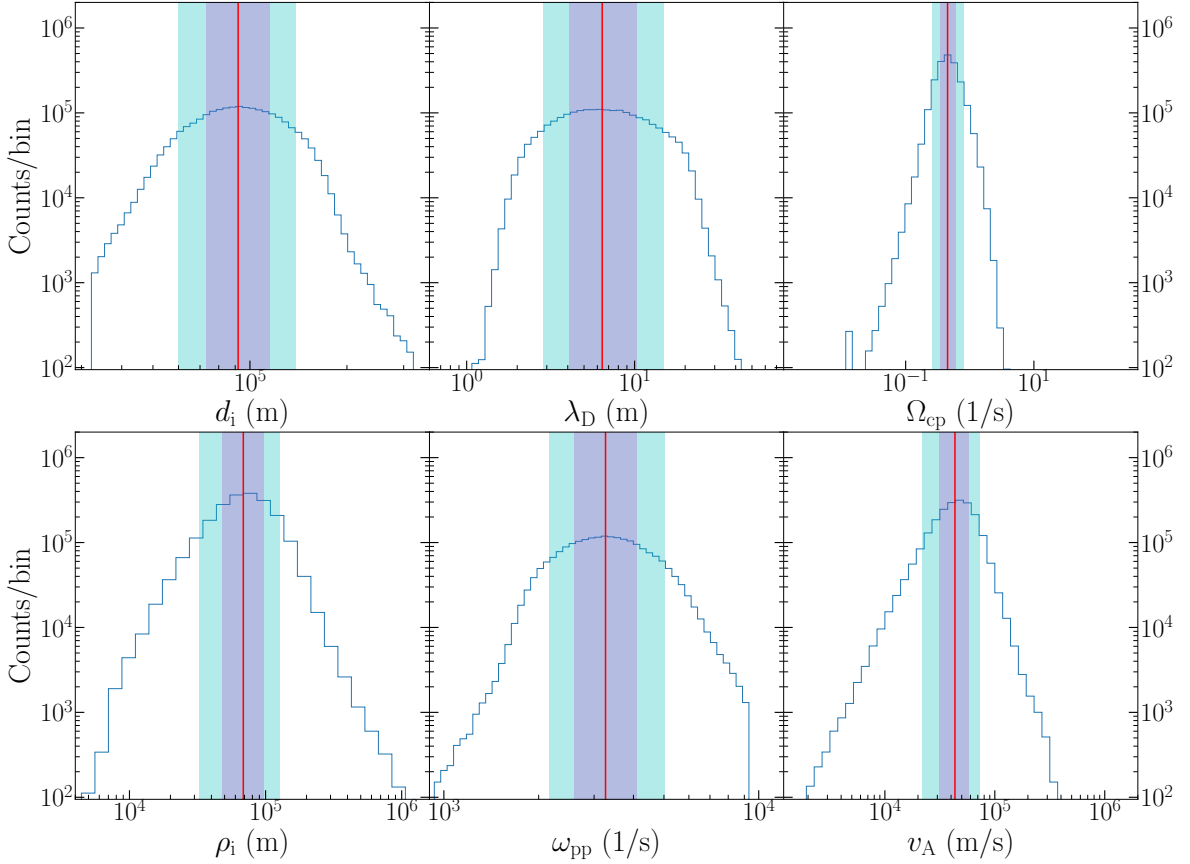


Figure 1.1: Distribution of various plasma parameters near Earth, based on data from Wind spacecraft. Top row shows distribution for (from left to right) proton-inertial length ( $d_i$ ), Debye length ( $\lambda_D$ ), proton-gyrofrequency ( $\Omega_{cp}$ ) and the lower row shows (from left to right) proton-gyroradius ( $\rho_i$ ), proton-plasma frequency ( $\omega_{pp}$ ) and alfvén speed ( $v_A$ ). Red line shows the median value of each parameter, whereas the shaded region shows 10<sup>th</sup> to 90<sup>th</sup> (cyan) and 25<sup>th</sup> to 75<sup>th</sup> percentile (magenta) of each parameter.<sup>4</sup>

which solar wind transitions from supersonic to subsonic speed is called the bow shock (region 1). The region immediately after the bow shock is called the magnetosheath (region 2) and is comprised mostly of shock treated solar wind. This region is of special importance to the present work (see Chapters 5 and 7). The region beyond the magnetosheath, towards Earth, where the pressure exerted by the solar wind and Earth's magnetic field are in equilibrium is called the magnetopause (region 3) and forms the boundary between Earth's magnetosphere (volume around Earth where the influence of its magnetic field is felt (region 4)) and the solar wind. There is also a long magnetotail further away from the Sun, which extends far beyond the surface of the Earth (regions 5 and 6). The region closest to the surface (region 7) is called the plasmasphere, which is made up of relatively cooler plasma and is located above the ionosphere. The shape and size of all these structures vary greatly depending on the velocity and density of the incoming plasma, the strength of magnetic field, and solar activity.

## 1.4 Studying Space Plasmas

In the previous section (Section 1.3) we discussed two different kinds of naturally occurring plasma regions close to Earth. A complete theory of plasma would require us to understand the commonality as well as the uniqueness of each of these regions. Consequently, over the last century or so the scientific community has devised several methods to study them. From Guglielmo Marconi using an antenna on a kite to receive radio signals in 1901 to NASA launching a spacecraft costing more than a billion dollars (Parker Solar Probe (PSP)) in 2018 to study the Sun from a closer distance than ever before, the community has been in a constant pursuit to understand them.

---

<sup>5</sup> These values are based on datasets as described in Chapter 4.

<sup>6</sup> Picture credit: [https://commons.wikimedia.org/wiki/File:Magnetosphere\\_Levels.svg](https://commons.wikimedia.org/wiki/File:Magnetosphere_Levels.svg)

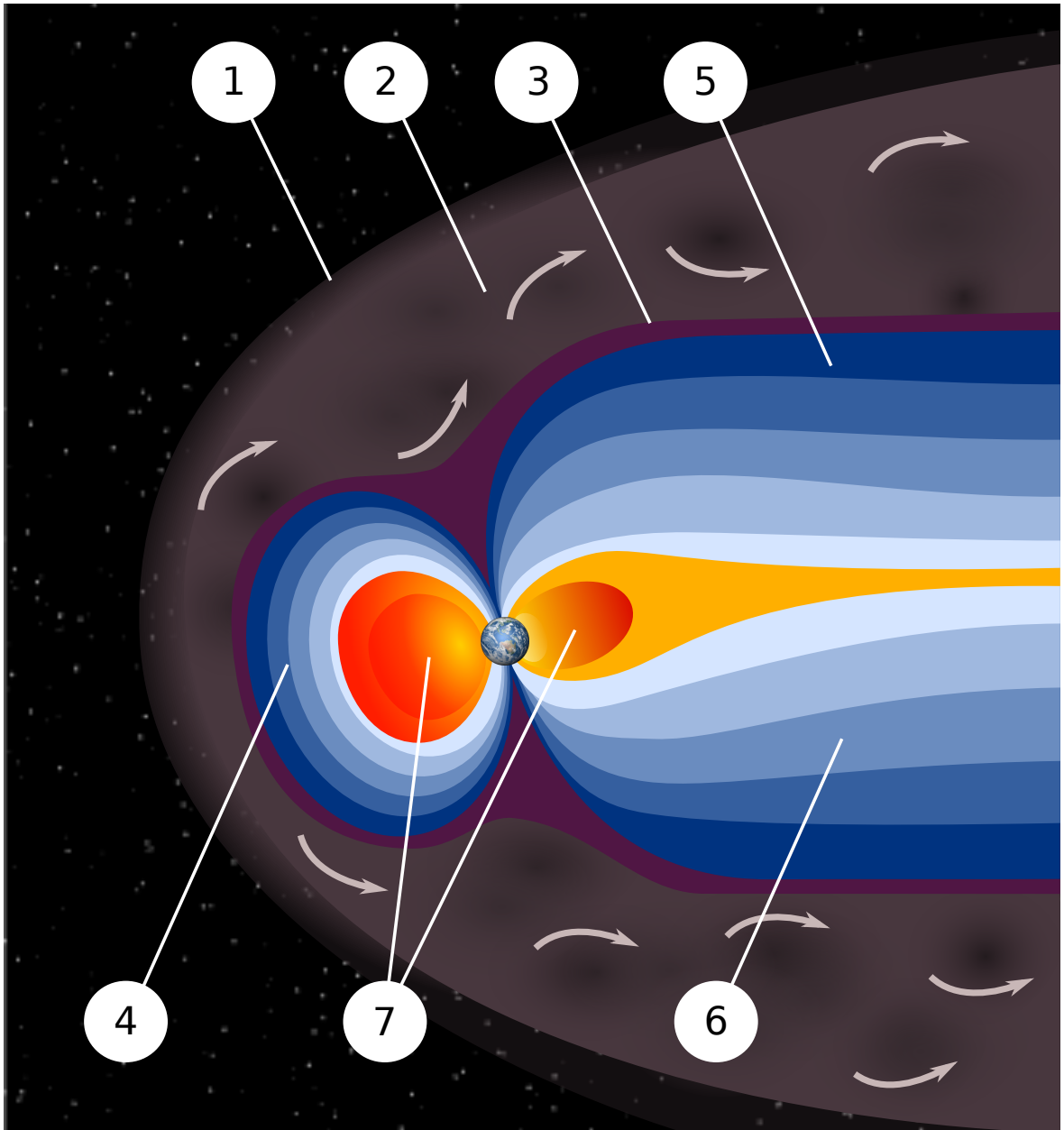


Figure 1.2: Artistic rendition of Earth's magnetosphere, its structure and different layers. The name of each numbered layer is 1.bow shock, 2. magnetosheath, 3. magnetopause, 4. magnetosphere, 5 and 6. tail lobes, 7. plasmasphere.<sup>6</sup>

Table 1.1: Plasma parameters and their typical values for different space plasmas.<sup>5</sup>

Parameter	Solar Wind (0.15 au )	Solar Wind (1 au )	Magnetosheath
$d_i$	$15,510 \pm 6,200$ m	$91,920 \pm 42,000$ m	$45,600 \pm 9,900$ m
$\lambda_D$	$2.87 \pm 1.98$ m	$6.41 \pm 6.20$ m	$23.18 \pm 8.00$ m
$\Omega_{cp}$	$6.47 \pm 2.70$ 1/s	$0.45 \pm 0.26$ 1/s	$2.16 \pm 1.00$ 1/s
$\omega_{pp}$	$19,328 \pm 7,300$ 1/s	$3,261 \pm 1,500$ 1/s	$6,574 \pm 1,500$ 1/s
$\rho_p$	$12,793 \pm 8,500$ m	$68,615 \pm 48,000$ m	$97,795 \pm 69,000$ m
$V_A$	$102,503 \pm 39,000$ m/s	$43,390 \pm 26,000$ m/s	$94,256 \pm 50,000$ m/s

## 1.5 In This Thesis

Work done towards this thesis presents an incremental contribution towards understanding the nature and behaviour of space plasmas. Chapters 2 and 3 provide a theoretical background on plasma microkinetics and turbulence, respectively. Chapter 4 gives a brief overview of all the datasets used in the present document and explains some of the data analysis techniques employed in Chapters 5 to 7.

Chapters 5 to 8 report the author's original work. Chapter 5 discusses the intermittency in space plasmas and simulations as well as its co-development with linear instabilities. Chapter 6 explores the heating of ions close to the Sun as a consequence of intermittent structures. Chapter 7 discusses the competition between linear and non-linear processes using a statistical approach on six different datasets. Chapter 8 presents an exploratory study of magnetic field reconstruction using machine learning

(ML) techniques. Chapter 9 provides a summary of the entire thesis and a guide for future work.

## Chapter 2

### KINETIC THEORY AND LINEAR MICROKINETIC INSTABILITIES

Kinetic theory forms a significant part of our understanding of plasma, specially at small scales (less than a  $d_i$ ). In this chapter, we give a brief overview of the salient properties of this theory. In Section 2.1 we start with the equation of motion for a charged particle in an electromagnetic field and extend this idea to an ensemble of particles. In Section 2.2 we discuss anisotropy and linear instabilities arising because of it. We also discuss how one can compute rate of growth of these instabilities using kinetic theory. In Section 2.3 we discuss some of the application and observational evidence of linear theory. We finish this chapter with a brief discussion of limitations of linear theory in Section 2.4.

#### 2.1 Introduction to Plasma Kinetic Theory

##### 2.1.1 Equations of motion

Consider a system which consists of a single charged particle of mass  $m$  and charge  $q$  in a magnetic field  $\mathbf{B}$  and an electric field  $\mathbf{E}$ . The non-relativistic equation of motion for this particle can then be written as:

$$m \frac{d\mathbf{v}_1}{dt} = q(\mathbf{E} + \mathbf{v}_1 \times \mathbf{B}) \quad (2.1)$$

and the its phase space exact density at any point in space can be written as :

$$\mathcal{F}_1(\mathbf{x}, \mathbf{v}, t) = \delta(\mathbf{x} - \mathbf{x}_1(t)) \delta(\mathbf{v} - \mathbf{v}_1(t)) \quad (2.2)$$

where  $\mathbf{x}_1(t)$  and  $\mathbf{v}_1(t)$  are the position and velocity of the particle at any time  $t$  and  $\delta(\dots)$  is the Dirac delta function. The six dimensional space spanned by  $\mathbf{x}$  and  $\mathbf{v}$  is

called phase space<sup>1</sup>. If we have  $n$  such particles in the system, then for the  $i^{\text{th}}$  particle, Equation (2.1) can be written as :

$$m_i \frac{d\mathbf{v}_i}{dt} = q_i (\mathbf{E}_\mu + \mathbf{v}_i \times \mathbf{B}_\mu) \quad (2.3)$$

where the subscript  $\mu$  represents the superposition of all the fields exerted by the particles in the system at the position of  $i^{\text{th}}$  particle. The total phase space density can now be written as:

$$\mathcal{F}_n(\mathbf{x}, \mathbf{v}, t) = \sum_{i=1}^n \delta(\mathbf{x} - \mathbf{x}_i(t)) \delta(\mathbf{v} - \mathbf{v}_i(t)) \quad (2.4)$$

In a closed system where there is no addition or removal of any particle, the total phase space density of a fluid element in phase space will remain constant in time. Using this conservation of phase space density one can write:

$$\frac{d}{dt} (\mathcal{F}_n(\mathbf{x}, \mathbf{v}, t)) = 0 \quad (2.5)$$

Since both  $\mathbf{x}$  and  $\mathbf{v}$  depend on time, we can use the chain rule and write Equation (2.5) as:

$$\frac{\partial \mathcal{F}_n}{\partial t} + \frac{d\mathbf{x}}{dt} \cdot \frac{d\mathcal{F}_n}{d\mathbf{x}} + \frac{d\mathbf{v}}{dt} \cdot \frac{d\mathcal{F}_n}{d\mathbf{v}} = 0 \quad (2.6)$$

where  $\frac{\partial}{\partial t}$  is the partial derivative with respect to  $t$ . In Equation (2.6) we have dropped  $(\mathbf{x}, \mathbf{v}, t)$  for the sake of readability. Using the fact that  $\frac{d}{dt}\mathbf{x} = \mathbf{v}$  and substituting for  $\frac{d\mathbf{v}}{dt}$  from Equation (2.3) in Equation (2.6), we have:

$$\frac{\partial \mathcal{F}}{\partial t} + \mathbf{v} \cdot \nabla_{\mathbf{x}} \mathcal{F} + \frac{q}{m} (\mathbf{E}_\mu + \mathbf{v} \times \mathbf{B}_\mu) \cdot \nabla_{\mathbf{v}} \mathcal{F} = 0 \quad (2.7)$$

Solving Equation (2.7) (called the Klimontovich-Dupree equation) is quite a difficult task since it contains all the microscopic fields, the computation of which involves tracking the position and velocity of all the particles, which as we have already discussed

<sup>1</sup> Note:  $\mathbf{x}$  and  $\mathbf{v}$  are independent coordinates in phase space.

is quite impossible to implement. This problem can be mitigated by writing the phase density as a sum of two parts, average and fluctuating as below:

$$\begin{aligned}\mathcal{F} &= \langle \mathcal{F} \rangle + \delta\mathcal{F} \\ &= f + \delta\mathcal{F}\end{aligned}\tag{2.8}$$

where  $\langle \mathcal{F} \rangle$  denotes the smoothed average or the background value of  $\mathcal{F}$ , and  $\delta\mathcal{F}$  is the fluctuation in the smoothed  $\mathcal{F}$ . For ease of writing, from now on  $\langle \mathcal{F} \rangle$  will simply be denoted by  $f$ , which is also called the distribution function and is interpreted as the probability of finding a particle at any location within a phase space volume  $d\mathbf{x}d\mathbf{v}$ . If we carry out the same process for the fields, we can write them as:

$$\begin{aligned}\mathbf{E}_\mu &= \langle \mathbf{E}_\mu \rangle + \delta\mathbf{E}_\mu \\ &= \mathbf{E} + \delta\mathbf{E}_\mu\end{aligned}\quad \begin{aligned}\mathbf{B}_\mu &= \langle \mathbf{B}_\mu \rangle + \delta\mathbf{B}_\mu \\ &= \mathbf{B} + \delta\mathbf{B}_\mu\end{aligned}\tag{2.9}$$

Since  $\mathcal{F}$ ,  $\mathbf{B}$  and  $\mathbf{E}$  are all smoothed averages, their fluctuations ( $\delta\mathcal{F}, \delta\mathbf{B}, \delta\mathbf{E}$ ) will form an statistical ensemble which would imply that  $\langle \delta\ldots \rangle = 0$ .

Using Equations (2.8) and (2.9) in Equation (2.7) and then taking the ensemble average, we have:

$$\frac{\partial f}{\partial t} + \mathbf{v} \cdot \nabla_{\mathbf{x}} f + \frac{q}{m} (\mathbf{E} + \mathbf{v} \times \mathbf{B}) \cdot \nabla_{\mathbf{v}} f = \frac{q}{m} \langle (\delta\mathbf{E} + \mathbf{v} \times \delta\mathbf{B}) \cdot \nabla_{\mathbf{v}} \mathcal{F} \rangle\tag{2.10}$$

This is the kinetic equation and defines the evolution of phase space density with time and position.

Computing the right hand side of Equation (2.10) is quite a difficult task, thus we often assume that the correlation between the background field and its fluctuation is infinitely small and collisions between particles account for correlation among themselves and occur uncorrelated of each other as random events, a consequence of the molecular chaos hypothesis (or *stoßzahlansatz*) (Clerk Maxwell, 1867). Under these assumptions we can simply replace the right side of Equation (2.10) with a collision operator,  $(\frac{\partial f}{\partial t})_c$ , which ideally will have all the information related to particle-particle interaction. Equation (2.10) can thus be re-written as:

$$\frac{\partial f}{\partial t} + \mathbf{v} \cdot \nabla_{\mathbf{x}} f + \frac{q}{m} (\mathbf{E} + \mathbf{v} \times \mathbf{B}) \cdot \nabla_{\mathbf{v}} f = \left( \frac{\partial f}{\partial t} \right)_c\tag{2.11}$$

This is the well known Boltzmann equation from statistical mechanics. [Baumjohann & Treumann \(1996\)](#) and references therein give some details about different functional forms of collisional operators.

Presence of collision can significantly alter the shape of a VDF (see Section [2.1.2](#) for definition). Since collisions can often result in transfer or exchange of energy and momentum between particles they work to erode the non-equilibrium features of a VDF (more on this later). In a fully ionized plasma where collisions are primarily coulombic in nature, computing the collision operator is further complicated by its dependence on temperature and density ([Baumjohann & Treumann, 1996](#)). [Landau \(1936\)](#) computed the collision operator,  $(\frac{\partial f}{\partial t})_c$ , for such a plasma, though solving it even for the simplest of cases is quite a daunting ask ([Verscharen et al., 2019](#)). However, [Marsch et al. \(1982a\)](#); [Marsch \(2010\)](#) showed that for space plasmas in the inner heliosphere collisions play negligible to minor role. We thus simply set the value of collision operator to zero and the Boltzmann equation (Equation [\(2.11\)](#)), in the absence of collision reduces to the Vlasov equation:

$$\frac{\partial f}{\partial t} + \mathbf{v} \cdot \nabla_{\mathbf{x}} f + \frac{q}{m} (\mathbf{E} + \mathbf{v} \times \mathbf{B}) \cdot \nabla_{\mathbf{v}} f = 0 \quad (2.12)$$

This equation forms the basis of much of kinetic theory for space plasmas and is used extensively in this thesis. We also use the Vlasov equation to derive the dispersion relation (see Section [2.2.1](#)), which gives us an idea about the kind of waves and instabilities present in the system (more on this later).

### **2.1.2 Distribution Function and Other Definitions**

As discussed in Section [2.1.1](#),  $f(\mathbf{x}, \mathbf{v}, t)$  gives the probability density function (PDF) of particles in phase space. Different statistical moments of the PDF gives us macroscopic properties of the whole ensemble. Often, we are interested in the behaviour of the system at one particular position in the configuration space at any given time. This would mean that the PDF will have no dependence on the position ( $\mathbf{x}$ ) or any explicit dependence on time ( $t$ ). We thus have a PDF with explicit dependence on just the velocity given as  $f(\mathbf{v})$ . This is referred to as velocity distribution function (VDF).

For a VDF we can define some parameters associated with plasma using its statistical moments.

**Density ( $n_j$ ):** Number density of species  $j$ , usually expressed in the units of  $\text{cm}^{-3}$  and can be derived from VDF by computing its zeroth order moment as follows:

$$n_j = \int_{\forall v} d^3v f_j(v) \quad (2.13)$$

**Bulk velocity ( $v_j$ ):** The bulk velocity of the species  $j$ , or the mean particle velocity, usually has units of  $\text{km/sec}$  and can be derived from the VDF's first-order moment:

$$\mathbf{v}_j = \frac{1}{n_j} \int_{\forall v} d^3v \mathbf{v} f_j(v) \quad (2.14)$$

**Thermal Speed ( $w_j$ ):** It represents the thermal speed of the species  $j$  and has units of  $\text{km/sec}$ . It is a measure of thermal energy of species  $j$  and the value for it can be derived from the VDF's second-order moment:

$$v_j^2 + 3 w_j^2 = \frac{1}{n_j} \int_{\forall v} d^3v \mathbf{v}^2 f_j(v) \quad (2.15)$$

For an anisotropic case, where temperature is different along different directions, Equation (2.15) is computed for each component separately (see [Verscharen et al. \(2019, §1.4.1\)](#) for a detailed description).

**Temperature ( $T_j$ ):** Using the thermal speed, one can define the temperature (in units of K) of the species as:

$$T_j = \frac{m_j w_j^2}{2k_B} \quad (2.16)$$

In a magnetized plasma, the VDFs commonly exhibit distinct temperatures perpendicular and parallel to the magnetic field because of the slightly different heating or cooling rates in different directions ([Stix, 1992](#); [Gary, 1993](#)). We thus have different temperatures in parallel ( $T_{||j}$ ) and perpendicular ( $T_{\perp j}$ ) directions and the total temperature of species  $j$  is then given as:

$$T_j = \frac{T_{||j} + 2T_{\perp j}}{3} \quad (2.17)$$

The ratio of two temperatures (perpendicular and parallel) is called anisotropy and is expressed as:

$$R_j = \frac{T_{\perp j}}{T_{\parallel j}} \quad (2.18)$$

**Parallel Beta ( $\beta_{\parallel j}$ ):** It is the ratio of parallel thermal energy of a species to the magnetic pressure energy stored in the field.

$$\beta_{\parallel j} = \frac{n_j k_B T_{\parallel j}}{B_0^2 / (2\mu_0)} \quad (2.19)$$

As we will see later in this chapter (see Section 2.2.2) the values of parameters  $R_j$  and  $\beta_{\parallel j}$  play an important role in determining if a region of plasma is stable or unstable.

### Shape of a VDF:

In general the VDF can take a variety of forms as long as they conform to the laws of probability. For a plasma in local thermodynamic equilibrium, it takes the shape of a Maxwellian distribution as shown in Equation (2.20).

$$f_j(\mathbf{v}) = \frac{n_j}{(\pi w_j^2)^{3/2}} \exp\left(-\frac{|\mathbf{v} - \mathbf{v}_0|^2}{w_j^2}\right) \quad (2.20)$$

where  $\mathbf{v}_0$  is the streaming velocity of the plasma. Each species ( $j$ ) in the plasma has its own VDF, the statistical moments of which give the species' bulk parameters (e.g., density and velocity).

One can define a direction based on the background field present in the plasma. If we assign the direction along the magnetic field as the parallel direction (represented by  $\parallel$ ) and the other two orthogonal directions as the perpendicular direction (represented by  $\perp$ ), the total magnetic field can be expressed in this new coordinate system as:

$$\mathbf{B} = B_{\parallel} \hat{\mathbf{e}}_{\parallel} + B_{\perp} \hat{\mathbf{e}}_{\perp} \quad (2.21)$$

where  $\hat{\mathbf{e}}_{\parallel}$  and  $\hat{\mathbf{e}}_{\perp}$  are the unit vectors along and perpendicular to the magnetic field.

It is often easier to work with VDFs in this coordinate system, thus we rewrite Equation (2.20) for a species  $j$  in the new coordinate system as:

$$f_j(\mathbf{v}) = \frac{n}{\pi^{3/2} w_{\perp j}^2 w_{\parallel j}} \exp \left( -\frac{(v_{\parallel} - v_{\parallel 0j})^2}{w_{\parallel j}^2} - \frac{|\mathbf{v}_{\perp} - \mathbf{v}_{\perp 0j}|^2}{w_{\perp j}^2} \right) \quad (2.22)$$

The values of  $v_{\parallel 0j}$  and  $\mathbf{v}_{\perp 0j}$  are often different resulting in a slightly different VDF in the two directions. For such a case, the VDF is referred to as the bi-Maxwellian distribution.

Though in this thesis we use Equation (2.22) as the standard/default VDF unless otherwise stated, it must be noted that for solar wind, especially at 1 au, the VDF departs significantly from a simple bi-Maxwellian (Feldman et al., 1974; Feldman et al., 1974; Marsch et al., 1982b; Alterman et al., 2018). Ion VDFs often have an asymmetry which can be more accurately accounted for by superposition of a differentially flowing bi-Maxwellian (Alterman et al., 2018). Other forms of distribution such as kappa distribution has also been used to study the non-Maxwellian features of VDF like enhanced tail (Pierrard & Lazar, 2010; Pierrard & Pieters, 2014; Maksimovic et al., 1997; Nicolaou et al., 2020).

## 2.2 Linear Microkinetic Instabilities

### 2.2.1 The Linear Dispersion Relation

Though in Section 2.1.1 we made several assumptions and used our a priori knowledge of the system, solving Equation (2.12) for even a simple distribution like the bi-Maxwellian (Equation (2.22)) is quite complicated and computationally expensive. Coupling between fields produced by one species with another species complicates it further. Linearization (or linear analysis), where one assumes plain wave perturbation in fields and the VDF helps simplify the problem while keeping the underlying physics of the equations intact as long as the fluctuations have small amplitude relative to the background values. In standard linear theory, we assume an equilibrium (i.e., constant) background and perturb it with a small-amplitude sinusoidal fluctuation of wave vector  $\mathbf{k}$  and angular frequency  $\omega$ . The goal then is to derive, for a given plasma,

the dispersion relation: the relationship between  $\mathbf{k}$  and  $\omega$ . Under this assumption one can rewrite Equations (2.8) and (2.9) as:

$$\begin{aligned} f_j(\mathbf{x}, \mathbf{v}, t) &= f_j^0(\mathbf{x}, \mathbf{v}) + f_j^1(\mathbf{x}, \mathbf{v}, t) \\ &= f_j^0(\mathbf{x}, \mathbf{v}) + f_j^1(\mathbf{k}, \omega, \mathbf{v}) e^{(i(\mathbf{k} \cdot \mathbf{x} - \omega t))} \end{aligned} \quad (2.23)$$

$$\begin{aligned} \mathbf{B}(\mathbf{x}, t) &= \mathbf{B}^0(\mathbf{x}) + \mathbf{B}^1(\mathbf{x}, t) \\ &= \mathbf{B}^0(\mathbf{x}) + \mathbf{B}^1(\mathbf{k}, \omega) e^{(i(\mathbf{k} \cdot \mathbf{x} - \omega t))} \end{aligned} \quad (2.24)$$

$$\begin{aligned} \mathbf{E}(\mathbf{x}, t) &= \mathbf{E}^0(\mathbf{x}) + \mathbf{E}^1(\mathbf{x}, t) \\ &= \mathbf{E}^0(\mathbf{x}) + \mathbf{E}^1(\mathbf{k}, \omega) e^{(i(\mathbf{k} \cdot \mathbf{x} - \omega t))} \end{aligned} \quad (2.25)$$

Where  $\mathbf{k}$  and  $\omega$  are the wavenumber vector and the frequency of perturbation, respectively. Equations (2.23) to (2.25) along with Maxwell's equation's (Equations (1.3) to (1.6)) help us drive the dispersion relations. In order to do so, we start with some simple assumptions and conditions. We work in a frame of reference where the zeroth order current density ( $\mathbf{J}^0(\mathbf{x})$ ) and electric field ( $\mathbf{E}^0(\mathbf{x})$ ) are zero and the magnetic field ( $\mathbf{B}^0(\mathbf{x})$ ) is constant. Thus Equations (2.24) and (2.25) can be rewritten as:

$$\mathbf{B}(\mathbf{x}, t) = \mathbf{B}_0 + \mathbf{B}^1(\mathbf{x}, t) \quad (2.26)$$

$$\mathbf{E}(\mathbf{x}, t) = \mathbf{E}^1(\mathbf{x}, t) \quad (2.27)$$

$$\mathbf{J}(\mathbf{x}, t) = \mathbf{J}^1(\mathbf{x}, t) \quad (2.28)$$

We choose a coördinate system with  $z$ -axis along the background magnetic field ( $\mathbf{B}_0$ ). The angle between the direction of propagation of fluctuation ( $\mathbf{k}$ ) and the magnetic field is:

$$\cos(\theta) = \frac{\mathbf{k} \cdot \mathbf{B}}{kB} \quad (2.29)$$

Substituting expressions for  $\mathbf{J}$ ,  $\mathbf{B}$  and  $\mathbf{E}$  into Maxwell's equations (Equations (1.3) to (1.6)) and simplifying we have:

$$\mu_0 \mathbf{J}^1(\mathbf{k}, \omega) = \frac{i}{\omega} \mathbf{k} \times [\mathbf{k} \times \mathbf{E}^1(\mathbf{k}, \omega)] + \frac{i\omega}{c^2} \mathbf{E}^1(\mathbf{k}, \omega) \quad (2.30)$$

In similar fashion to the particle velocity in Equation (2.14) one can write the flux density as:

$$\Gamma_j^1(\mathbf{k}, \omega) = \int_{-\infty}^{\infty} d^3v \mathbf{v} f_j^1(\mathbf{k}, \omega, \mathbf{v}) \quad (2.31)$$

and thus define the current density as:

$$\mathbf{J}^1(\mathbf{k}, \omega) = \sum_j q_j \Gamma_j^1(\mathbf{k}, \omega) \quad (2.32)$$

For species  $j$  we can define the dimensionless conductivity tensor  $\mathbf{S}_j$  as:

$$\Gamma_j^1(\mathbf{k}, \omega) = -\frac{i \epsilon_0 k^2 c^2}{q_j \omega} \mathbf{S}_j(\mathbf{k}, \omega) \cdot \mathbf{E}^1(\mathbf{k}, \omega) \quad (2.33)$$

Combining Equations (2.28), (2.30) and (2.32) gives us:

$$\mathbf{D}(\mathbf{k}, \omega) \cdot \mathbf{E}^1(\mathbf{k}, \omega) = 0 \quad (2.34)$$

where,

$$\mathbf{D}(\mathbf{k}, \omega) = (\omega^2 - c^2 k^2) \mathbf{I} + c^2 \mathbf{k} \mathbf{k} + c^2 k^2 \sum_j \mathbf{S}_j(\mathbf{k}, \omega) \quad (2.35)$$

with  $\mathbf{I}$  being the 3-dimensional identity matrix and  $\mathbf{k} \mathbf{k}$  being the dyadic<sup>2</sup> product of the wavevector. For Equation (2.35) to be true,  $\mathbf{E}^1$  cannot be allowed to go to zero since that would allow perturbations in the system to vanish. Hence we must have the determinant of  $\mathbf{D}(\mathbf{k}, \omega)$  go to zero, thus:

$$\det(\mathbf{D}(\mathbf{k}, \omega)) = 0 \quad (2.36)$$

which is the plasma dispersion relation. Gary (1993) notes that this equation can be solved “either as a boundary value problem ( $\omega$  is given as real, one solves for a complex component of  $\mathbf{k}$ ) or as an initial value problem ( $\mathbf{k}$  is given as real, one solves for complex  $\omega$ )”.

---

<sup>2</sup> The dyadic product between two vectors  $\mathbf{a}$  and  $\mathbf{b}$  is simply the product between the vector and its transpose, so one has  $\mathbf{a} \mathbf{b} = \mathbf{a} \mathbf{b}^T$ , which results in a rank-two tensor.

Equation (2.36) in general gives infinite number of solutions for  $\omega$  for any value of  $\mathbf{k}$  and a set of plasma parameters. Thus  $\omega(\mathbf{k})$  is a multi valued function with multiple branches corresponding to different modes (see [Schwartz \(1980, Figure 2\)](#)). However most modes are strongly damped and thus dissipate before they can substantially effect the plasma.

### 2.2.2 Temperature Anisotropy Induced Instabilities

In a homogeneous plasma (PDF is independent of position) in local thermodynamic equilibrium (LTE), all fluctuations (at any  $\mathbf{k}$  and  $\omega$ ) are damped and thus have a decaying amplitude. However, departure from LTE because of the non-Maxwellian properties of VDFs (temperature anisotropy or relative drift between two different species, etc.) introduce free energy into the system. This results in circumstances where instead of getting damped some perturbations grow exponentially and make the system unstable. The rate at which such a perturbation propagates and gets damped or grows is computed by solving the dispersion relation (Equation (2.36)). Solutions of Equation (2.36) using the initial value problem method gives  $\omega$ , which is in general complex and can be written as:

$$\omega = \omega_r + i\gamma \quad (2.37)$$

where,  $\omega_r$  is the real component and  $\gamma$  is the damping rate ( $\gamma < 0$ ) or growth rate ( $\gamma > 0$ ). In the presence of a growth rate, the fluctuations present in the system start to grow exponentially. If the process continues, fluctuations start having amplitudes comparable to the background value, which makes the assumption of linearity void and makes the system non-linear. The state of the system can no longer be predicted by linear theory and instead relies on non-linear dynamics.

When an instability has  $\gamma = 0$  for any wave vector, we call it threshold of the associated instability. We also define  $\gamma_{\max}$  for a given branch of dispersion solutions as the maximum value of  $\gamma$  for different wavenumbers ( $\mathbf{k}$ ) and for all propagation

directions ( $\theta$ ).  $\omega_{max}$  and  $\mathbf{k}_{max}$  are then defined as the values of  $\omega$  and  $\mathbf{k}$  corresponding to  $\gamma = \gamma_{max}$  respectively. Mathematically this can be written as:

$$\gamma_{max}^j = \max(\gamma^j(\mathbf{k}, \theta)) \quad \forall (\mathbf{k}, \theta) \quad (2.38)$$

where  $j$  represents the branch of dispersion solutions for which  $\gamma$  was computed.

In this thesis we consider ion temperature anisotropy as the only source of free energy. For instability driven by ion temperature anisotropy, there are four distinct modes depending on the anisotropy value ( $R_p$ ) and the direction of propagation ( $\theta$ ). For parallel propagation ( $\theta = 0$ ), there are two modes: ion cyclotron for  $R_p > 1$  and parallel firehose for  $R_p < 1$ . In the oblique direction ( $0 < \theta < 90$ ), the corresponding instabilities are mirror ( $R_p > 1$ ) and oblique firehose ( $R_p < 1$ ). It is worth noting that neither of these two oblique instabilities propagate. Table 2.1 gives a summary of all four instabilities discussed.

Table 2.1: List of four temperature-anisotropy induced instabilities in plasma

Anisotropy Range	Parallel ( $\omega_r > 0$ )	Oblique ( $\omega_r = 0$ )
$R_p > 1$	Ion cyclotron	Mirror
$R_p < 1$	Parallel firehose	Oblique firehose

### 2.2.3 Computing Growth Rates

Computation of growth rates ( $\gamma$ ) for any given value of the plasma parameters for a given branch of instability means solving Equation (2.36) for all different values of  $\mathbf{k}$ . This is generally done by using a numerical dispersion solver. This project used tables of  $\gamma_{max}$  as a function of the plasma parameters developed by [Maruca et al. \(2012\)](#) using the software of [Gary \(1993\)](#). For our case, given a value of  $R_p$  and  $\beta_{\parallel p}$ , we check the table for values of  $(R_p, \beta_{\parallel p})$  that are closest to the input value and then use an interpolation technique (cubic spline interpolation) to get the value at that exact input point.

Once we get the  $\gamma_{max}$  value corresponding to an instability, we normalize it to the cyclotron frequency of protons ( $\gamma_{max} \rightarrow \gamma_{max}/\Omega_{cp}$ ). However, not all computed

values of the growth rate will have a significant effect on the plasma dynamics. As is expected if growth rate is high, the instability grows faster and conversely it will take the instability a long time to manifest or change the dynamics if it has a small growth rate. Thus, one can think of  $1/\gamma$  as a proxy for the amount of time it will take for the instability to manifest itself. For a positive but an infinitesimal value of  $\gamma_{\max}$ , the value of time will be much, much greater than the other characteristic time scales of the system, which means the instability will never have time to significantly affect the plasma. We thus define a cut-off value of growth rates, in units of proton cyclotron frequency, as:

$$\gamma_{\max,\text{cut-off}}^j = 10^{-5} \Omega_{\text{cp}} \quad (2.39)$$

For any combination of  $(R_p, \beta_{\parallel p})$  if the value of  $\gamma_{\max}/\Omega_{\text{cp}}$  is less than  $10^{-5}$  we essentially set those values to zero and assume that the plasma is completely stable at those points. Choosing this cut-off is a bit arbitrary. Different studies have chosen different threshold values. For example [Gary & Cairns \(1999\)](#) and [Gary & Karimabadi \(2006\)](#) chose  $\gamma = 10^{-2} \Omega_{\text{cp}}$  as their cut-off, whereas both [Hellinger et al. \(2006\)](#) and [Klein et al. \(2018\)](#) settled on cut-off value of  $\gamma = 10^{-3} \Omega_{\text{cp}}$ . As long as the cut-off value of  $\gamma$  is significantly smaller than that of other relevant time scales (see Sections 3.3 and 7.3) it can comfortably be set to zero.

### 2.3 Application of linear theory and observational evidence

The low density and extreme dynamics of space plasmas, such as solar wind and the magnetosheath (see Section 1.3), ensure that they almost invariably deviate substantially from local thermal equilibrium ([Marsch, 2006](#); [Verscharen et al., 2019](#)). For example, even though the majority of solar wind ions are protons (ionized hydrogen) or  $\alpha$ -particles (fully ionized helium), these two particle species rarely have equal temperatures or bulk velocities (see, e.g., [Feldman et al., 1974](#); [Marsch et al., 1982a](#); [Hefti et al., 1998](#); [Kasper et al., 2008](#); [Maruca et al., 2013](#)). Figure 2.1 shows the distribution of temperature for these two species using data from the Wind spacecraft

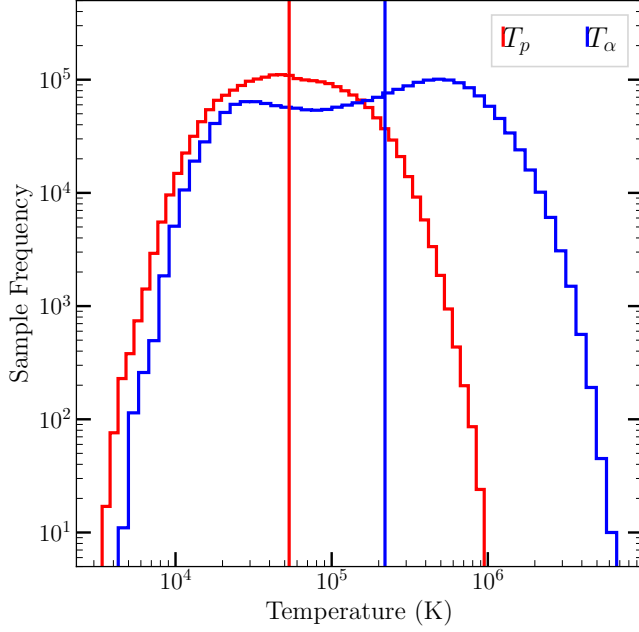


Figure 2.1: Distribution of proton and  $\alpha$ -temperatures at 1 au. Vertical lines show the median temperature of each species.

(Section 4.1.1 for more details on the dataset used). Furthermore, the VDF of any given ion species often significantly departs from the entropically favored Maxwellian functional form (Feldman et al., 1973a; Feldman et al., 1974; Marsch et al., 1982b; Alterman et al., 2018). Observations of solar wind and magnetosheath from multiple spacecraft (Feldman et al., 1973b; Marsch et al., 1982b; Kasper et al., 2002) have shown that the protons exhibit distinct kinetic temperatures,  $T_{\perp p}$  and  $T_{\parallel p}$ . Both values of  $R_p > 1$  and  $R_p < 1$  are commonly observed in the solar wind and in Earth’s magnetosheath, making it an ideal candidate for the application of linear Vlasov theory. Figure 2.2 shows distribution of  $R_p$  for solar wind at 1 au and magnetosheath.

As discussed in Section 2.2.2 if  $R_p$  departs sufficiently from unity, it can trigger a kinetic microinstability: a short-wavelength fluctuation with an exponentially growing amplitude. The threshold  $R_p$ -value for the onset of a proton temperature-anisotropy instability depends on all plasma parameters (e.g., composition and relative temperatures), depending most strongly on proton parallel beta ( $\beta_{\parallel p}$ ). Figure 2.3 shows various thresholds on an  $(R_p, \beta_{\parallel p})$  plane for the four modes of instabilities. As is evident, at

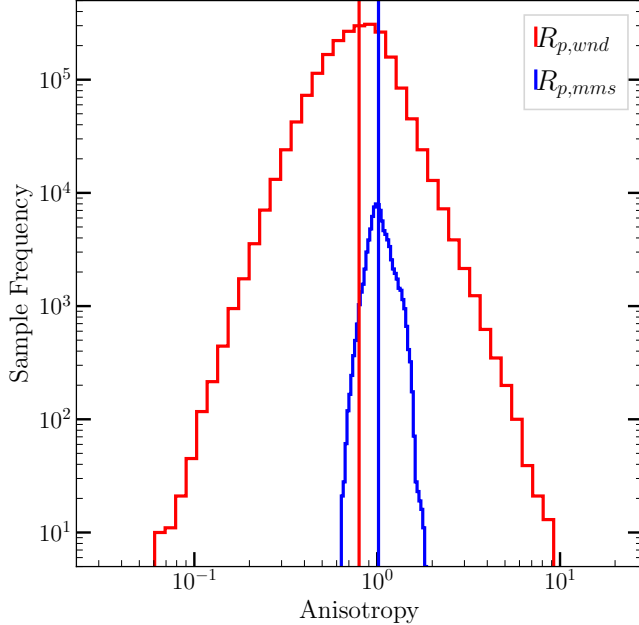


Figure 2.2: Distribution of proton temperature anisotropy at 1 au (red) and in the magnetosheath (blue). Vertical lines show the median values at each location.

fixed  $R_p$  a slight increment in  $\beta_{\parallel p}$  can lead to significant increase in the growth rate.

These instabilities have threshold  $R_p$ -values, which means that they can effectively limit the degree to which proton temperature can depart from isotropy. If an unstable mode grows and does not saturate, it eventually becomes nonlinear, continues to scatter particles in phase space, and eventually drives the VDF toward local thermal equilibrium. Multiple studies have analyzed large datasets from various spacecraft and under the assumptions of a spatially homogeneous plasma and a bi-Maxwellian proton velocity distribution; such studies have found that the joint distribution of  $(\beta_{\parallel p}, R_p)$ -values from the interplanetary solar wind largely conform to the limits set by the instability thresholds (Gary et al., 2001; Kasper et al., 2002; Hellinger et al., 2006; Matteini et al., 2007). Figure 2.4 shows the joint probability distribution of  $(R_p, \beta_{\parallel p})$  and the thresholds corresponding to different instability modes for  $\gamma_{\max}/\Omega_{cp} = 10^{-2}$ <sup>3</sup>. We can see that the probability density decreases significantly as one moves closer to

---

<sup>3</sup> Please see Appendix A for more details on how these figures were made and how thresholds were computed

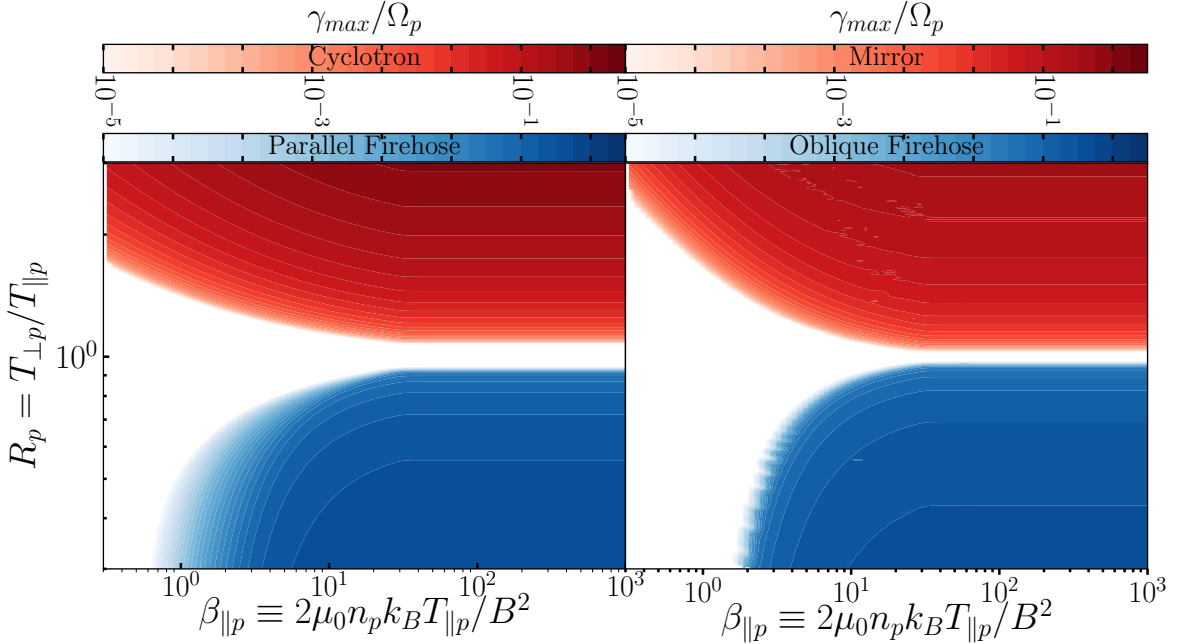


Figure 2.3: Contours of constant growth rates.

any of the threshold values. A recent study by [Maruca et al. \(2018\)](#) confirmed the same effect in Earth’s magnetosheath, which is shown in Figure 2.5 (see Appendix A for examples of a  $(\beta_{\parallel p}, R_p)$ -plot in other systems). Additional studies have found that plasma with unstable  $(\beta_{\parallel p}, R_p)$ -values is statistically more likely to exhibit enhancements in magnetic fluctuations ([Bale et al., 2009](#)) and proton temperature ([Maruca et al., 2011](#)). These findings suggest that the instabilities not only regulate temperature anisotropy in space plasmas but, in doing so, play an integral role in the large-scale evolution of the plasmas.

The empirical studies of  $(\beta_{\parallel p}, R_p)$ -distributions — especially that by [Matteini et al. \(2007\)](#) — indicate that the instabilities globally limit proton temperature anisotropy and affect the large-scale thermodynamics of expanding solar wind plasma. Nevertheless, the instabilities themselves act on far smaller scales. Indeed, [Osman et al. \(2012a\)](#) found that unstable  $(\beta_{\parallel p}, R_p)$ -values are statistically more likely to exhibit enhanced values of the partial variance of increments (PVI), which is an indicator of intermittent structure (see Section 3.2.3). This result suggests that long-wavelength turbulence

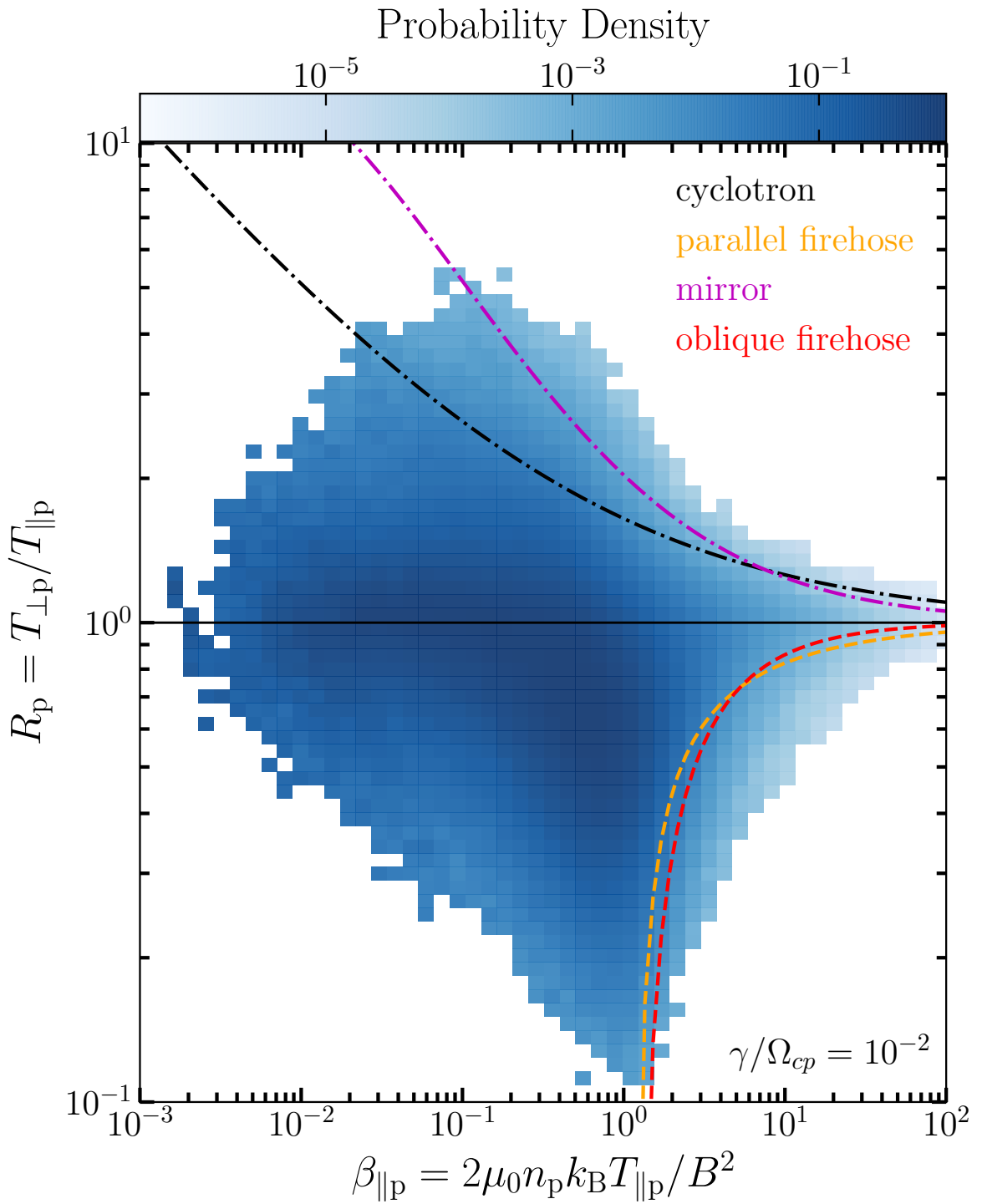


Figure 2.4: Plot of estimated probability density,  $\tilde{p}$  of  $(R_p, \beta_{\parallel p})$  for solar wind at 1 au (from `wnd` dataset, see Chapter 4) and thresholds associated with different instabilities for threshold value of  $\gamma_{\max}/\Omega_{cp} = 10^{-2}$ .

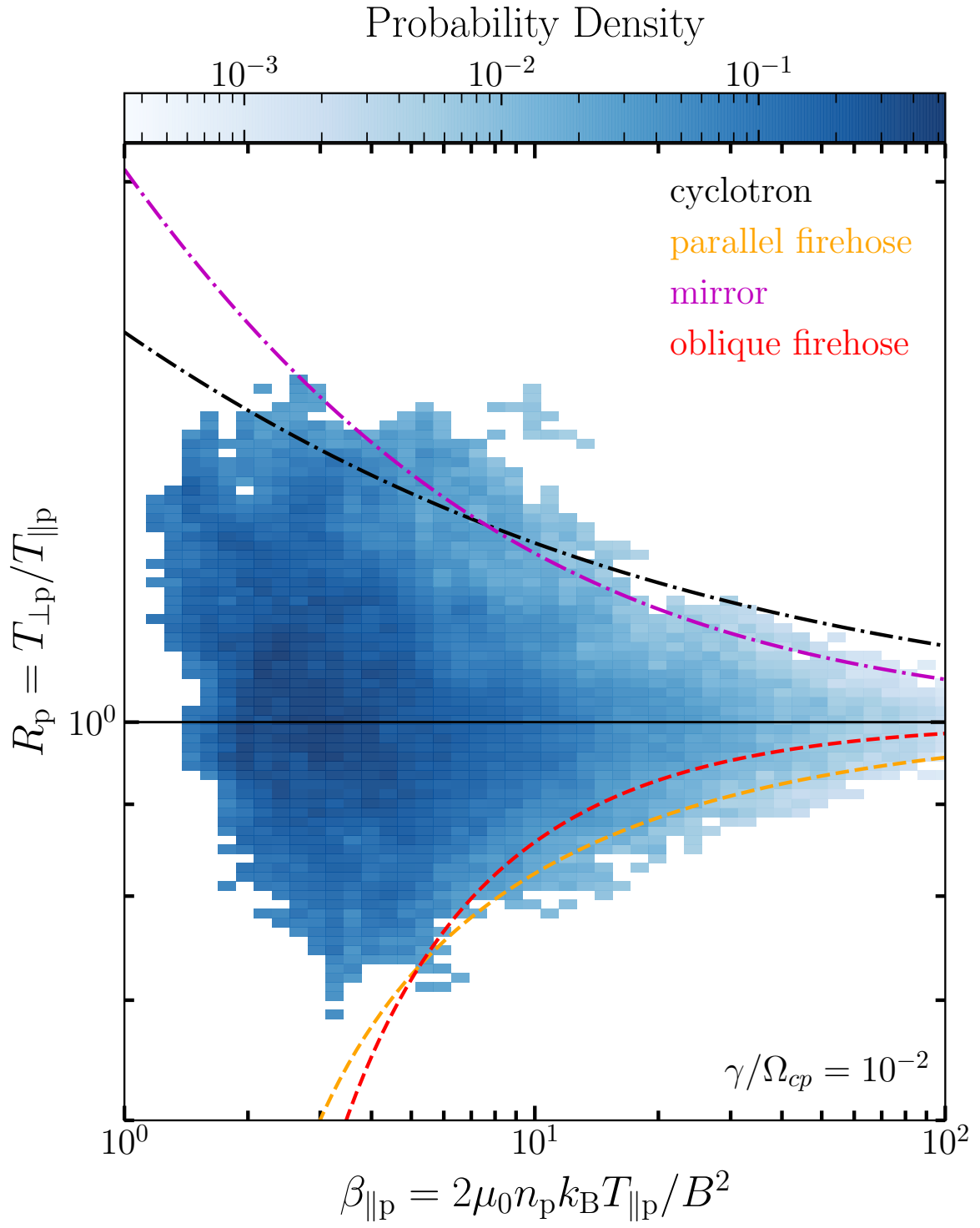


Figure 2.5: Plot of estimated probability density,  $\tilde{p}$  of  $(R_p, \beta_{\parallel p})$  for Earth's magnetosheath (from mms dataset, see Chapter 4) and thresholds associated with different instabilities for threshold value of  $\gamma_{\max}/\Omega_{cp} = 10^{-2}$ .

may play a substantial role in generating the local plasma conditions that drive these microinstabilities. Also, advancements made in numerical simulation by Servidio et al. (2012); Greco et al. (2012); Servidio et al. (2015), with corroboration from space plasma observations (Marsch et al., 1992; Sorriso-Valvo et al., 1999; Osman et al., 2011, 2012a; Kiyani et al., 2009) show the importance of intermittency in interpretation of these observations. We discuss these in more detail in Chapter 3.

## 2.4 Limitations of linear theory

Though linear theory works well for plasma with a homogeneous background, when it comes to its application to study the characteristics of space plasmas, the method is not without caveats. Multiple studies have shown space plasma to be highly structured and thus inhomogeneous (Burlaga, 1968; Tsurutani & Smith, 1979; Ness & Burlaga, 2001; Osman et al., 2012a,b; Greco et al., 2012). In fact, by all accounts, inhomogeneity is ubiquitously present in space plasma, and thus any study of instabilities in plasma should take into account the inhomogeneity of the background among variation in other parameters.

Consequently, use of linear theory for such studies of course presents a theoretical inconsistency in the application of computed instability thresholds to study the properties of plasma because of the underlying disparity between the assumptions of linear theory and the observed space plasma. However, several studies over the last three decades have presented empirical evidence of agreement between the observations and theoretical predictions (Gary, 1991; Gary et al., 1994, 2001; Gary & Karimabadi, 2006; Kasper et al., 2002; Hellinger et al., 2006; Maruca et al., 2011, 2012; Maruca et al., 2018). These studies strongly suggest that linear instability thresholds are indeed efficient in restricting the plasma/plasma VDF in a narrow region of  $(\beta_{\parallel p}, R_p)$ -plane, inhibiting the excursion of plasma VDFs to extreme anisotropy regions at high  $\beta_{\parallel p}$ . Although limitations on spatial and temporal resolution using present-day spacecraft make it difficult to directly demonstrate the existence of such instabilities in space plasmas, work done by, Bale et al. (2009); He et al. (2011); Podesta (2013); Jian et al.

(2009, 2010); Jian et al. (2014); Klein et al. (2014); Telloni & Bruno (2016); Gary et al. (2016) among others provide indirect evidence for the presence of various different instabilities. More details can be found in Verscharen et al. (2019) and references therein.

Given these limitations of linear theory and its application, we have to look into the non-linear processes and study how those processes affect the dynamics of the plasma. Chapter 3 introduces some the non-linear processes in plasmas and discusses how they affect the dynamics.



## Chapter 3

### NON-LINEAR PLASMA DYNAMICS

#### 3.1 Introduction to Turbulence

In laminar flow, different layers of fluid move smoothly without much mixing between layers, and the characteristic quantities/parameters - like velocity, pressure, or density - vary smoothly in a predictable way. A system where these quantities fluctuate in a chaotic fashion is called turbulent and the phenomena is called turbulence. Because of the chaotic nature of the fluctuations, unlike the laminar flow, prediction of the exact state of the system is essentially impossible. This makes a system extremely complicated to study, so much so that Sir Horace Lamb once remarked ([Goldstein, 1969](#)):

I'm an old man now, and when I die and go to heaven there are two matters on which I hope for enlightenment. One is quantum electrodynamics, and the other is turbulent motion of fluids. And about the former I'm rather optimistic.

Turbulence is extremely complicated and the fact that it is ubiquitous in nature (and in most man made processes involving fluids) makes it unavoidable.

Whether a given fluid system will develop turbulence largely depends on its viscosity, which is the liquid equivalent of friction and is a measure of how easy it is for the liquid to flow ([Chapman, 1916; Jeans, 1905](#)) and its Reynolds number ([Reynolds, 1883, 1886; Matthaeus & Montgomery, 1980](#)). A small Reynolds number means that the system is laminar whereas a high value Reynolds number implies turbulent flow. For a neutral fluid it is defined as:

$$R_e = L \frac{u}{\nu} \quad (3.1)$$

where  $L$  is the characteristic length of the system,  $u$  is the mean flow velocity and  $\nu$  is the kinematic viscosity. For a similar amount of force or external pressure, a highly viscous fluid or one with low  $R_e$  can maintain laminar flow for much longer duration than a fluid with low viscosity or high  $R_e$ . Presence of viscosity in a fluid leads to interaction between different layers or scales and results in energy transfer from larger to smaller scales through eddies which eventually reaches the smallest scale and dissipate as heat ([Kolmogorov, 1941a,b](#)) in a process called energy cascade in turbulence. In a weakly collisional and magnetized plasma, the presence of charged particle and magnetic field complicates the process. For a system like solar wind, the situation is further complicated because of the relatively similar size of the system and the mean free path<sup>1</sup> ([Echim et al., 2010](#), Appendix 2) both of which are of the order of 1 au ([Verscharen et al., 2019](#), Table 1) and thus one cannot use the classic methodology developed by [Enskog \(1917\)](#) and [Chapman \(1918\)](#).

Turbulence cascade has far reaching consequences for both neutral fluids and plasmas. It provides a pathway for the dissipation or transfer of energy from large scales, where they can be introduced, to smaller scales. In the next section (Section 3.2) we will look at some of the consequences of turbulence in space plasmas. We discuss only those which are relevant to this thesis. In Section 3.3 we discuss the linear and non-linear time scales associated with their respective phenomena.

### 3.2 Consequences of Turbulence in Space Plasmas

In-situ observations and theoretical interpretations have established the ubiquitous presence of turbulence in space plasmas ([Matthaeus & Velli, 2011](#); [Matthaeus, 2021](#), and references therein). In this section we discuss three of the major consequences that arise because of turbulence in space plasmas. Though these three are not the only consequences of turbulence, these were selected because of their relevance to this thesis, as we will see in Chapters 5 to 7.

---

<sup>1</sup> Mean free path is defined as the average distance travelled by particles between two successive collisions.

### 3.2.1 Heating of plasma

In space plasmas, under the assumption that the magnetic field changes slowly (slower than the ion gyrotropic time scale), the magnetic moment ( $\mu$ ) of the particle is conserved (Baumjohann & Treumann, 1996; Verscharen et al., 2019). Thus, we can write:

$$\frac{d\mu}{dt} = 0 \quad (3.2)$$

where,  $\mu = m_p w_{\perp p}^2 / (2B)$ ,  $m_p$  is the proton mass,  $w_{\perp p}^2$  is the perpendicular thermal velocity and  $B$  is the magnitude of magnetic field. Writing Equation (3.2) in terms of the proton-perpendicular temperature using Equation (2.16), we have:

$$\frac{d}{dt} \left( \frac{k_B T_{\perp p}}{B} \right) = 0 \quad (3.3)$$

or:

$$T_{\perp p} \propto B \quad (3.4)$$

In a similar vein for the parallel direction, under the assumption of no dissipation, we have:

$$\frac{d}{dt} \left( \frac{k_B T_{\parallel p} B^2}{n_p^2} \right) = 0 \quad (3.5)$$

or:

$$T_{\parallel p} \propto \left( \frac{n_p}{B} \right)^2 \quad (3.6)$$

These two conservation laws (Equations (3.4) and (3.6)) for the *double-adiabatic invariants* are also called *Chew–Goldberger–Low or CGL invariants* (for a bit more detailed discussion and derivation of CGL invariants, see Appendix B).

In the inner heliosphere, the magnitude of magnetic field ( $B$ ) varies with solar distance as  $B \propto r^{-1.5}$  (Hellinger et al., 2013; Hanneson et al., 2020), and the proton density varies as  $n_p \propto r^{-1.9}$  (Hellinger et al., 2013). If the CGL invariants were actively

being conserved, the radial dependence for the perpendicular and parallel temperatures would be:

$$T_{\perp p} \propto r^{-1.5} \quad (3.7)$$

$$T_{\parallel p} \propto r^{-0.8} \quad (3.8)$$

However, in-situ observations in the inner as well as outer heliosphere show a much flatter curve than those predicted by Equations (3.7) and (3.8). Based on Helios 1 and Helios 2 data, Hellinger et al. (2013) reported the value of exponents to be  $-0.58$  and  $-0.59$  for perpendicular and parallel temperatures respectively and  $-0.58$  for the scalar temperature for  $r \in [0.3, 1]$  au.

Flatter than expected temperature curves imply the existence of some mechanism which continues to heat the solar wind beyond the corona in both the parallel and perpendicular directions. Indeed, several studies (Coleman Jr, 1968; Verma et al., 1995; Sorriso-Valvo et al., 2007; MacBride et al., 2008) predict around  $1000 \text{ kJ/kg/sec}$  is being added as internal energy to the plasma at 1 au. The dissipation of this energy at least partially accounts for the flatter radial trend in solar-wind temperature than that predicted by the double adiabatic expansion assumption.

### 3.2.2 Anisotropy

In Section 2.2.2 we discussed the fact that because of anisotropy, VDFs have excess free energy that results in development of microkinetic instabilities, though we did not discuss the origin of such anisotropies. As we saw in Section 3.2.1, turbulence results in the transfer of heat from larger to smaller scales. However, in presence of an external background magnetic field the rate at which transfer occurs is not identical in each direction. Because of an uneven transfer along the parallel and perpendicular direction relative to the average magnetic field (inhibition along the direction of magnetic field), there is an imbalance between the amount of heating in different directions, resulting in anisotropy (Shebalin et al., 1983; Oughton et al., 1994).

### 3.2.3 Intermittency

The solar wind at 1 au exhibits localized structures that have been studied since the pioneering work of Burlaga (1968), Hudson (1970), Tsurutani & Smith (1979), and more recently by Ness & Burlaga (2001), Neugebauer (2006), ErdőS & Balogh (2008). Several studies have found evidence that plasma turbulence generates these structures dynamically (Matthaeus & Lamkin, 1986; Veltri, 1999; Osman et al., 2013). The structures are inhomogeneous and highly intermittent (Osman et al., 2011, 2013; Greco et al., 2008). Intermittency or burstiness in measured properties of turbulence is typically associated with the dynamical formation of coherent structures in space. These arise as a direct consequence of discontinuities in the magnetic field (Greco et al., 2008, 2009; Vasquez et al., 2007).

One method for identifying a discontinuity in a time series of magnetic-field (or any other field in general) data is Partial Variance of Increments (PVI) (Greco et al., 2008). PVI is a powerful and reliable tool for identifying and locating such regions and it is unbiased towards any special structure since it cares only about the discontinuities in the magnetic field. This also manifests as a shortcoming of the technique since one cannot use it to study different kinds of discontinuities like radial or tangential discontinuities. Greco et al. (2008) defines PVI as:

$$\mathcal{I}(t, \delta t) = \frac{|\Delta \mathbf{B}(t, \delta t)|}{\sqrt{\langle |\Delta \mathbf{B}(t, \delta t)|^2 \rangle}} \quad (3.9)$$

where,  $\Delta \mathbf{B}(t, \delta t) = \mathbf{B}(t + \delta t) - \mathbf{B}(t)$ , is the vector increment in magnetic field at any given time  $t$  and a time lag of  $\delta t$ .  $\langle \dots \rangle$  is the ensemble average over a period of time, and  $\mathcal{I}$  is the normalized PVI. For studying local structures induced by turbulence,  $\delta t$  is typically chosen to be, assuming the validity of Taylor's hypothesis (Taylor, 1938) which was found to be valid for inner heliosphere (Chasapis, 2021), of the order of  $d_i$ .

## 3.3 Linear and Non-linear Time Scales

Since turbulence is not the only process that governs the dynamics, we must compare its characteristic timescale with other with those of other relevant processes.

As we saw in Section 2.2.2, linear instabilities grow at growth rates of  $\gamma_{\max}$ . Inverse of  $\gamma_{\max}$  gives us a linear time scale associated with such microinstabilities.

$$\tau_{\text{lin}} = \frac{2\pi}{(\gamma_{\max}/\Omega_{\text{cp}})} \quad (3.10)$$

Here we have scaled time scale with the proton cyclotron frequency ( $\Omega_{\text{cp}}$ ) to get a dimensionless timescale. This gives us an idea of timescales required by such linear processes to affect the local plasma.

In a similar vein, one can compute nonlinear frequency associated with turbulence at any position  $\mathbf{r}$  for a lag length scale of  $\ell$  as follows<sup>2</sup>:

$$\omega_{\text{nl}} \sim \delta b_\ell / \ell \quad (3.11)$$

where  $\delta b_\ell$  is the change in the longitudinal magnetic field:

$$\delta b_\ell = \left| \hat{\ell} \cdot [\mathbf{b}(\mathbf{r} + \ell) - \mathbf{b}(\mathbf{r})] \right| \quad (3.12)$$

where  $\mathbf{b}$  is the total magnetic field expressed in local Alfvén speed units ( $\mathbf{b} = \mathbf{B}/\sqrt{\mu_0 n_p m_p}$ ). Thus nonlinear time scale has the expression:

$$\tau_{\text{nl}} = \frac{2\pi}{(\omega_{\text{nl}}/\Omega_{\text{cp}})} \quad (3.13)$$

These two processes under certain conditions might compete with each other and depending on the value of other kinetic or turbulent parameters one or the other may dominate. A simplistic understanding of this competition would imply that if one time scale is significantly smaller than the other, then the processes associated with former time scale will dominate the dynamics of the plasma. However, as we will see in Chapter 7 the situation is a bit more complicated than that.

<sup>2</sup> Ideally, velocity and not the magnetic field should be used for computing  $\omega_{\text{nl}}$ . However, neither of the spacecraft data we used has enough resolution for such computation. We thus fall back to using magnetic field under the assumption of Alfvénic fluctuations.

## Chapter 4

### DATASETS AND ANALYSIS METHODS

We utilized multiple datasets (both observational and theoretical) while working on this thesis. This chapter gives a brief overview of all the datasets. Table 4.2 summarizes these datasets and how they were used.

#### 4.1 Spacecraft datasets

##### 4.1.1 Wind

The Wind spacecraft was launched on November 1, 1994 as part of international Solar terrestrial Physics (ISTP) with the objective of studying plasma processes in the solar wind near earth and in magnetosphere and ionosphere (Acuna et al., 1995). Wind is spin stabilized and makes one complete rotation every  $\sim 3$  seconds about axis aligned to perpendicular to the ecliptic plane (Acuna et al., 1995; Wilson III et al., 2021). Wind's instruments collectively produce  $\sim 1,100$  data variables or datasets (Wilson III et al., 2021). The instruments of interest to this thesis are the Magnetic Field Investigation (MFI) and the Faraday Cup (FC).

##### MFI

MFI consists of two fluxgate magnetometers mounted on a boom at distances of 8 and 12 meters from the spacecraft (Lepping et al., 1995). Though occasionally MFI can provide data as fast as 44 Sa/s<sup>1</sup> with great accuracy ( $< 0.08$  nT), though 10.9 Sa/s is the standard product and was used for this thesis.

---

<sup>1</sup> Samples per second.

## FC

The Solar Wind Experiment (SWE) suite includes two Faraday cups (FC) (Ogilvie et al., 1995). Each cup measures the current from incoming charged ions for a different energy bin during each rotation measuring current in 20 different look directions. It has 31 energy bins which defines its resolution of the VDF. Since each rotation lasts about 3 seconds, it takes FC roughly 93 seconds to collect the full spectra. The current can then be converted to velocity of particle assuming an appropriate charge to mass ratio. Since it takes roughly 93 seconds to get the full VDF, we get one measurement of parameters like density, velocity, temperature etc. every 93 seconds. Consequently, while pairing FC data with MFI data, we further averaged MFI data to 93 Sa/s. For an in depth discussion of extracting VDF from FC observation and computation of higher order moments see Maruca (2012a).

## The `wnd` dataset

In this thesis we use the Wind data from 1994 to 2008, which henceforth shall be referred as `wnd` dataset. In the initial data cleaning process we discarded any point which had  $R_p < 0.1$  or  $R_p > 10$ . We also only selected data from the pristine solar wind and discarded everything within the bow shock region of the Earth. A more detailed description of the data selection process can be found in Maruca (2012a, §4.1).

**Computing linear growth rate and non-linear frequency:** In order to compute the value of linear growth rates at any point, we use the methodology mentioned in Section 2.2.3 by using the local values of  $R_p$  and  $\beta_{\parallel p}$ . We computed  $\omega_{nl}$  using Equation (3.11), where we used  $x$ -component<sup>2</sup> of magnetic field for the longitudinal direction of  $\mathbf{B}$ . Use of  $\mathbf{x}$ -component instead of radial component introduces a small error in the computation of  $\omega_{nl}$  since the magnetic field at 1 au is not perfectly aligned with the radial direction (on average, the angle between magnetic field and radial direction is 45°). The field also strongly fluctuates around the average value. Alfvén

---

<sup>2</sup> For Wind,  $x$ -direction is defined by the line joining the Earth and the Sun.

speed was computed using the average field from MFI data and  $n_p$  from FC as per equation Equation (1.13). For lag we used  $\ell = 1/k_{\max}$ , where  $k_{\max}$  is the wave number corresponding to  $\gamma_{\max}$ . The lag of was taken as  $1/k_{\max}$  in order to ensure that both  $\gamma_{\max}$  and  $\omega_{nl}$  are being computed at the same scale.

#### 4.1.2 MMS

Magnetospheric Multiscale (MMS) is a constellation of four spacecraft which was launched by NASA on March 12, 2015. Main objective of the mission was to study how reconnection happens in a collisionless plasma in the Earths magnetosphere (Russell et al., 2016). MMS has 6 major instrument suites (Russell et al., 2016) and in this thesis we used the data from FIELDS and Fast Plasma Investigation (FPI).

### FIELDS

The FIELDS instrument suite consists of 2 different kind of fluxgate magnetometers, a search coil magnetometer and an electron drift instrument (Torbert et al., 2016). The flux gate magnetometers are mounted at the end of two 5 m booms of each spacecraft (Russell et al., 2016). The cadence of this FGMs is 128 Hz meaning we get 128 samples of magnetic field vector every 1 second with an accuracy of  $\sim 0.1$  nT (Russell et al., 2016; Torbert et al., 2016).

### FPI

FPI uses electrostatic analyzer to measure the VDF of ions and electrons (Pollock et al., 2016). It has  $180^\circ$  instantaneous polar field of view at a resolution of  $15^\circ$ . We use the proton density and temperature anisotropy which are among the standard products of FPI. FPI works in 2 modes:

- (a) **Slow/Survey mode:** which gives full 3-D VDF of ions every 1 second.
- (b) **Fast/Burst Mode:** which gives 1 measurement of ion VDF every 150 ms.

## mms dataset

Though in burst mode cadence of FPI is very high they generally last for only a few minutes. In our studies we thus used data from several different burst modes spread over multiple years and when the spacecraft was in magnetosheath. Table 4.1 lists out all the dates and time from which data was used as well as gives value of the plasma parameters.

Once we have the required parameters we compute other derived parameters like  $\gamma$  and  $\omega_{nl}$  in the same way as mentioned in Section 4.1.1. We refer to the complete MMS dataset as `mms`.

### 4.1.3 PSP

Parker Solar Probe was launched on August 12, 2018 with the objective to understand the dynamical structure of the sun, study and find the processes behind coronal heating and find out the process that accelerates energetic particles (Fox et al., 2015). The spacecraft has 4 major instrument suites: FIELDS, SWEAP, WISPR, IS $\odot$ IS(Fox et al., 2015).

## FIELDS

With main objective of measuring wave and turbulence in the inner heliosphere FIELDS measures the magnetic field using both, search coils and fluxgate magnetometers (Bale et al., 2016). All three magnetometers are mounted on a boom (search coil at 3.08 m and 2 magnetometers at 1.9 m and 2.7 m). For this thesis we use the magnetic field data from flux gate magnetometer. At the highest cadence magnetometer can record field at a rate of 292.969 Sa/s or 256 Sa/NYS, where 1 NYsecond is defined as 0.837 seconds (Bale et al., 2016)<sup>3</sup>. Though for this thesis we mostly used data recorded at a slightly lower cadence of 64 Sa/S unless otherwise specified.

---

<sup>3</sup> An alternate and definitely more magically colorful definition of a New York second is given by Sir Terry Pratchett as “The shortest unit of time in the multiverse is the New York Second, defined as the period of time between the traffic lights turning green and the cab behind you honking.”

## SWEAP

Solar Wind Electrons Alphas and Protons or SWEAP is the particle instrument suite on PSP and is comprised of 4 sensor instruments and provides complete measurement of electron, alpha and protons which makes up for almost 99% of solar wind ([Kasper et al., 2016](#)). Solar Probe Cup (SPC) and Solar Probe Analyzer (SPAN) make up SWEAP. We are mostly interested in SPC which is a fast Faraday cup and looks directly at the sun to measure the ion flux and its angle. The native cadence of SPC is 1 Hz or 1 Sa/s at an angular resolution of  $10^\circ$ , though in another mode cadence can go as high as 16 Hz at  $1^\circ$  resolution ([Kasper et al., 2016](#)). For this thesis we used 1 Hz data from SPC. Though for the purpose of computation of anisotropy we resampled the data to 0.1 Hz (see Chapter [7](#)).

### psp dataset

We used the PSP data from its first encounter with the Sun (October 31 to November 11, 2018). From SPC we got the radial proton temperature/thermal speed. Since SPC only measures radial temperature, and proton temperature is significantly anisotropic ([Huang et al., 2020](#)), for computation of  $\beta_{\parallel p}$  we needed to ensure that the temperature we were measuring was indeed parallel temperature. Thus, we only considered data points where magnetic field was mostly radial. Any interval where the angle between  $B_r \hat{\mathbf{r}}$  and  $\mathbf{B}$  was more than 30 degrees was not considered. This ensured that the temperature measured by SPC was indeed the parallel temperature. We compute temperature anisotropy at a much lower cadence than the temperature measurement ( $\sim 0.1$  Sa/S) using the methodology described in [Huang et al. \(2020\)](#). Once we have the anisotropy data along with proton density and magnetic field strength we compute the  $\beta_{\parallel p}$  according to Equation [\(2.19\)](#). We then calculate  $\gamma$  and  $\omega_{nl}$  using the same methodology as mentioned in Section [4.1.1](#).

## 4.2 Simulation datasets

Though spacecraft provide plenty of in-situ data, because of several restrictions (e.g., cost, planning, resolution, and cadence) not every phenomena of plasma can be studied using spacecraft data. Thus physicists often use simulations to study different systems or verify predictions made by theories under certain conditions. For space plasmas there are 3 types of simulations that are usually carried out.

### 4.2.1 MHD Simulations

MHD simulation treats the plasma as an electromagnetic, conducting fluid having one characteristic velocity and temperature and studies its dynamics by numerically solving the required MHD equations. For more details about the underlying physics and some of the relevant equations see ([Hossain et al., 1995](#)).

### 4.2.2 Hybrid Simulations

In hybrid simulations, instead of treating the whole system as a fluid, electrons are treated as massless fluid and protons are treated as massive particles. For the details of such simulations and equations used for it refer to ([Terasawa et al., 1986](#); [Vasquez, 1995](#); [Parashar et al., 2009](#)).

### 4.2.3 Kinetic Simulations

In kinetic simulations with particle in cell (PIC) we solve Vlasov equation (see Equation [\(2.12\)](#)) along with Maxwell's equation (see Equations [\(1.3\)](#) to [\(1.6\)](#)) by treating plasma as a collection of individual particles. PIC simulations are often performed on either a 2.5D system or a full 3-D system.

## 3-D PIC Simulations

In full 3-D system the parameters are setup such that the vectors can fluctuate in all three directions. For this thesis, we used the output of a fully kinetic 3-D simulation performed by ([Roytershteyn et al., 2015](#)). In the simulation the system was initially perturbed ( $|\delta\mathbf{B}^2| = \mathbf{B}_0^2$ ) and was then left to evolve under its own forcing.

The undisturbed state of particle distribution was Maxwellian (for both proton and electron) at equal temperature ( $T_p = T_e$ ). Some other parameters were  $\beta_p = \beta_e = 0.5$ ,  $R_p = 1$ ,  $\omega_{pe}/\Omega_{ce} = 2$ ,  $m_p/m_e = 50$  and the background magnetic field was in  $z$ -direction. Size of the box was  $l \approx 42 d_p$ , with a resolution of  $2048^3$  cells. Average number of particles in each cell was 150 making a total of  $\sim 2.6 \times 10^{12}$ . We refer to this dataset as `ros`.

## 2.5-D Simulations

In case of a 2.5D simulation the plasma parameters are allowed to vary only in 2 dimensions, though they have all 3 components. Depending on the direction of background magnetic field one can further classify 2.5-D simulation in following classes:

- (a) **2.5D perpendicular PIC simulation:** The parameters are allowed to vary only in 2 spatial dimensions with background magnetic field perpendicular to the simulation plane.
- (b) **2.5D oblique PIC simulation:** The parameters are allowed to vary only in 2 spatial dimensions with background magnetic field neither parallel nor perpendicular to the simulation plane.
- (c) **2.5D parallel PIC simulation:** The parameters are allowed to vary only in 2 spatial dimensions with background magnetic field parallel to the simulation plane.

In this thesis we used both perpendicular and parallel simulations. For the 2.5-D perpendicular simulation we used the output from a P3D code ([Zeiler et al., 2002](#)). The initial conditions were such that we have  $m_p/m_e = 25$ ,  $T_p = T_e$ ,  $\beta_p = \beta_e = 0.6$ ,  $\delta B = 0.5 B_0$  and the length of the box was  $l = 149.6 d_p$  at a resolution  $4096^2$  of with each cell having an average of 3200 particles with each species resulting in a total of  $1.07 \times 10^{11}$  particles. For more details on the simulation refer to ([Parashar et al., 2018a](#)). We refer to this dataset as `149p6`.

We also used a 2.5-D parallel simulation where the background magnetic field was in the plane with  $\mathbf{B}_0 = B_0 \hat{x}$ ,  $m_p/m_e = 25$ ,  $\omega_{pe}/\Omega_{ce} = 8$ ,  $\beta_p = \beta_e = 0.6$ . The size

of the box was  $l_{\parallel} = 149.6 d_p$  (in parallel direction) and  $l_{\perp} = 37.4 d_p$  (in perpendicular direction) at a resolution of  $4043 \times 1000$  with an average of 800 particles/cell resulting in a total of  $6.5 \times 10^9$  particles. More information about this simulation can be found in ([Parashar & Gary, 2019](#); [Gary et al., 2020](#)). We refer to this dataset as **kaw**.

For 2 datasets of simulations (**kaw** and **149p6**), once we have the value of  $R_p$  and  $\beta_{\parallel p}$  we compute  $\gamma$  and  $\omega_{nl}$  in the same way as mentioned in Section [4.1.1](#). For the case **ros**, for computation of  $\omega_{nl}$ , because of some computational limitations, the value of lag was kept fixed at  $1 d_p$ .

Table 4.1: Burst data duration and median values of some plasma parameters

Date (YYYYMMDD)	Time (HH:MM:SS) (GMT)		Median Values
	Start HH:MM:SS	End HH:MM:SS	
20160111	00:57:04	01:00:33	$n_p = 52.04 \text{ cm}^{-3}$ , $v_p = 261.47 \text{ km/s}$ , $T_p = 2.53 \times 10^6 \text{ K}$ , $R_p = 1.09$ , $\beta_{\parallel p} = 6.54$
20160124	23:36:14	23:47:33	$n_p = 32.57 \text{ cm}^{-3}$ , $v_p = 242.21 \text{ km/s}$ , $T_p = 3.98 \times 10^6 \text{ K}$ , $R_p = 0.99$ , $\beta_{\parallel p} = 12.57$
20170118	00:45:54	00:49:43	$n_p = 198.26 \text{ cm}^{-3}$ , $v_p = 135.11 \text{ km/s}$ , $T_p = 1.31 \times 10^6 \text{ K}$ , $R_p = 0.97$ , $\beta_{\parallel p} = 10.66$
20171226	06:12:43	06:52:22	$n_p = 22.29 \text{ cm}^{-3}$ , $v_p = 243.50 \text{ km/s}$ , $T_p = 2.66 \times 10^6 \text{ K}$ , $R_p = 1.04$ , $\beta_{\parallel p} = 4.29$
All			$n_p = 2.94 \text{ cm}^{-3}$ , $v_p = 240.15 \text{ km/s}$ , $T_p = 2.74 \times 10^6 \text{ K}$ , $R_p = 1.01$ , $\beta_{\parallel p} = 5.34$

Table 4.2: Datasets used in this study

Dataset	Type of data	median values	List of chapters
149p6	PIC Simulation (2.5-D)	$R_p = 0.89,$ $\beta_{\parallel p} = 0.67$	Chapters 5 and 7
kaw	PIC Simulation (2.5-D)	$R_p = 0.83,$ $\beta_{\parallel p} = 0.64$	Chapters 5 and 7
ros	PIC Simulation (3-D)	$R_p = 1.04,$ $\beta_{\parallel p} = 0.84$	Chapters 5, 7 and 8
mms	Spacecraft Observation (Magnetosheath)	see Table 4.1	Chapters 5 and 7
wnd	Spacecraft Observation (Solar Wind at 1 au)	$R_p = 0.50,$ $\beta_{\parallel p} = 0.69$	Chapters 5 and 7
psp	Spacecraft Observation (Solar Wind at 0.2 au)	$R_p = 1.44,$ $\beta_{\parallel p} = 0.50$	Chapters 6 and 7

## Chapter 5

### ASSOCIATION OF INTERMITTENCY AND MICROINSTABILITIES

#### 5.1 Overview

As discussed in Section 2.3, weakly collisional space plasmas are rarely in local thermal equilibrium and often exhibit non-Maxwellian electron and ion velocity distributions that lead to the growth of microinstabilities (see Section 2.3). These instabilities play an active role in the evolution of space plasmas (see Section 2.3), as does ubiquitous broadband turbulence induced by turbulent structures (see Section 3.2). This Chapter compares linear and non-linear phenomena of a variety of 2.5-dimensional and 3-dimensional Particle-In-Cell (PIC) simulation for the forward cascade of Alfvénic turbulence in a collisionless plasma against the same properties of turbulence observed by the Magnetospheric Multiscale Mission (MMS) in the terrestrial magnetosheath and the Wind spacecraft in the solar wind at 1 au.

Both the simulation and the observations show that strong temperature anisotropies and growth rates occur highly intermittently in the plasma, and the simulation further shows that such anisotropies preferentially occur near current sheets. This suggests that, though microinstabilities may affect the plasma globally, they act locally and develop in response to extreme temperature anisotropies generated by turbulent structures.

Section 5.2 starts with the introduction of the topic and the motivation for such a study. We discuss the data analysis technique in Section 5.3 (PIC data in Section 5.3.1 and spacecraft data in Section 5.3.2). Section 5.4 presents the result highlighting the

observations made using the different datasets and ends with the conclusion and some discussion of further possibilities in Section 5.5.<sup>1</sup>

## 5.2 Introduction

The focus of this study was protons and in particular their temperature anisotropy ( $R_p$ ) (see Equation (2.18)). As discussed in Section 2.2, a sufficient departure of  $R_p$  from  $R_p = 1$  triggers one or more modes of microinstability. These linear instabilities and their thresholds are predicted by linear Vlasov theory (see Section 2.2) under the assumption of a homogeneous background of magnetic field. However, the space plasma is rarely homogeneous which raises a fundamental issue of reconciling the assumptions of theory of microinstabilities with the observed state of space plasma. Multiple studies have shown space plasma to be highly structured and thus inhomogeneous (Burlaga, 1968; Tsurutani & Smith, 1979; Ness & Burlaga, 2001; Osman et al., 2012a,b; Greco et al., 2012). This has been a persistent question in the field and a prime motivation for our work which formalizes the implications of Osman et al. (2012a).

As was highlighted in Section 2.4, owing to inhomogeneous nature of the plasma background an ideal study would include the effect of these background inhomogeneities in computing the growth rates. However we do not have any such established methodology and development of such a method is beyond the scope of this study. We thus are restricted to use the established theory of microinstabilities, and calculate instability thresholds from linear Vlasov equations as discussed in Section 2.1.

## 5.3 Data and Analysis

### 5.3.1 PIC Simulation

Linear Vlasov calculations were applied to the output of a variety of fully kinetic, particle-in-cell (PIC) simulation in homogeneous, collisionless, magnetized plasmas. Table 4.2 gives detail of different simulation and the starting value of important parameters of each data set.

---

<sup>1</sup> Part of this study was published in Qudsi et al. (2020a).

For 2.5-D simulations, though all vector quantities (like magnetic field  $\mathbf{B}$ , current density  $\mathbf{J}$  etc.) had three components they varied only in the  $xy$ -plane for simulation `149p6` and perpendicular to the  $xy$ -plane for simulation `kaw` (see Chapter 4 for a detailed discussion of different types of dataset used in this study). For `149p6` the initial conditions were chosen such that the particle distribution was Maxwellian,  $\beta_p = \beta_e = 1.2, R_p = 1, T_p = T_e$  and the rms value of fluctuations in magnetic and velocity fields were half of the background values. For `kaw` the simulation had  $\beta_p = \beta_e = 0.6, R_p = 1, T_p = T_e$  as the initial condition whereas for the full 3-D simulation (`ros`) we had  $\beta_p = \beta_e = 0.5, R_p = 1, T_p = T_e$  and the background magnetic field was in  $z$ -direction. Table 4.2 lists out the details of all three simulations (and other datasets) in tabular form. It is worth noting that high  $\beta$ -values as well as values much lower than 1 makes the PIC computations very expensive and thus were avoided. After the initial condition was finalized, the system was allowed to evolve without any external forcing. Fluctuation in the observed magnetic and velocity fields produce and drive the turbulence in the plasma.

Once the simulation data was ready, we computed the value of linear growth rates ( $\gamma_{\max}$ ) at each point using methodology discussed in Section 2.2.3. Results pertaining to this analysis is discussed in Section 5.4.1

### 5.3.2 Space Observations

Similar analysis was carried out on data from two separate space missions: MMS and Wind. MMS is a constellation of four identical spacecraft designed to study reconnection in the magnetosphere of the Earth (Burch et al., 2016). We used proton density and temperature-anisotropy data from the Fast Plasma Investigation (FPI) and magnetic-field data from the Fluxgate Magnetometer (FGM). In burst mode FPI measures one proton distribution every 150 ms (Pollock et al., 2016), and the cadence of FGM is 128 Hz (Russell et al., 2016) (see Section 4.1.2 for a more detailed discussion of MMS and some of its instruments).

The measured temperature-anisotropy and magnetic field vectors were used to compute the value of the linear instability growth rates ( $\gamma_{\max}$ ) for each point in the time series using the same methodology as described in Section 2.1. Though the analysis was carried out on several intervals of burst-mode (high cadence) measurements, here only results from a 40-minute long period of burst data from 26-12-2017 starting at 06:12:43 UTC is being presented (see Table 4.1). This period was chosen in part because of its relatively long duration compared to typical burst mode intervals. During this period, average proton density was  $22 \text{ cm}^{-3}$ , the average value of  $\beta_{\parallel p}$  was 4.5 and average bulk velocity of the plasma was 238 km/s. Parashar et al. (2018b) describes this data interval in more detail.

For the case of solar wind, we used the data from Wind spacecraft's Faraday Cup (FC) and Magnetic Field Investigation (MFI) instruments (see Section 4.1.1 for a more detailed discussion of instruments and dataset).

## 5.4 Results

### 5.4.1 PIC simulation

Figures 5.1 to 5.3 show five parameters —  $R_p$ ,  $\beta_{\parallel p}$ ,  $J_z$ ,  $\gamma_{\parallel \max}$  and  $\gamma_{\# \max}$  — across the simulation box for three different simulations (149p6, kaw and ros respectively). For the 3-D case (Figure 5.3), we show the variation of parameters for a selected slice of  $xy$ -plane.

Panels (a) to (c) of each (Figures 5.1 to 5.3) show the three parameters —  $R_p$ ,  $\beta_{\parallel p}$ , and  $J_z$  — across the simulation box. In all the cases the system is strongly turbulent and exhibits structures of various scales. The extreme values of each parameter occur in distinct regions that occupy only small fractions of the total volume. That is, these quantities are intermittent, which is correlated with the existence of sharp gradients and coherent structures (Greco & Perri, 2014; Matthaeus et al., 2015; Greco et al., 2016; Perrone et al., 2016, 2017). Further, extreme values of  $R_p$  and  $\beta_{\parallel p}$  reside near (but are not exactly coincident with) extreme values of  $J_z$ . These concentrations

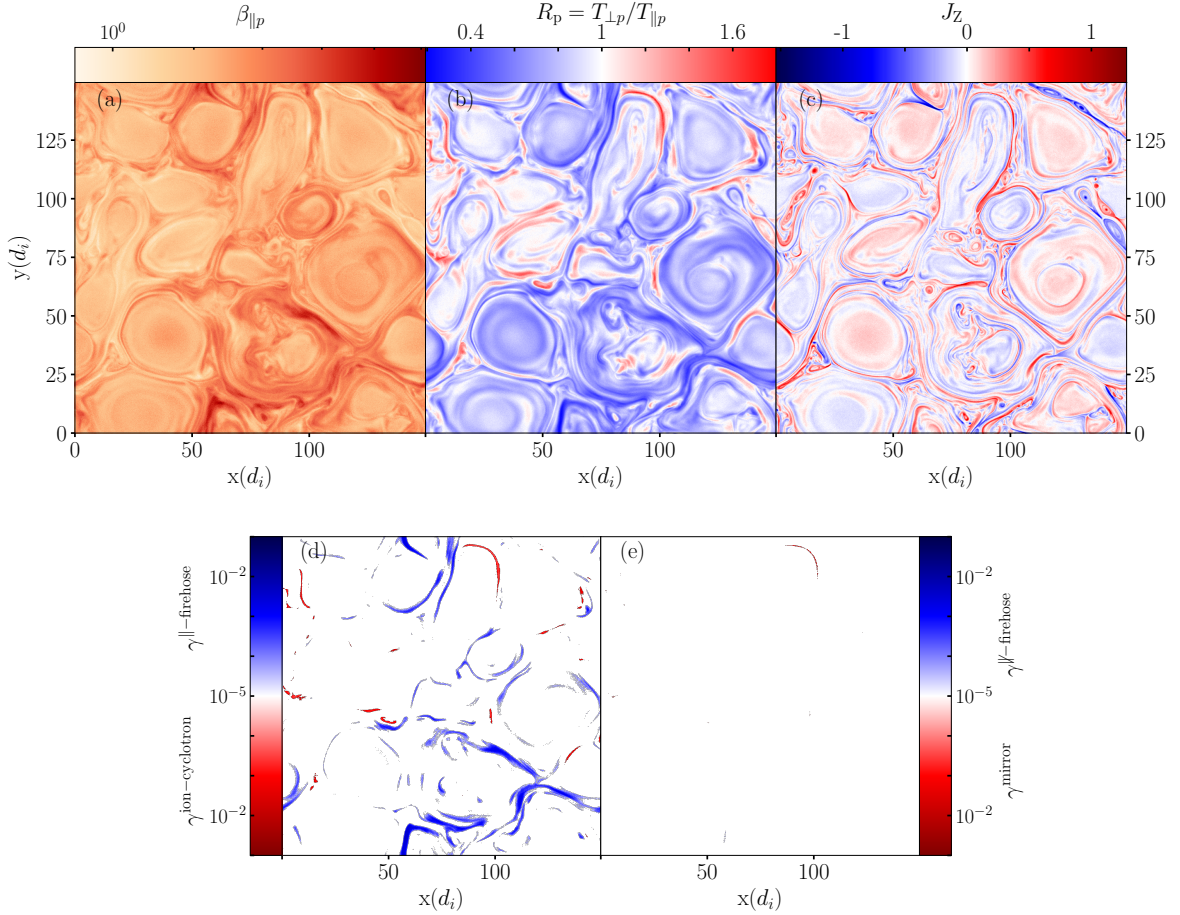


Figure 5.1: Colorplot of (top row, left to right)  $\beta_{\parallel p}$ ,  $R_p$  and  $J_z$  for 149p6 dataset. Panel (d) and (e) (bottom row) show the spatial distribution of  $\gamma_{\max}$  for parallel and oblique propagation respectively corresponding to first two panels. *Figure reproduced from Qudsi et al. (2020a) with the permission of AIP Publishing* (see Appendix D).

of current densities frequently correspond to current sheets, as reported by Parashar & Matthaeus (2016).

Using the method described in Section 2.2.3 and chapter 4, we computed  $\gamma_{\max}$  for the  $(\beta_{\parallel p}, R_p)$ -pair at each grid point of the simulation box, where  $\gamma_{\max}$  is the maximum value of growth rate for all possible values of propagation vector ( $\mathbf{k}$ ). The fourth and fifth Panels (d) and (e) of Figures 5.1 to 5.3 show the spatial distribution of growth rates for the solutions with positive growth rates, corresponding to the first two panels of the same figure. As described in Section 2.2.3, for  $\gamma_{\max}$ , we imposed a cut-off at

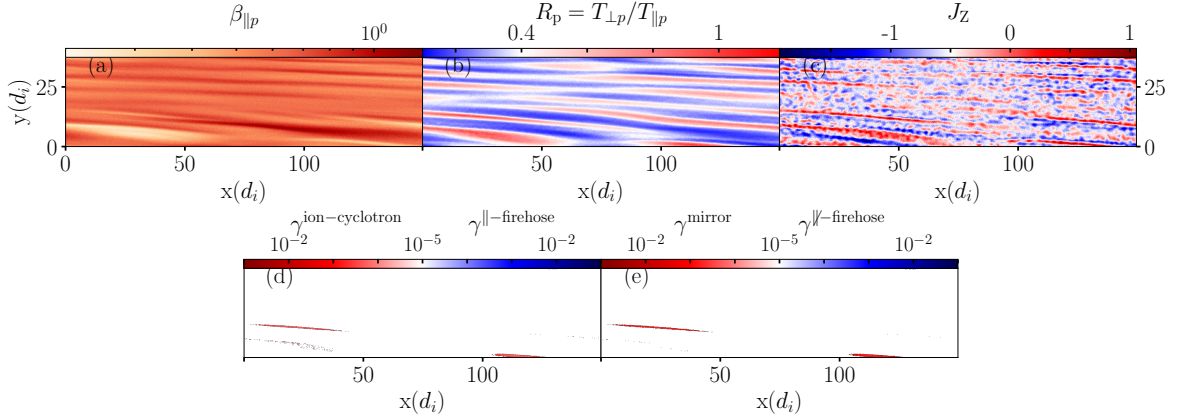


Figure 5.2: Colorplot of (top row, left to right)  $\beta_{\parallel p}$ ,  $R_p$  and  $J_z$  for **kaw** dataset. Panel (d) and (e) (bottom row) show the spatial distribution of  $\gamma_{\text{max}}$  for parallel and oblique propagation respectively corresponding to first two panels.

$10^{-5} \Omega_p$ ; thus growth rates less than  $10^{-5} \Omega_p$  are considered to be 0. The Panel (d) of each figure (Figures 5.1 to 5.3) corresponds to the parallel modes (cyclotron for  $R_p > 1$  and parallel firehose for  $R_p < 1$ ), whereas the Panel (e) are for the oblique propagation (mirror for  $R_p > 1$  and oblique firehose for  $R_p < 1$ ). The paucity of blue color in the fifth panel of Figures 5.1 and 5.2 implies that the  $\beta_{\parallel p}$  (and/or  $R_p$ ) was rarely high (low) enough to excite any mode of oblique firehose instability.

Comparing Panel (b) to Panel (d) and (e) of these figures, we see that values of  $\gamma_{\text{max}} > 0$  are concentrated in distinct, thin regions of the  $xy$ -plane where extreme values of temperature anisotropy also occur. We also note that, for Figure 5.1 because the simulation is 2.5D with  $\mathbf{B}_0$  perpendicular to the simulation plane, the growth of instabilities such as the proton cyclotron and the parallel proton firehose with maximum growth at  $\mathbf{k} \times \mathbf{B}_0 = \mathbf{0}$  is suppressed. However, for the other two simulations (Figures 5.2 and 5.3) that is not the case. Consequently, we see a lot of parallel instability in Figure 5.3 and a much higher value of average growth rate for **kaw** and **ros** datasets compared to **149p6** (see Figure 7.5 and associated discussion). However, despite not being suppressed in the parallel direction, parallel instabilities in Figure 5.2 remain relatively sparse because of very low value of  $\beta_{\parallel p}$  (see Table 5.1). Comparatively Figure 5.3 shows much less sparsity as a consequence of high value of  $R_p$  over

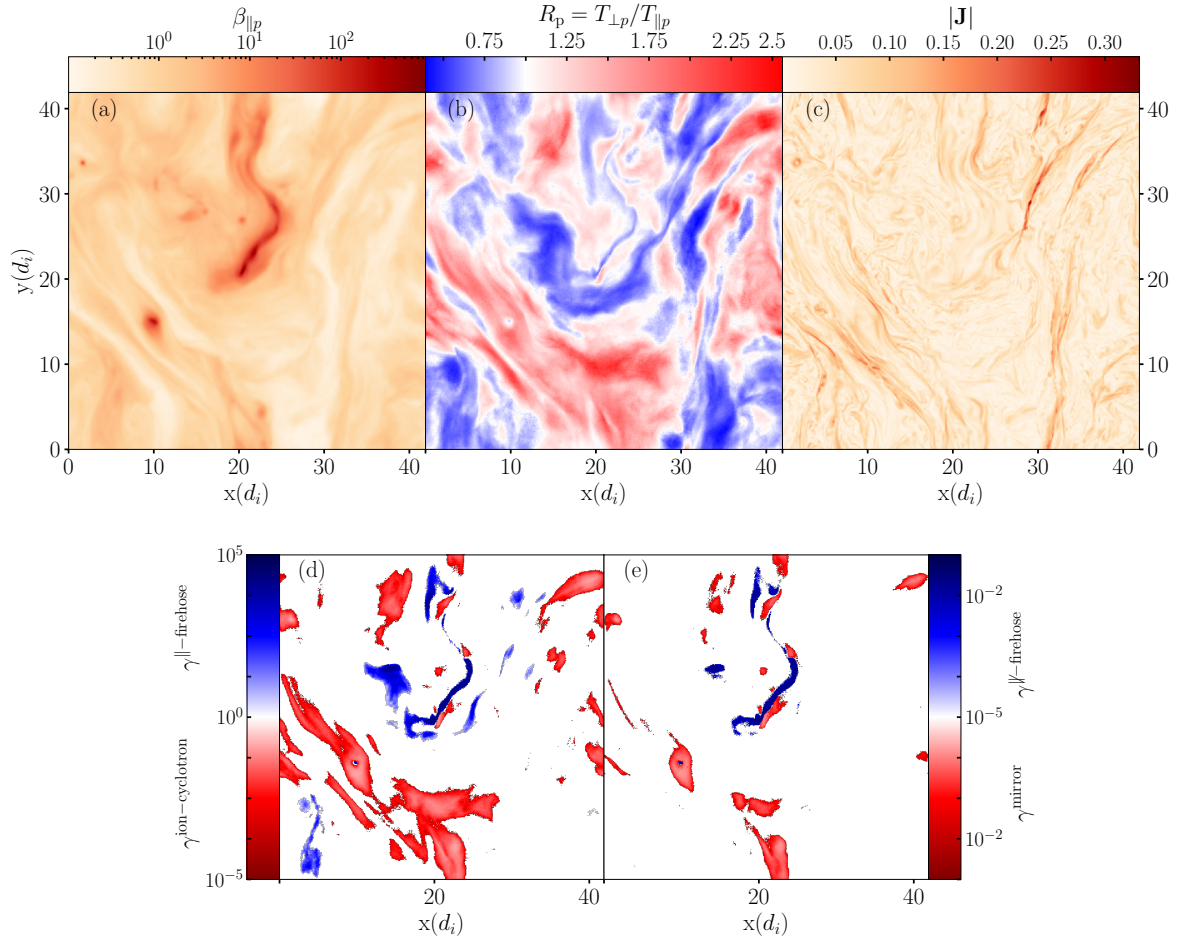


Figure 5.3: Colorplot of (top row, left to right)  $\beta_{\parallel p}$ ,  $R_p$  and  $J_z$  for **ros** dataset. Panel (d) and (e) (bottom row) show the spatial distribution of  $\gamma_{\max}$  for parallel and oblique propagation respectively corresponding to first two panels.

an extended region of the simulation box.

### 5.4.2 Spacecraft Observations

Figure 5.4 and Figure 5.5 show a typical portion of the time series data from two spacecraft: MMS and Wind. The panels, from top to bottom show  $R_p$ ,  $\beta_{\parallel p}$ ,  $|\mathbf{J}|$  and maximum growth rates ( $\gamma_{\max}$ ) for parallel and oblique instabilities respectively for both the spacecraft. Time intervals were chosen so that the figures showed approximately equal numbers of correlation time scales in the magnetosheath and solar wind at 1 au. For magnetosheath 10 minute corresponds to roughly 20  $\tau_{\text{cr}}$  (Le et al., 1993; Gutynska et al., 2008) whereas for solar wind which has a correlation time length of about 55 minutes the interval of 24 hours corresponds to about 25 times  $\tau_{\text{cr}}$  (Matthaeus & Goldstein, 1982; Wicks et al., 2010).

Both the Figures 5.4 and 5.5 show an intermittent distribution of instability growth rates, though in case of Wind since the variation in  $\beta_{\parallel p}$  is much smaller than that observed in magnetosheath the number of unstable points are significantly smaller. Table 5.1 lists out the variation in these parameters for all the different cases discussed so far.

Comparing Figure 5.1 and Figure 5.4 we see that a larger fraction the MMS data (30%) are unstable versus grid points from the simulation (0.8%), with  $\gamma_{\max}$  values above the cut-off ( $10^{-5} \Omega_p$ ). This discrepancy arises in part because MMS data have much higher values of  $\beta_{\parallel p}$  than the simulation (median values of 4.5 and 1.2, respectively). Furthermore, Servidio et al. (2015) found that, for a given value of  $\beta_{\parallel p}$ , simulations of the turbulence type, like in the present 2.5D cases, generally admit less extreme temperature-anisotropy than are seen in space observations, because typical simulations are of modest size resulting in modest Reynolds number and lack large scale coherent driving.

The time series for MMS observation (Figure 5.4) exhibits intermittent structure in the distribution of growth rates that are similar to what we see in Panels (d) and (e) of Figure 5.1 for simulation. Figure 5.6, which shows the comparison of the time

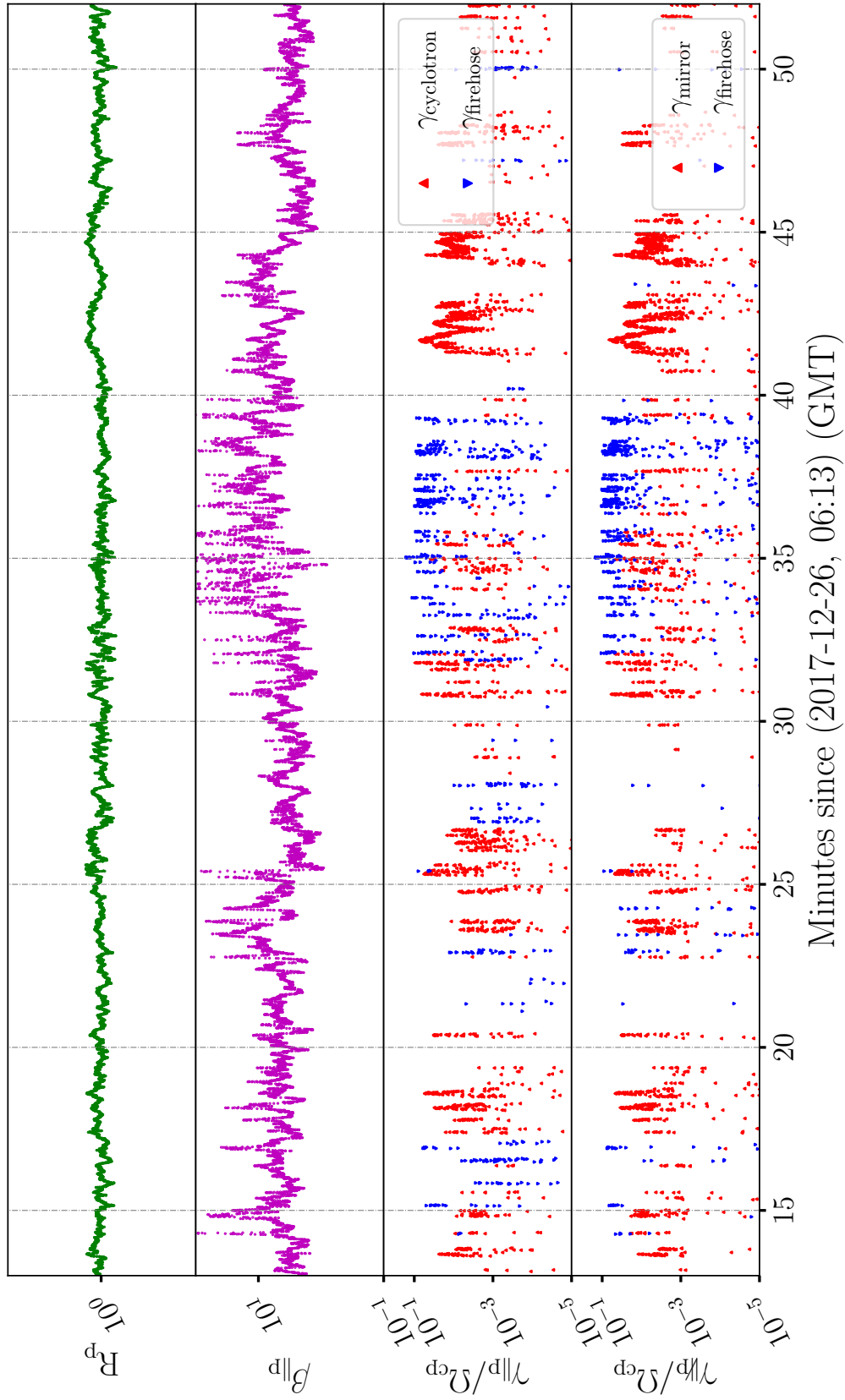


Figure 5.4: Time series plot of proton anisotropy ratio ( $R_p$ ), proton parallel beta ( $\beta_{\parallel pp}$ ), total current density in  $nA/m^2$ , parallel instability growth rates (proton-cyclotron, in red and parallel firehose in blue), and oblique instability growth rates (mirror in red and oblique firehose in blue), as observed by MMS on 2017 December 26.

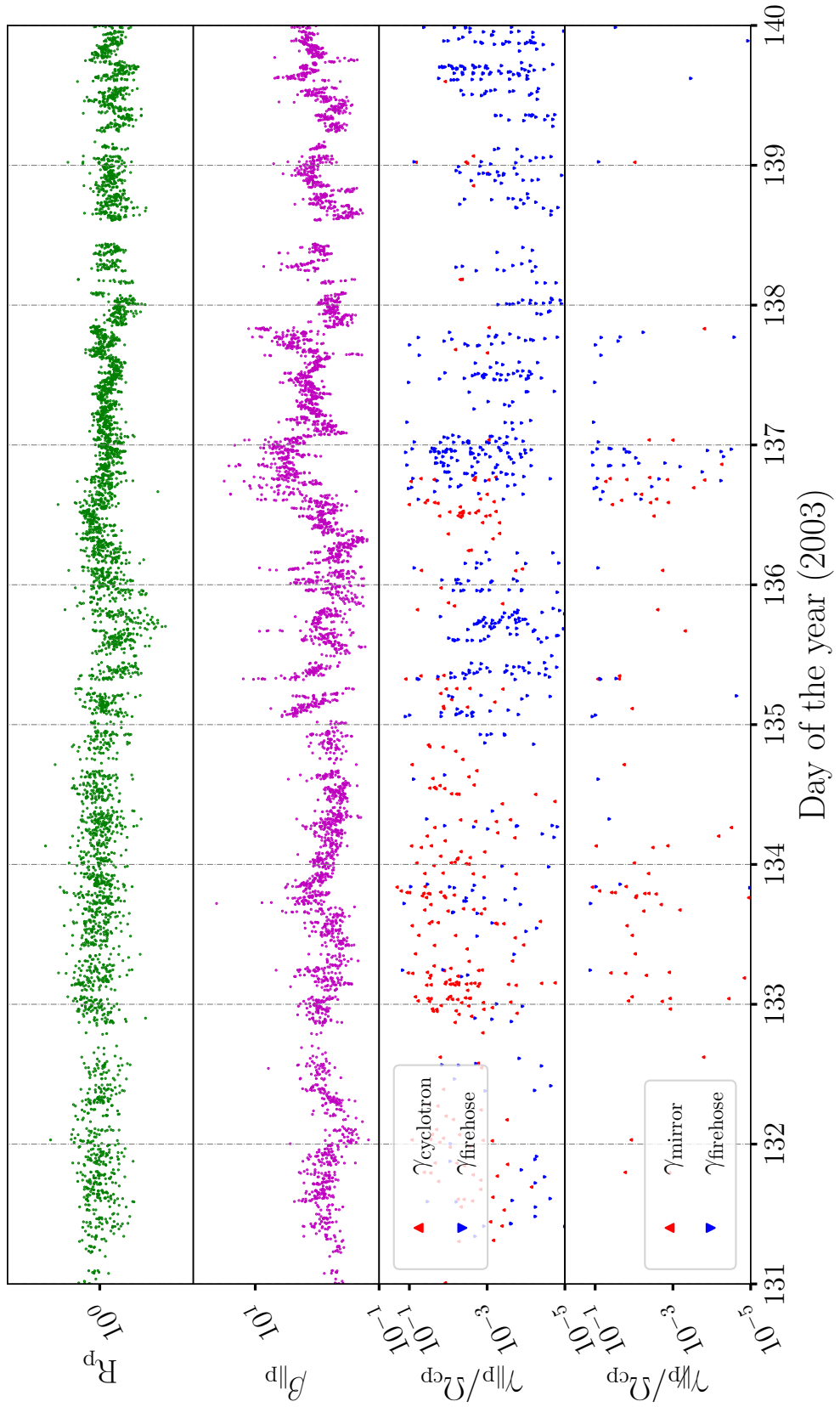


Figure 5.5: Time series plot of proton anisotropy ratio ( $R_p$ ), proton parallel beta ( $\beta_{\parallel p}$ ), parallel instability growth rates (proton-cyclotron, in red and parallel firehose in blue), and oblique instability growth rates (mirror in red and oblique firehose in blue), as observed by Wind.

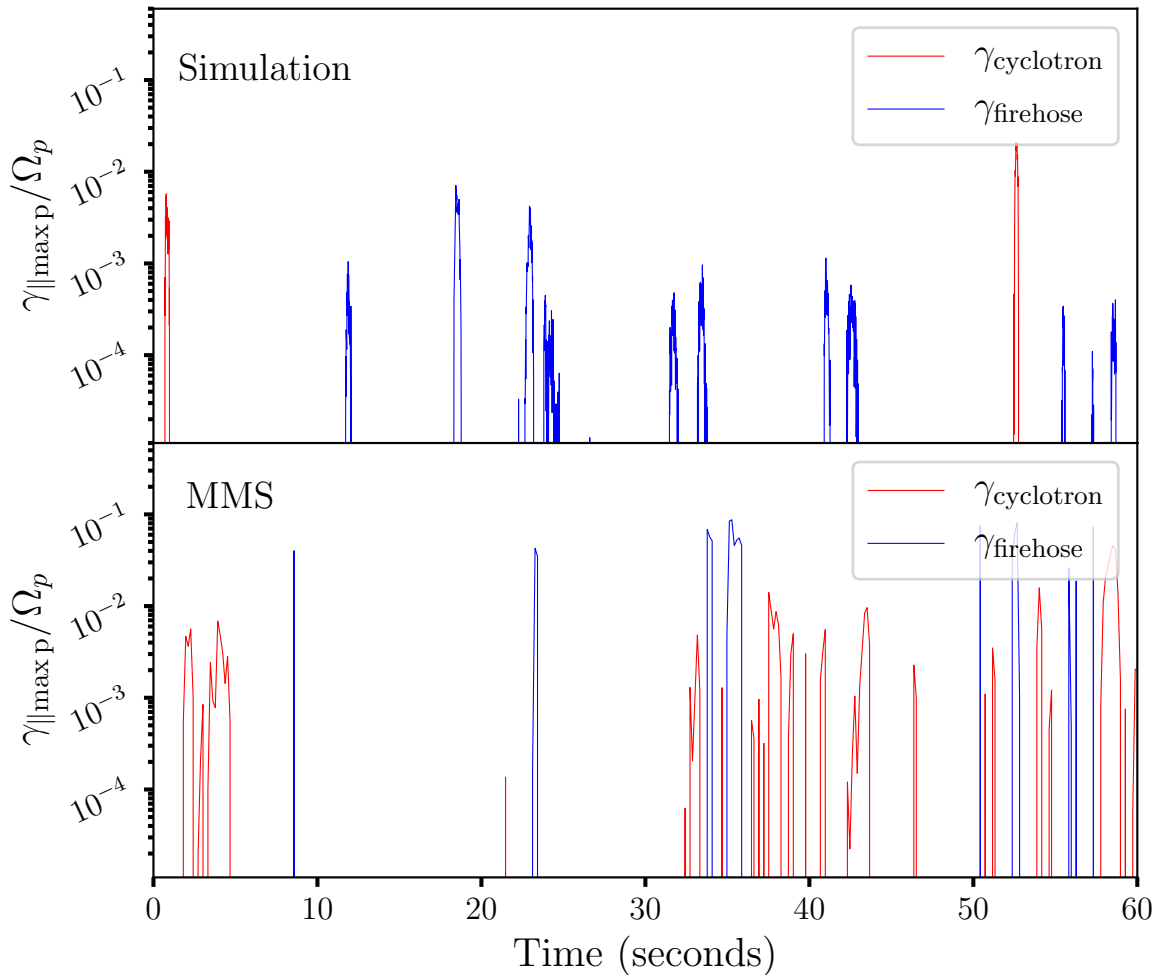


Figure 5.6: Comparison of simulation and MMS time series for  $\gamma_{\parallel max}$  values for a 1-minute period. The top panel shows the distribution for a 1-minute long flight through the simulation box and the lower panel shows the distribution of  $\gamma_{\max}$  starting at 06:34 on 2017 December 26. *Figure reproduced from Qudsi et al. (2020a) with the permission of AIP Publishing* (see Appendix D).

Table 5.1: Average values of parameters for different datasets

Name	Type of data	$\langle \beta_{\parallel p} \rangle$	$\langle R_p \rangle$	$n_\gamma/N$ (%)
149p6	Simulation	0.64	0.83	6.82
kaw	Simulation	0.61	0.89	0.90
ros	Simulation	0.84	1.04	16.39
mms	Spacecraft Observation (Magnetosheath)	4.29	1.04	24.51
wnd	Spacecraft Observation (Solar Wind)	0.69	0.50	14.22

series of simulation and MMS data for a 1 minute period, shows that qualitatively they have similar distribution. Time series for the simulation was computed by flying a virtual spacecraft, travelling at the plasma bulk speed (238 km/s, same speed as that of plasma during MMS observation), through the entire box at an angle of 75 degrees with respect to  $x$ -direction.

In Figure 5.4 the points of instabilities ( $\gamma_{\max} > 0$ ) are concentrated together, spreading over a small time interval lasting typically a few seconds (4-8 seconds) with sharp peaks. Though in this study we did not quantify the length scale of all the peaks, we found that typically they are spread over a length scale of  $\sim 20 - 40 d_i$ , where  $d_i$  is the ion-inertial length and the length scale was calculated using the flow speed of the plasma and the duration of the peak.

## 5.5 Discussions

In recent years, two different perspectives have been widely used to explain the behavior of the solar wind, magnetosheath, and similar space plasmas. In the first picture, the linear theory of plasma instability, at high  $\beta_{\parallel p}$ , for extreme  $R_p$ , different instability thresholds become active, thereby confining the plasma population to lower values of  $R_p$  (Gary et al., 2001; Kasper et al., 2002; Hellinger et al., 2006; Matteini et al., 2007; Klein et al., 2018). In the second, turbulence generates sharp gradients in the plasma that produce temperature anisotropy (Osman et al., 2011; Greco et al., 2012; Valentini et al., 2014; Parashar & Matthaeus, 2016).

These two theories have been non-reconcilable because of the basic underlying assumption. The linear theory of plasma instability assumes a homogeneous background magnetic field whereas turbulence relies on large fluctuations in the field. It was hitherto unclear if these two seemingly disparate processes—microinstabilities and turbulence—are connected in any way in configuration space. The apparent contradiction—homogeneity against intermittent inhomogeneity—between the two interpretations poses a question of fundamental importance in the study of space plasmas specifically and collisionless plasmas in general: How can an inhomogeneous phenomenon such as turbulence be consistent with temperature-anisotropy constraints derived from linear theory of homogeneous plasmas? Our simulations show that the turbulence indeed heats the plasma anisotropically, making it more susceptible to instability. But the simulation also shows that these anisotropies are strongly localized; furthermore the 2.5-D character of the simulation with a strong background magnetic field out of the simulation plane acts against the growth of the proton cyclotron and parallel proton firehose microinstabilities. Clearly, further studies are necessary to resolve this apparent contradiction.

Although there is no discussion of the consequences of electron anisotropies here, it should be noted that both simulations and magnetosheath observations (Gary et al., 2005) have shown that electron temperature anisotropies in collisionless plasmas can drive whistler instabilities which, in turn, scatter the electrons to establish a constraint

on the anisotropy of that species (Gary & Wang, 1996), in full analogy with the case of ion instabilities and anisotropy constraints discussed here.

In Figures 5.1 to 5.3 the regions of significant growth rates are close to the regions of peak current values. This suggests that current sheets are producing the extreme temperature-anisotropies that ultimately drive the instabilities. Note, though, that the high- $\gamma_{\max}$  regions and the high- $J_z$  regions do not perfectly overlap: they tend to be adjacent to each other rather than co-located, as seen by Greco et al. (2012). Thus, traditional methods of correlation calculation would be inadequate to quantify the relationship between these two structures. Instead, an analysis using cross correlations of these quantities (see, e.g., Parashar & Matthaeus, 2016) or joint distributions (see, e.g., Yang et al., 2017) to explore the causal connection between instabilities and turbulence-generated current sheets would be the next step forward.

In this study we found an explicit connection between intermittency in plasma turbulence and indication of the local enhancement of linear instability growth rates. Intermittency is clearly influential in the interpretation of observations, while its theoretical importance derives from its potential connection to the nature and statistics of dissipation Kolmogorov (1962); Karimabadi et al. (2013); Wan et al. (2016); Howes (2015); Matthaeus et al. (2015). The connection we have found here—that linear instability growth rates computed from (admittedly oversimplified) homogeneous plasma theory, also occur in intermittent bursts—adds to this emerging understanding of plasma dissipation. Previous studies found that pathways, such as inertial range transfer (Sorriso-Valvo et al., 2019), electromagnetic work (Wan et al., 2012), electron energization (Karimabadi et al., 2013), and pressure-strain interactions (Yang et al., 2017) concentrate in small sub-volumes of plasma turbulence. Dynamical processes that lead to dissipation such as magnetic reconnection, also occur in spatially localized regions (Drake et al., 2008). Along with these we now have observed strong indication that velocity-space driven phenomena (Servidio et al., 2012; Greco et al., 2012; Schekochihin et al., 2016; Servidio et al., 2015) also occur in similar highly localized

sub-volumes. Observation and study of wave signatures which propagate in both directions and thus implying proximity to the generation region may provide a more conclusive evidence. The nature of the spatial or regional correlations of these kinetic processes to the surrounding dynamical processes that drive them largely remains to be explored.



# Chapter 6

## TEMPERATURE ENHANCEMENT ALONG INTERMITTENT STRUCTURES

### 6.1 Overview

The solar wind proton temperature at 1 au has been found to be correlated with small-scale intermittent magnetic structures, i.e., regions with enhanced temperature are associated with coherent structures such as current sheets. Using Parker Solar Probe data from the first encounter, we study this association using measurements of radial proton temperature, employing the Partial Variance of Increments (PVI) technique to identify intermittent magnetic structures. We observe that the probability density functions of high-PVI events have higher median temperatures than those with lower PVI. The regions in space where PVI peaks were also locations that had enhanced temperatures when compared with similar regions suggesting a heating mechanism in the young solar wind that is associated with intermittency developed by a nonlinear turbulent cascade in the immediate vicinity. We also look into magnetosheath ion temperature using MMS and report on the findings.<sup>1</sup>

### 6.2 Introduction

As discussed in Section 1.3, solar wind is a stream of charged and highly magnetized plasma streaming at supersonic speed originating from the Sun. Solar wind is primarily composed of ionized hydrogen (Marsch et al., 1982; Kasper et al., 2012) with varying amount of helium nucleus (Maruca, 2012b) and minor heavier ions.

Despite decades of observation, the exact process that originally heats and accelerates solar wind plasma remain unknown, but several candidates have been proposed.

---

<sup>1</sup> Part of this study was published in Qudsi et al. (2020b).

Turbulence cascade transfers energy from large to small scales (see Section 3.2 for more details), which can ultimately lead to dissipation and heating (Velli et al., 1989; Velli, 1993; Matthaeus et al., 1999; Dmitruk et al., 2002; Cranmer & van Ballegooijen, 2005; Cranmer et al., 2007; Cranmer & van Ballegooijen, 2012; Cranmer, 2014; Verdini & Velli, 2007; Verdini et al., 2009a,b; Chandran & Hollweg, 2009; Perez & Chandran, 2013; Lionello et al., 2014). Current sheets, generated by cascading vortices, can also lead to localized heating (Parashar et al., 2009; Osman et al., 2011, 2012a,b; Gingell et al., 2015). Wave particle interactions — including, e.g., microinstabilities, Landau damping, and ion-cyclotron resonance — can likewise result in significant changes to the particles' phase-space distribution (Gary, 1993; Sahraoui et al., 2010; Klein & Howes, 2015). Though there are several linear and non-linear mechanisms which heats the space plasma, here we focused on one such mechanism, coherent structures: features in the plasma that are persistent through time, concentrated in space, or both (Greco et al., 2018). As discussed in Section 3.2.3 such structures can be produced by turbulent cascade (Osman et al., 2012b) and are also associated with current sheets (Yordanova et al., 2016). Osman et al. (2011, 2012b) analyzed in-situ observations and of near-Earth solar wind and found clear indications that coherent structures correlate with local enhancements in temperature.

So far most of the studies have been done using either numerical simulation data or solar wind data at 1 au. However, plasma conditions are a lot different at 1 au from those very close to the Sun, say 0.2 au. Magnetic field near 0.2 au is  $\sim 70$  nT compared to  $\sim 5$  nT at 1 au. Plasma at 0.2 au is also much denser and hotter ( $\sim 200$  /cm $^{-3}$  and  $\sim 10^6$  K compared to  $\sim 5$  /cm $^{-3}$  and  $\sim 10^4$  K respectively) (Kasper et al., 2019). And even though solar wind is mostly collisionless, plasma at 1 au has gone through more processing compared to the young solar wind (Verscharen et al., 2019, §3.3 & references therein). The recently launched Parker Solar Probe (PSP) provides an unprecedented opportunity to study the nascent solar wind in great detail.

In this study, we revisit the techniques of Osman et al. (2011, 2012b), and, by applying them to observations from Parker Solar Probe (PSP), explore the relationship

between plasma structures and heating in nascent solar wind plasma. We also look into the heating of terrestrial magnetosheath plasma using data from MMS. Section 6.3 provides the background on such structures and introduces the reader to the physics of technique employed in data analysis which is described in Section 6.4. In Section 6.5 we present the results and discuss its implication. Section 6.6 summarizes the results along with a conclusion and potential future works.

### 6.3 Background

Some recent studies, both observational and numerical, have shown that intermittent structures are correlated with the regions of enhanced temperature in the plasma (Osman et al., 2012a, 2011; Greco et al., 2012) and understanding the mechanisms by which the turbulence heats the plasma may also help solve the coronal heating problem (Osman et al., 2012b). This is a particularly attractive scenario especially given the ubiquity of the localized structures. Study performed on data from PIC simulation by Wu et al. (2013) shows that the correlation between enhanced temperature and coherent structures exists for sub ion inertial length ( $d_i$ ). Further evidence of this is provided by TenBarge & Howes (2013) for Gyrokinetic simulation, Parashar et al. (2009); Wan et al. (2012); Karimabadi et al. (2013); Wan et al. (2015) for PIC and S. Servidio & Veltre (2012); Servidio et al. (2015) for Vlasov simulations respectively. Work done by Chasapis et al. (2015) and Yordanova et al. (2016) on from Cluster and MMS data show similar results from observation vantage point.

In this study, we investigate these discontinuities in the magnetic field and explore their association with local enhancements in ion temperature. As discussed in Section 3.2.3 we use PVI (see Equation (3.9) for the expression of PVI) to identify the discontinuities. Although these structures constitute only a small fraction of total data set their contribution to the total internal energy per unit volume is high. This emphasizes the importance of using the PVI technique for such studies. We also note that an analogous examination of the association of PVI events with energetic particles was carried out at 1 au, (Tessein et al., 2016).

## 6.4 Data Selection and Methodology

We analyzed data from PSP’s first encounter with the Sun (October 31 to November 11, 2018). The FIELDS fluxgate magnetometers provided measurements of the local magnetic field at a rate of 64 samples/NYseconds. Radial proton temperature/thermal speed data was obtained from the Solar Probe Cup (SPC), part of the Solar Wind Electron, Alpha and Proton suite (Kasper et al., 2016) (See Section 4.1.3 for a more detailed discussion of PSP, SPC, FIELDS and the dataset used in this study). The average speed of solar wind during the first encounter was around 350 km/s for the most part and crossed 500 km/s only on the last day of the encounter. Thus, using Taylor’s Hypothesis, 1 NYs corresponds to a length scale of 300 km.

For the calculation of PVI according to Equation (3.9), we used 64 NYHz data, with a lag of 1 NYs, which is the native cadence of SPC (Kasper et al., 2016). The ensemble averaging was done over 8 hours, which is several times the estimated correlation time. In this study we used the correlation time computed in Parashar et al. (2020). However there are few subtleties associated with this calculation, and Smith et al. (2001); Isaacs et al. (2015); Krishna Jagarlamudi et al. (2019); Bandyopadhyay et al. (2020a) offer more insights and discussion on this topic along with potential issues in such determination. We also carried out the analysis for various different averaging times (from 1 to 12 hours) and different lags (from 1 to 100 seconds) and it was observed to have minimal affect on the outcome. Figure 6.1 plots the relative changes in PVI for 6<sup>th</sup> of November, 2018 for these different inputs, and shows that the value of computed PVI barely changes for different lags and averaging times, thereby reaffirming the robustness of this method. Though changing the lag or averaging times or both slightly changes the overall value of PVI, they remain highly correlated with respect to each other over the entire interval. PVI time series was then resampled to ion cadence of 1 NYHz in the way such that for each interval of 1 NYs, the maximum value of PVI in that interval was chosen.

In this study we focused on the second half of the encounter, immediately after PSP was at its perihelion. The second half of the encounter has very different properties

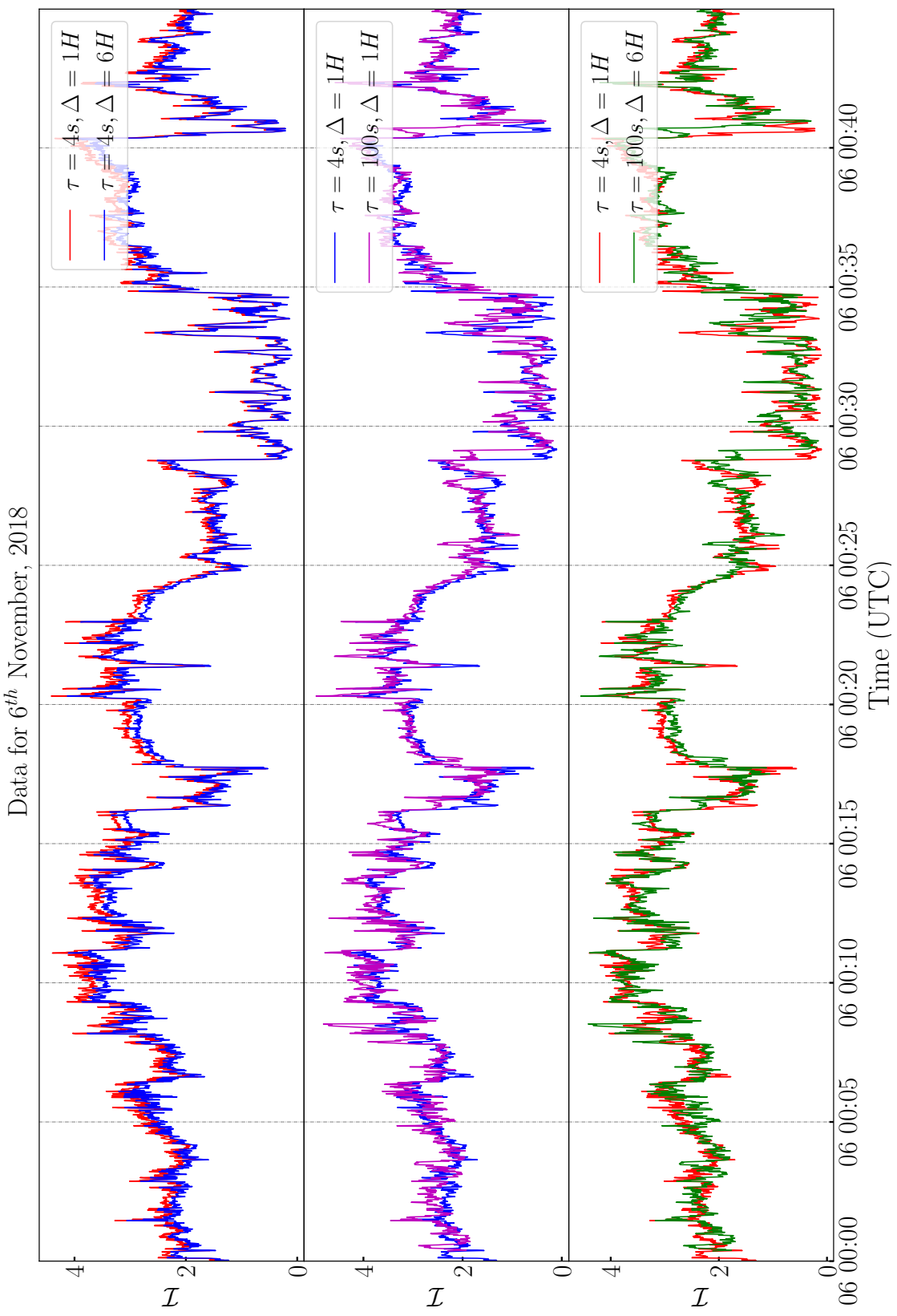


Figure 6.1: Comparison of PVI computed for PSP for various different set of lag and averaging time. Though changing the lag or averaging times or both slightly changes the overall value of PVI, they remain highly correlated with respect to each other over time.

compared to the first half. A greater number of energetic particles were observed (McComas et al., 2019), the solar wind speed was comparatively higher (Kasper et al., 2019), and there were many more switchbacks or polarity reversal of magnetic fields (Bale et al., 2019). Bandyopadhyay et al. (2020a) observed enhanced local energy transfer, which points towards a more turbulent period in general, and thus a suitable environment for PVI study.

For MMS analysis, we used the same data set as reported in Sections 4.1.2 and 5.3.2.

## 6.5 Results

Figure 6.2 shows the joint histogram of radial proton-temperature and PVI for the first encounter of PSP. Increasing PVI color contours have an upwards trend, as we see temperature distribution showing a positive slope with increase in value of PVI. The positive correlation between temperature and PVI suggest some kind of heating in the regions with high PVI. We then conditionally sampled radial proton temperature. Conditionally sampled means that we arrange the data by increasing value of PVI and then divide all the data points in 6 bins such that each bin has equal number of points. We then calculate the temperature distribution within each bin which is shown in Figure 6.3.

As PVI increases, the probability density increases for the higher temperature and decreases for the lower temperature which is opposite of what we see at the low temperatures where probability density is highest for the lowest PVI. Median temperature, shown by vertical lines in Figure 6.3, for each of the distribution increases implying presence of stronger and stronger heating as we go to higher and more extreme values of PVI. For  $\text{PVI} < 1$ , median value of the temperature is  $5.32 \times 10^5 \text{ K}$  whereas for  $\text{PVI} > 6$ , the median temperature increases to  $1.01 \times 10^6 \text{ K}$ . Osman et al. (2011) observed similar increase in average temperature in their study of solar wind at 1 au. This is consistent with heating occurring in the regions with small scale coherent structure in MHD turbulence.

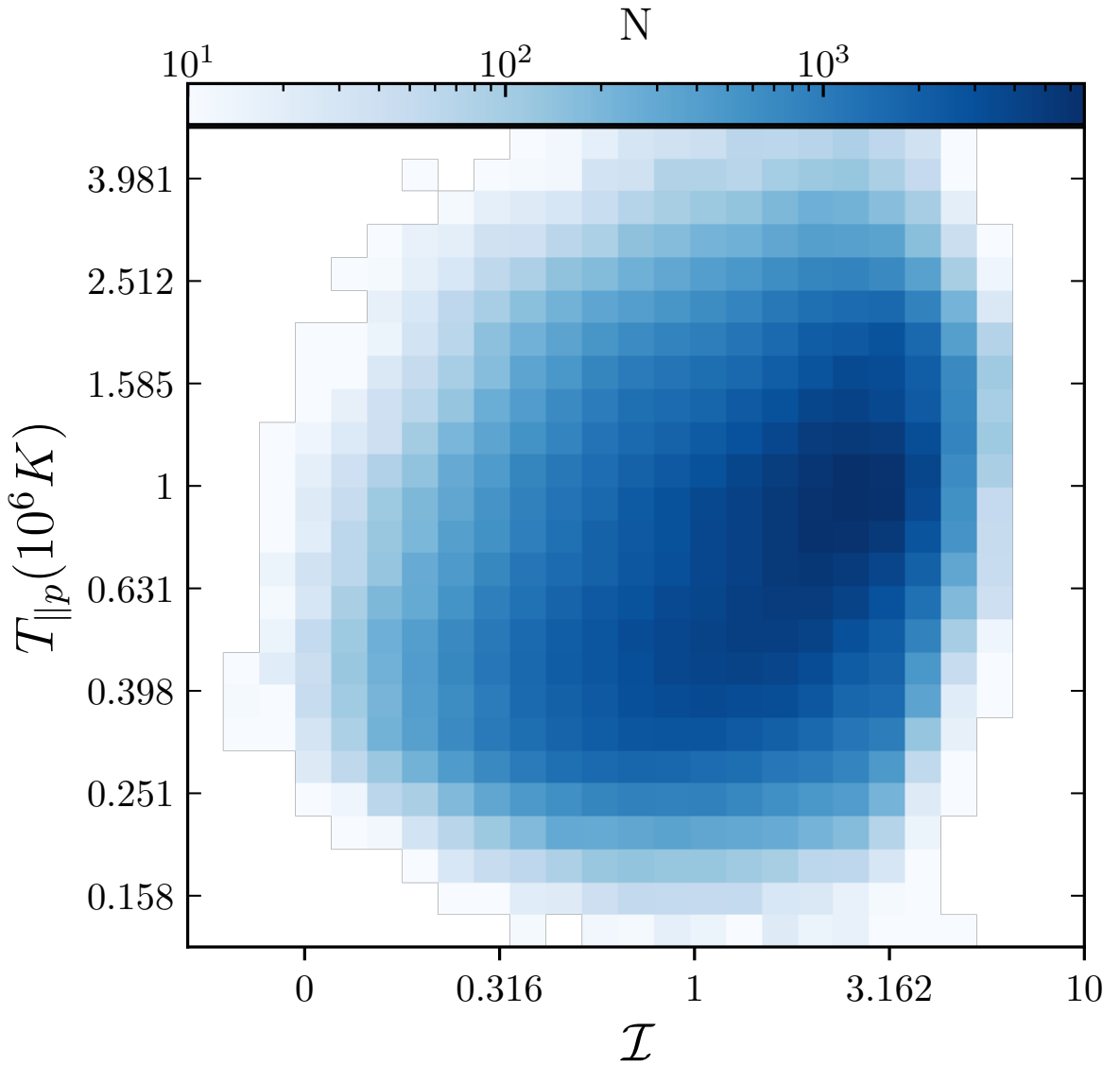


Figure 6.2: Joint histogram of radial proton-temperature and PVI for the second half of first encounter on a log-log scale. There is an upward trend between PVI and temperature as the deep blue region in the plot tilts upwards showing an increase of temperature as PVI increases. *Figure reproduced from Qudsi et al. (2020b) with the permission of AIP Publishing* (see Appendix D).

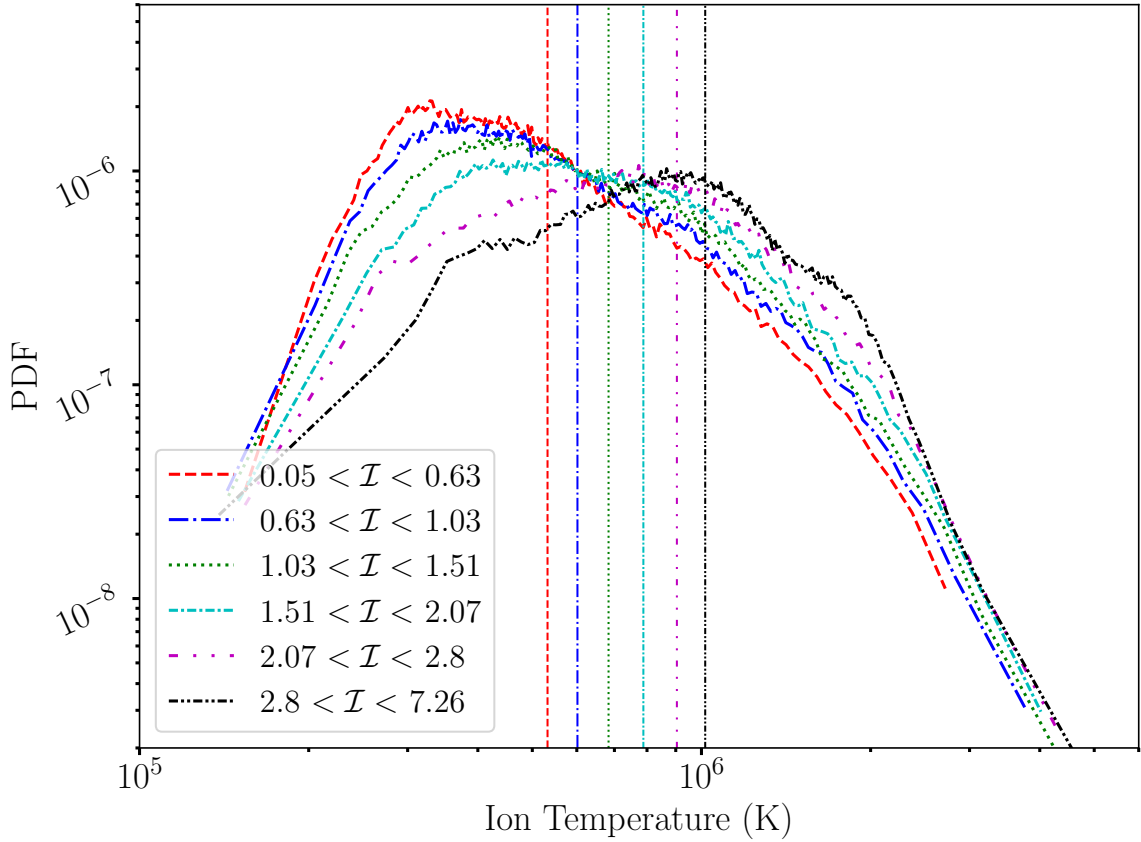


Figure 6.3: PDFs for the radial proton-temperature for the second half of first encounter. Each PDF corresponds to a different PVI range such that each PVI bin has equal number of data points. The probability density increases with increase in temperature for high PVI events and peaks at comparatively higher value of temperature, whereas it decreases for low PVI PDF. Vertical lines show the median temperature for each of the PDF plot. *Figure reproduced from Qudsi et al. (2020b) with the permission of AIP Publishing* (see Appendix D).

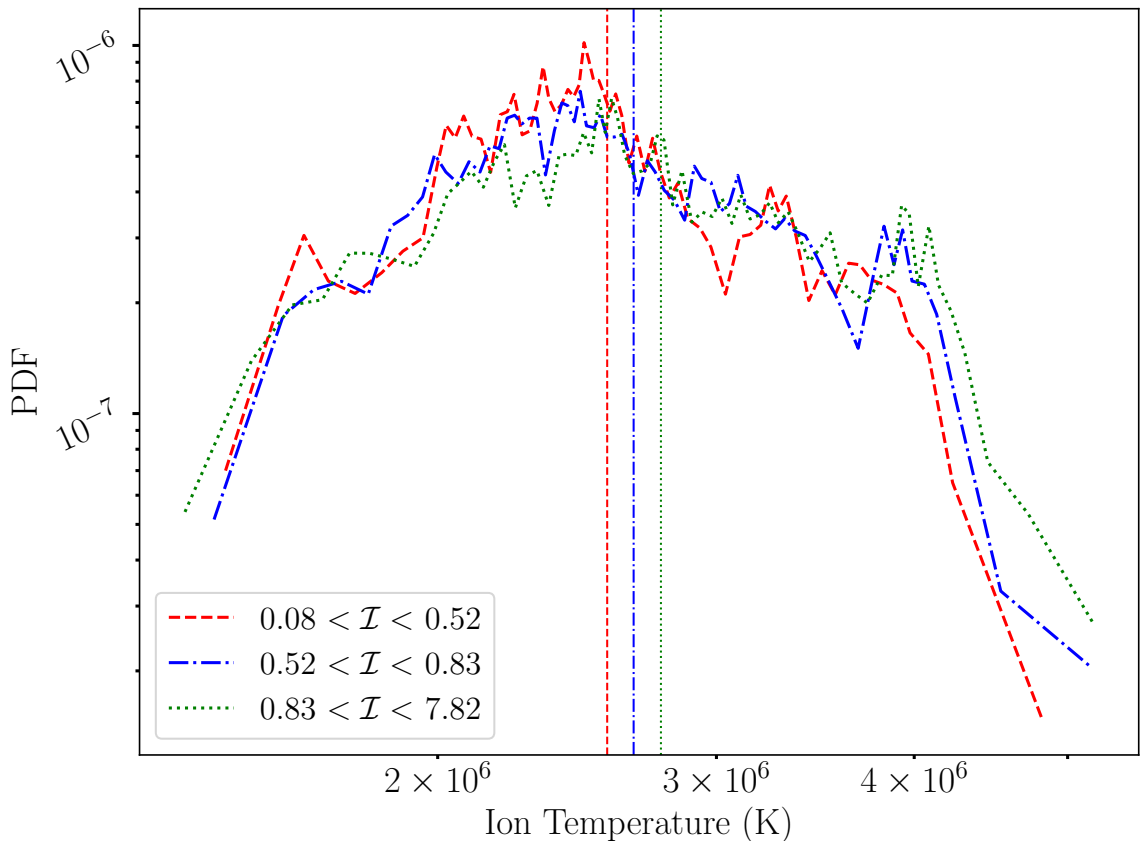


Figure 6.4: PDFs for the total proton-temperature for 40 minutes burst observation from MMS. Each PDF corresponds to a different PVI range such that each PVI bin has equal number of data points. The probability density increases with increase in temperature for high PVI whereas it decreases for low PVI PDF. Vertical lines show the median temperature for each of the PDF plot.

Though distribution of total proton temperature from magnetosheath shows similar trend in the median temperature of each bin as seen in Figure 6.3, the enhancement in temperature is comparatively smaller. The median temperature corresponding to three bins shown in Figure 6.3 are  $2.56 \times 10^6$  K,  $2.66 \times 10^6$  K and  $2.77 \times 10^6$  K, which is barely an increment. However, this is reflective of two features of magnetosheath temperature and PVI compared to that of nascent solar wind. The radial temperature of solar wind varies over more than an order of magnitude whereas for magnetosheath it is less than half an order. Also, comparatively, solar wind has much higher values of PVI than that of magnetosheath, mean value of 1.69 versus 0.78. There are other factors to be considered as well. Short interval of observation which results in smaller amount of data could be another contributing factor. Also, in the case that fluctuation event lasts longer than the interval length, we won't detect any enhancement in the observed temperature. Though we did not see a conclusive evidence of temperature enhancement for ions, it is worth noting that Chasapis et al. (2018) did observe it for electrons. A comparative statistical study of PVI for datasets of different length of observation time will help in quantifying how prominent is the effect of duration of observations on the value of computed PVI.

In order to further demonstrate the relationship between PVI and enhanced temperature for PSP, we looked at the temperature at the point of high PVI event and its immediate surrounding in space using the methodology described by Osman et al. (2012b). We compute the mean value of temperature at the point of the PVI event and for points near the PVI events separated from it by up to one correlation length. Formally, these averages may be expressed as:

$$\tilde{T}_p(\delta t, \theta_1, \theta_2) = \langle T_p(t_{\mathcal{I}} + \delta t) | \theta_1 \leq \mathcal{I}(t_{\mathcal{I}}) < \theta_2 \rangle \quad (6.1)$$

where  $\tilde{T}_p$  is the conditionally averaged temperature for all the events,  $\delta t$  is the time difference relative to the position of PVI events,  $t_{\mathcal{I}}$  is the time of PVI events between the threshold  $\theta_1$  and  $\theta_2$ . In Equation (6.1), for a given threshold of PVI, we record the temperature at each point where PVI satisfies the expression  $\theta_1 \leq \mathcal{I}(t_{\mathcal{I}}) < \theta_2$ .

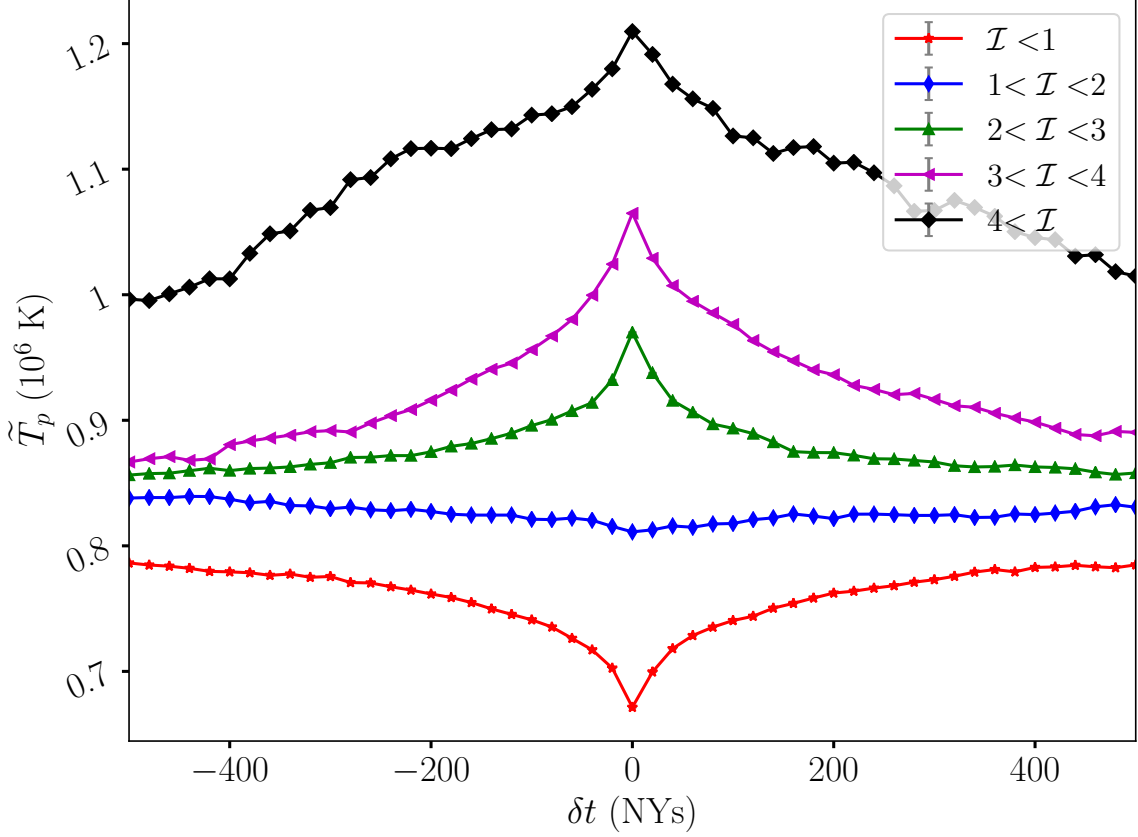


Figure 6.5: Figure shows conditional average temperature for different PVI thresholds at the point of a PVI event.  $\tilde{T}_p$  peaks at the instant of PVI event and continues to have elevated temperature in its vicinity within the correlation time scale. Red curve, corresponding to lowest PVI shows a dip suggesting no heating when the magnetic field is very smooth. The error bars are smaller than the symbols and thus not easily visible in the figure. *Figure reproduced from Qudsi et al. (2020b) with the permission of AIP Publishing* (see Appendix D).

We then record the temperature around that point, moving up to 1 correlation length away from the point of PVI event. Once we have the temperature at all such points, we take the average of all temperatures which were at same distance from the event.

Figure 6.5 shows the plot of  $\tilde{T}_p$  for various thresholds for the second half of the encounter. Not only do we observe enhanced temperature at the point of high PVI events, suggesting localized heating at those points, we also see that  $\tilde{T}_p$  for a higher PVI event is consistently higher than nearby points separated by up to a correlation length. This implies that the points nearby an identified PVI event have an elevated

average temperature, continuously approaching the elevated average temperature found at the PVI event itself. Some of this effect may be due to clustering of PVI events (see Chhiber et al. (2020)). Another point worth noting in Figure 6.5 is the valley in the temperature profile for small PVI. This is the region where background magnetic field is smooth and it appears that in such regions, the temperature is lower than the temperature of plasma in its immediate surrounding, which is concurrent with the fact that in those places there is no turbulence heating. Osman et al. (2012b) found similar result in their study at 1 au. However, in our study we find a significant dip compared to the dip reported in Osman et al. (2012b),  $\sim 10^5$  K compared to  $\sim 2 \times 10^3$  K.

## 6.6 Discussions

In this study, we used in-situ observations from PSP's first encounter with the Sun and the magnetosheath data from MMS to explore the association of proton heating with coherent magnetic structures in space plasmas. We identified enhancements of PVI (Greco et al., 2008) as indicative of the presence of such a structure (Osman et al., 2011, 2012b). We observed that the joint histogram of PVI and proton radial temperature, for solar wind, shows positive trend as shown in Figure 6.2. We also observed that the PDF of data, as shown in Figures 6.3 and 6.4, with higher PVI has higher median temperature compared to those with lower PVI for both solar wind and terrestrial magnetosheath. These observations strongly supports the theory that the solar wind in those regions are heated by coherent structures which are generated by plasma turbulence. Though owing to certain characteristics of magnetosheath data, a more in-depth analysis is required to draw any final conclusion.

The present results demonstrate both the shifting of the PDF of temperature towards higher values with increasing PVI condition, (in Figure 6.3) and the spatial/temporal localization of the temperature enhancement near PVI events (in Figure 6.5). Both of these are fully consistent with findings in the two papers that examine these effects (Osman et al. (2011, 2012a), respectively). It is interesting that these effects are present clearly in the PSP first orbit where turbulence is presumably younger

and possibly less well developed than it is at 1 au. It is possible that the temperature differential between low and high PVI is somewhat less in the PSP data than in the ACE data at 1 au ([Osman et al., 2011](#)), but additional samples by PSP will be needed to draw any firm conclusion of this type.

In order to further demonstrate this association we looked at the conditionally average temperatures at the point of a high PVI event and in its immediate surrounding up to 1 correlation length. We observed that not only the point of event has the highest temperature, its vicinity shows enhanced temperature compared to lower PVI events. The local maxima of these temperature profiles are most prominent for higher PVI events suggesting stronger heating. The plateau region of each thresholds are distinct, and for higher threshold they maintain a high value suggesting clustering of PVI events around a large discontinuity. For very smooth magnetic field we see a dip in the average temperature at that point. [Osman et al. \(2012b\)](#) found similar behavior in their study of solar wind at 1 au, though neither the heating nor the dip in temperature for small PVI that they reported in their study was as high as what we observed in our study. This suggests that either coherent structures are more efficient in heating the plasma near the Sun compared to 1 au or we have a lot more such structures as we move closer to the Sun. Since these coherent structures are generated by plasma turbulence, these observations suggest that non-linear turbulence cascade play a crucial role in heating the nascent solar wind. Given the ubiquitous nature of such structures, this process can help explain the coronal heating or be at least a part of the explanation.

A significant limitation of this study was unavailability of temperature-anisotropy data. The temperature measures we used were not the scalar temperature but rather the radial temperature, for which reason we limited our observations to period of nearly-radial magnetic field (see Sections [4.1.3](#) and [6.4](#)). Once reliable ion temperature-anisotropy data are available, the present study could be revisited to explore both scalar and anisotropic heating. Theoretical studies have found that turbulent cascade can generate strong temperature anisotropy near coherent structures ([Parashar & Matthaeus, 2016](#)).

A careful inspection of Figure 6.5 reveals a very slight asymmetry in the shape of the temperature profile right before and after the PVI event. The phenomenon was also noted in 1 au solar wind by ([Osman et al., 2012b](#)). The cause and significance of this asymmetry remain unclear, but it may suggest a connection between local heating and large-scale processes such as heat flux.

## Chapter 7

# INTERPLAY BETWEEN LINEAR AND NON-LINEAR PROCESSES

### 7.1 Overview

In the last two chapters, Chapter 4 and Chapter 5, we discussed two different processes which result in heating or temperature enhancements in the space plasmas. As we found in Chapter 5 two processes occur simultaneously in both space and time and are entangled together at different scales. Consequently, there is an implied competition between the two processes to determine which one dominates given a set of conditions in the space plasmas. In this chapter we look at the two processes simultaneously to see the result of this competition as well as the dynamics between the two. We compare the time scales of two processes to see which one dominates and report our results in this chapter.<sup>1</sup>

### 7.2 Introduction

Solar wind is weakly collisional. The VDFs of solar wind ions exhibit non-Maxwellian features which introduce significant free energy in the system (see Chapter 2). The presence of additional features like secondary beam population<sup>2</sup> (Verscharen et al., 2019, and references therein) signifies additional departure from the local thermodynamic equilibrium and thus provide one form of free energy. All this often results in significant departure from temperature isotropy ( $T_{\perp} = T_{\parallel}$ ), which leads to the development of kinetic microinstabilities fueled by the free energy in the system. As

---

<sup>1</sup> Part of this study was published in Bandyopadhyay et al. (2020b) and Gary et al. (2020).

<sup>2</sup> A field aligned secondary population of species which moves at a higher speed compared to the core population along the magnetic field lines.

discussed in Chapters 2 and 5, these instabilities then act to make the system more isotropic by scattering of particles in phase space.

Turbulence is another process by which the opposite affect can be achieved, enhancement in anisotropy of the plasma, and because of its ubiquitous nature, it is expected to play important role in the dynamics of the plasmas. Thus at any point these two processes are either feeding off of each other or are competing in the system. Recent studies have shown that coherent structures (e.g., current sheets) generated by solar wind turbulence can generate extreme anisotropies (Greco et al., 2012; Servidio et al., 2015; Karimabadi et al., 2013) which results in development of linear growth rates as predicted by the Vlasov dispersion equation (Qudsi et al., 2020a). Other studies (Karimabadi et al., 2013; Matthaeus et al., 2015) have shown that local instabilities may arise occasionally in the presence of shear driven turbulence. Bale et al. (2009) found enhancements in magnetic fluctuations in regions of solar wind plasma that are susceptible to the development of one or more microinstabilities. Osman et al. (2013) showed the presence of high cascade rate in the same regions, suggesting that these two, linear and non-linear, processes exist in the same space.

However, since these two processes compete with each another to influence the plasma, it remain unclear as of now which one dominates and drive the large scale phenomenon. We thus decided to study the time scales at which the two processes work and compare them in different types of plasmas. For kinetic microinstabilities we study the linear growth rates (see Section 2.2.2) whereas for time scales associated with turbulence we look at the non-linear frequency and time scales as computed in Section 3.3. We carry out this analysis for six different datasets: 3 from simulation and 3 from in-situ measurement of space plasmas (see Chapter 4 and Table 4.2 for details of data and some other relevant quantities).

### 7.3 Data Selection and Methodology

Since we are to compare the two time scales, we look at the linear and non-linear rates present in the plasma locally. For the linear growth rates, we consider all the four

growth rates<sup>3</sup> which might be active at any point and compute the maximum of the 4 rates, where each growth rate was computed by the method described in Sections 2.2.3 and 4.2. Equation (7.1) puts this succinctly in the form of an equation.

$$\Gamma_{\max} = \max(\gamma_{\max, \text{cyclotron}}, \gamma_{\max, \text{mirror}}, \gamma_{\max, \parallel \text{firehose}}, \gamma_{\max, \# \text{firehose}}) \quad (7.1)$$

For the non-linear rate, we computed the local non-linear frequency ( $\omega_{\text{nl}}$ ) at any position  $\mathbf{r}$  for a lag length scale of  $\ell$  as :

$$\omega_{\text{nl}} \sim \delta b_\ell / \ell \quad (7.2)$$

Where  $\delta b_\ell$  is the change in the longitudinal magnetic field and is given by :

$$\delta b_\ell = \left| \hat{\boldsymbol{\ell}} \cdot [\mathbf{b}(\mathbf{r} + \boldsymbol{\ell}) - \mathbf{b}(\mathbf{r})] \right|, \quad (7.3)$$

Where  $\mathbf{b}$  is the total magnetic field expresses in local Alfvén speed units (see Section 3.3). As mentioned in Section 4.2.3 for all cases except the 3-D dataset, since the goal was to carefully evaluate the nonlinear frequency at the scale of the fastest growing mode, the value of  $\ell$  is given by  $1/k_{\max}$ , where  $k_{\max}$  is the wave number corresponding to  $\Gamma_{\max}$  as computed in Equation (7.1). Since for marginally unstable plasma,  $k_{\max}$  is typically of the same order as the ion inertial length ( $d_i$ ) (Maruca, 2012a, Figures 6.6 to 6.9), for the case of 3-D simulation, because of some computation limitation, we set  $\ell = d_i$ .

## 7.4 Results

Figure 7.1 shows the comparison between the two time scales (linear and non-linear) for three different simulations (see Chapter 4 for more detail). The first panel of each row shows the maximum value of linear growth rates ( $\Gamma_{\max}$ ) as defined by Equation (7.1). The second panel shows the non-linear growth rates ( $\omega_{\text{nl}}$ ) computed using Equation (7.2). Though  $\omega_{\text{nl}}$  is largely uniform over the simulation box, heightened

---

<sup>3</sup> Under the assumption of no secondary beam populations and an isotropic electron population.

values of it lie close to the regions with high current density and/or where temperature anisotropy has extreme values (see Figures 5.1 to 5.3). The third panel shows the ratio between the two growth rates. This ratio is only computed for regions where the condition  $\Gamma_{\max} > 10^{-5}\Omega_{cp}$  is satisfied, consequently there are very few points of comparison compared to the total number of points inside the box (see Table 7.1). The third panel shows that there are very few points where  $\Gamma_{\max} > \omega_{nl}$ , which implies the dominance of non-linear phenomena over the linear one for all three different kinds of simulation conditions. This means that it takes longer time for the linear instability to affect the system than the eddy turnover time and thus it will be the nonlinear processes and not linear instability which will dictate the evolution of the system. Counting the number of data points where both the conditions ( $\Gamma_{\max} > 0$  and  $\Gamma_{\max}/\omega_{nl} > 1$ ) were satisfied, we found that the conditions were true only for 0.019, 0.053 and 0.59 percentages of cases for **149p6**, **kaw** and **ros** datasets respectively.

Figures 7.2 to 7.4 show the time series equivalent of Figure 7.1 for three different spacecraft (MMS, Wind and PSP respectively), located in different space plasmas: Earth's magnetosheath, 1 au solar wind, and near-Sun solar wind ( $\sim 0.2$  au) (see Section 1.3 and Chapter 4). Similar to Figure 7.1, for each of these figure the first panel shows the time series for  $\Gamma_{\max}$ , the second shows that for  $\omega_{nl}$ , and the third shows ratio of the two. The dashed red line in each third panel demarcates  $\Gamma_{\max} = \omega_{nl}$ . Though in all three sets of observations, fraction of data with  $\Gamma_{\max} > \omega_{nl}$  is higher than in the simulations (see Table 7.1), it remains well below 50%. Though Klein et al. (2018) used a different method to compute the condition of plasma instability and a different condition for calculation of  $\omega_{nl}$ , they found a similar result for solar wind at 1 au.

Figure 7.5 shows the kernel density estimate (KDE)<sup>4</sup> plot for each of the aforementioned six datasets generated using `seaborn` package in Python. As expected, in all the cases the core of KDE is below  $\Gamma_{\max} = \omega_{nl}$  line (dashed red line). Though for simulation dataset **149p6** the core of the distribution is centered between  $\Gamma_{\max} = 10^{-4}$

---

<sup>4</sup> KDE is a non-parametric method of probability density estimation of a random variable.

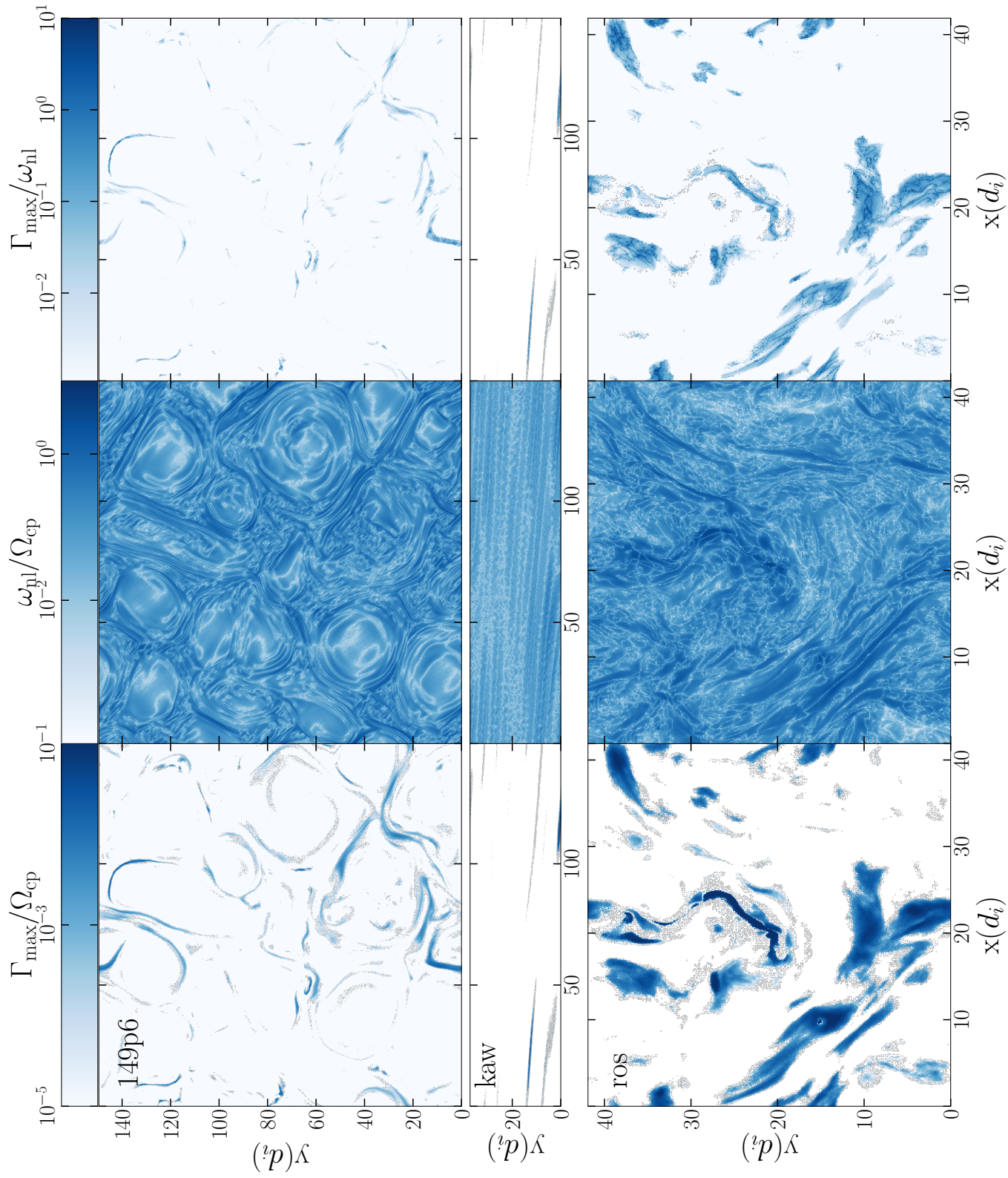


Figure 7.1: Plots (from left to right) of maximum linear growth rate ( $\Gamma_{\max}$ ), nonlinear frequency ( $\omega_{nl}$ ) and the ratio  $\Gamma_{\max}/\omega_{nl}$  for the three different kinds of PIC simulation. First row shows the data for 149p6 dataset, middle row is for kaw dataset and the bottom row shows the data from ros dataset.

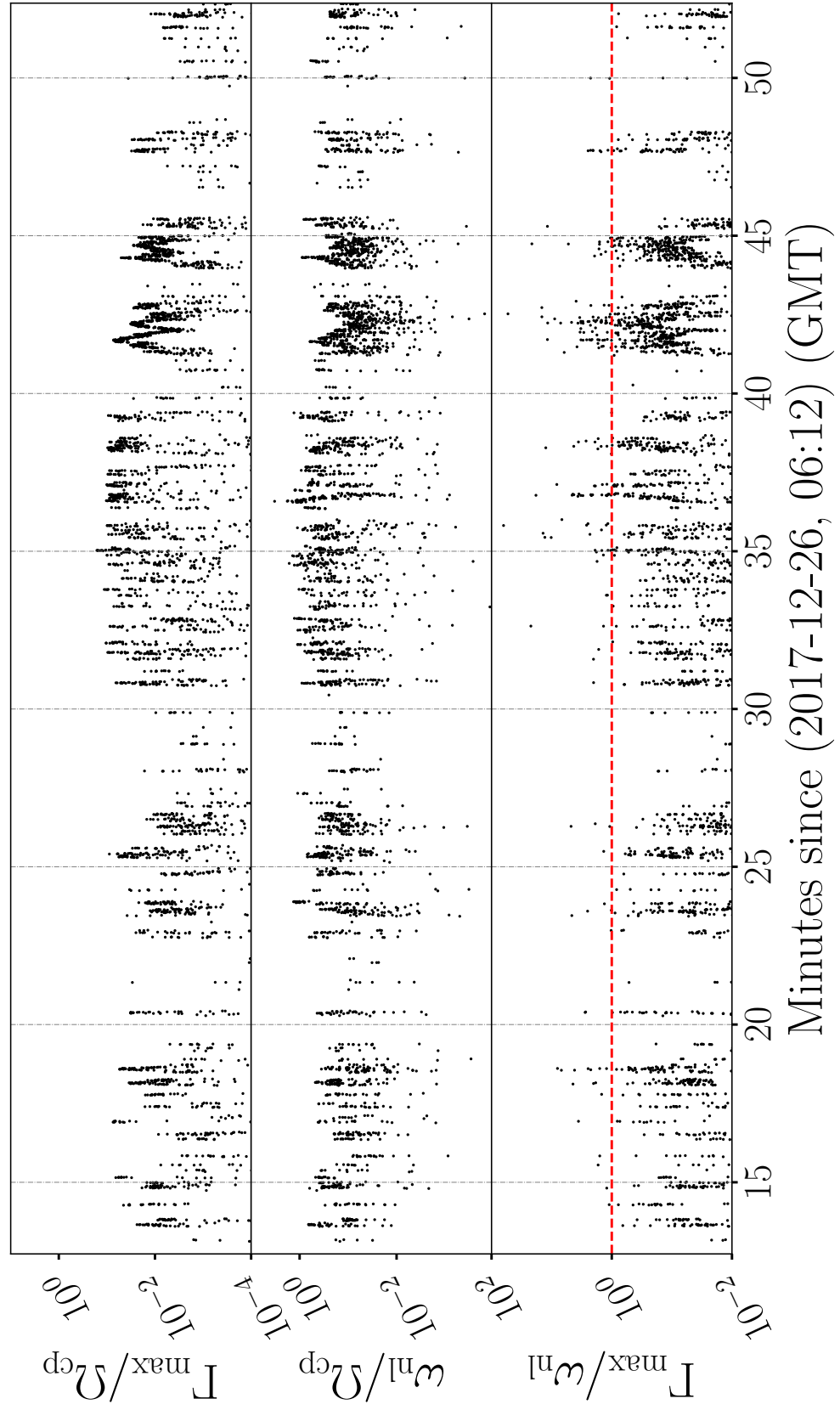


Figure 7.2: Time series plot of (top to bottom) of maximum linear growth rate ( $\Gamma_{\max}$ ), nonlinear frequency ( $\omega_{nl}$ ) at 1  $d_i$ , and the ratio  $\Gamma_{\max}/\omega_{nl}$  at  $z=0$ .  $d_i$  from terrestrial magnetosheath.

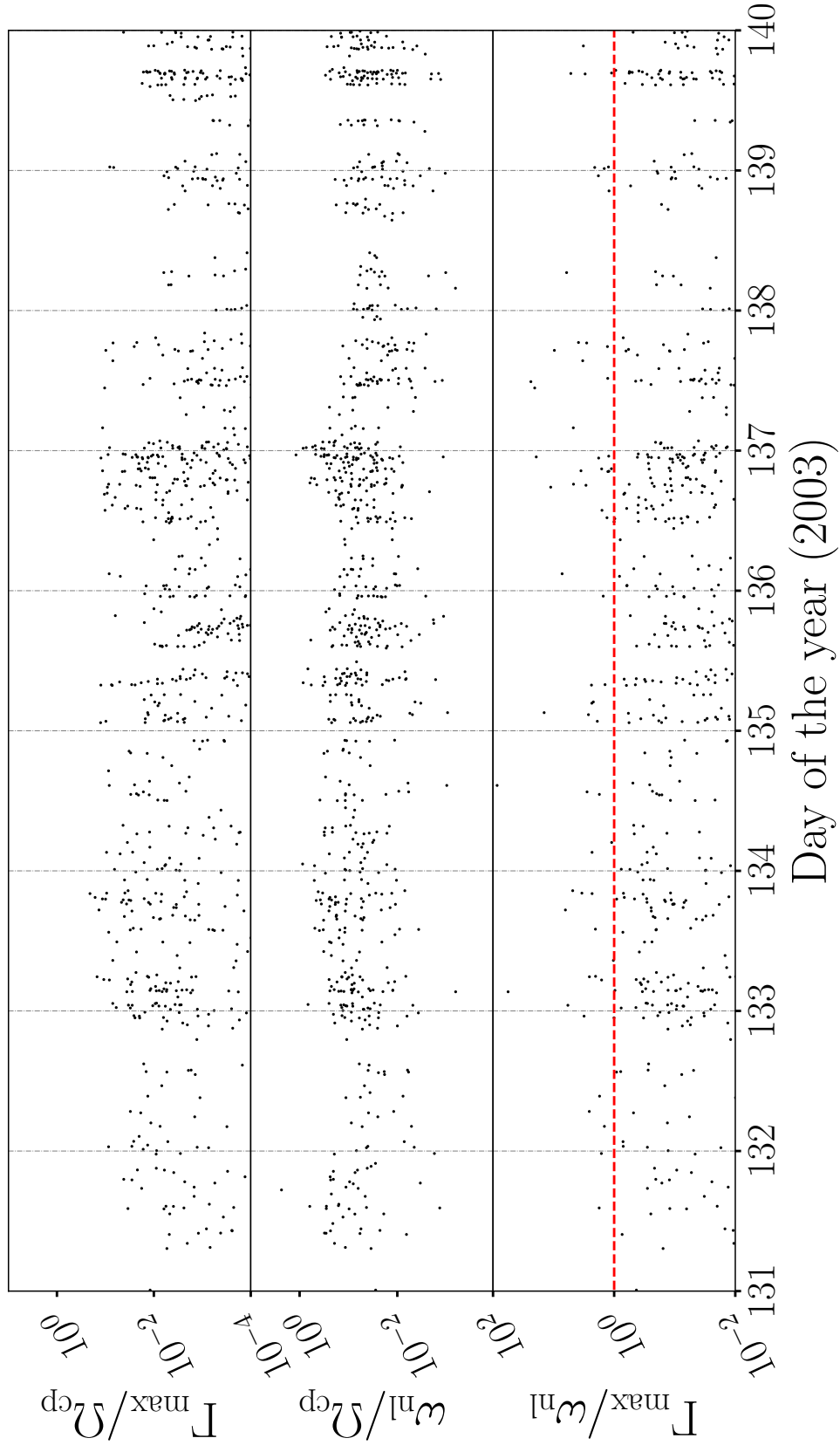


Figure 7.3: Time series plot of (top to bottom) of maximum linear growth rate ( $\Gamma_{\max}$ ), nonlinear frequency ( $\omega_{nl}$ ) at 1  $d_i$ , and the ratio  $\Gamma_{\max}/\omega_{nl}$  at  $z=0$ .  $d_i$  from solar wind at 1-a.u.

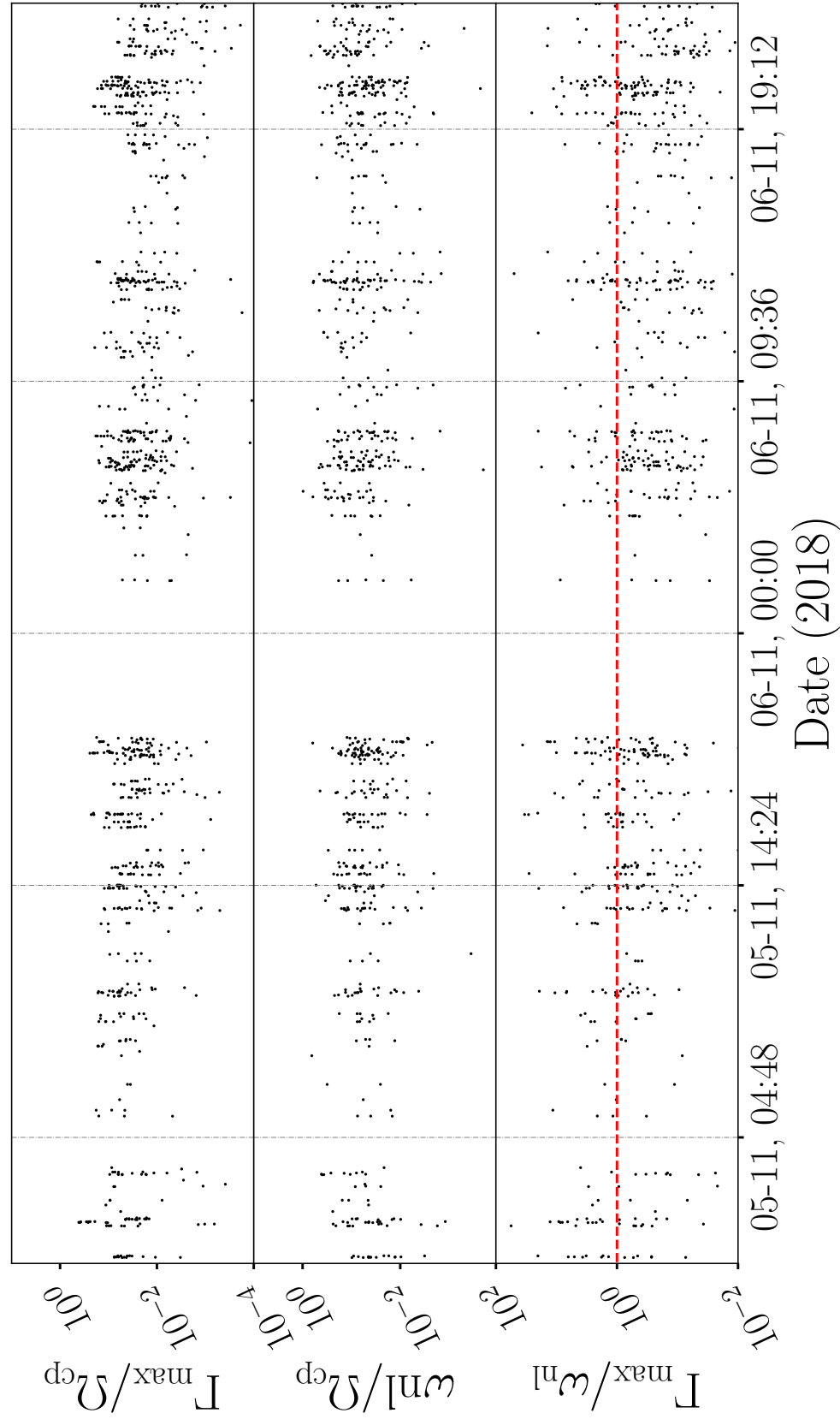


Figure 7.4: Time series plot of (top to bottom) of maximum linear growth rate ( $\Gamma_{\max}$ ), nonlinear frequency ( $\omega_{nl}$ ) at  $1 d_i$ , and the ratio  $\Gamma_{\max}/\omega_{nl}$  at  $z=0$ .  $d_i$  from solar wind close to the Sun.

Table 7.1: Number of points in each datasets, and where we have active linear instability present ( $\Gamma_{\max} > 10^{-5} \Omega_{cp}$ ) and where  $\Gamma_{\max}/\omega_{nl} > 1$  with associated percentages in parenthesis

Datasets	Number of		
	total data points	points where $\Gamma_{\max} > 10^{-5} \Omega_{cp}$ (%)	points where $\Gamma_{\max}/\omega_{nl} > 1$ (%)
149p6	16,777,216	1,144,615 (6.82)	3,347 (0.019)
kaw	4,194,304	37,560 (0.90)	2,227 (0.053)
ros	134,217,728	22,001,875 (16.39)	794,220 (0.59)
mms	15,857	3,887 (24.51)	174 (1.10)
wnd	1,316,621	187,338 (14.22)	2,7857 (2.11)
psp	95,034	5,347 (5.62)	1,483 (1.56)

and  $\Gamma_{\max} = 10^{-3}$ , for both **kaw** and **ros** datasets centroid of KDE is more than an order of magnitude higher at  $\Gamma_{\max} = 10^{-2}$ . This can be attributed to the fact that in both of these simulations the background magnetic field ( $\mathbf{B}_0$ ) in the plane of the fluctuations is non-zero, by design for the **kaw** dataset and for **ros** dataset because there are fluctuations in all 3 directions. This results in the case that  $\mathbf{k}_{\parallel} \neq 0$  for these two simulations, whereas for 149p6 simulation since there is no spatial variation in the direction parallel to  $\mathbf{B}_0$ , wave vector components parallel to  $\mathbf{B}_0$  are zero. This results in limited application of both Landau (fluctuations of zero frequency) and cyclotron resonance (fluctuations with  $n^{th}$  species cyclotron frequencies)([Gary et al., 2020](#)). This makes both the resonances independent of particle velocities and thus

the particles are constrained to fluid-like behavior. Because of this, 149p6 simulation fails to account for velocity dependent wave-particle interactions which may represent critical elements of turbulent dissipation at wavelengths of the order of or shorter than  $d_i$  (Gary et al., 2020). Another interesting feature of these KDE plots is how much closer to the  $\Gamma_{\max} = \omega_{nl}$  line the centroid of the distribution is for the PSP data compared to other spacecraft data, implying substantially more competition between the linear and non-linear processes closer to the Sun. Klein et al. (2021) observed similar enhancements in the linear growth rates for plasma closer to the Sun. Further analysis is needed, though, since the available PSP data were from such a short time interval (see Section 4.1.3), and temperature anisotropy was computed using an entirely novel technique (Huang et al., 2020). As was remarked in Section 6.6 close to the Sun the turbulence is quite young and not developed enough implying presence of weaker non-linear instabilities. Presence of faster linear growth rates closer to the Sun would also explain the stronger-than-expected plasma heating as evident in Figure 6.5. Another factor could also be the proximity of plasma to the Alfvén critical region and thus it exhibits wave like behaviour which are a lot stronger than those at 1 au or in the terrestrial magnetosheath.

Each of the datasets shows that non-linear time scales are in general faster than linear timescales. This would imply that in most cases linear processes never have enough time to act on the plasma in a way that is significant enough to affect the dynamics or the statistical behaviour of whole plasma. However, as discussed in Section 2.3 as well as in Section 5.5, linear theory is very efficient at predicting the boundaries of  $(R_p, \beta_{\parallel p})$  plots which implies that linear growth rates work well enough to regulate extreme values of  $R_p$  at high  $\beta_{\parallel p}$ . We thus look at the distribution of the two frequencies ( $\Gamma_{\max}$  and  $\omega_{nl}$ ) and their ratio for the three spacecraft datasets (**mms**, **wnd** and **psp**) on the  $(R_p, \beta_{\parallel p})$  plane.

Figures 7.6 to 7.8 show the distribution of data on a  $(R_p, \beta_{\parallel p})$ -plot. The first panel of each figure show the number of data points in each bin, the second panel shows the average value of  $\Gamma_{\max}$  in each bin,  $\omega_{nl}$  is shown in the third panel and their ratio

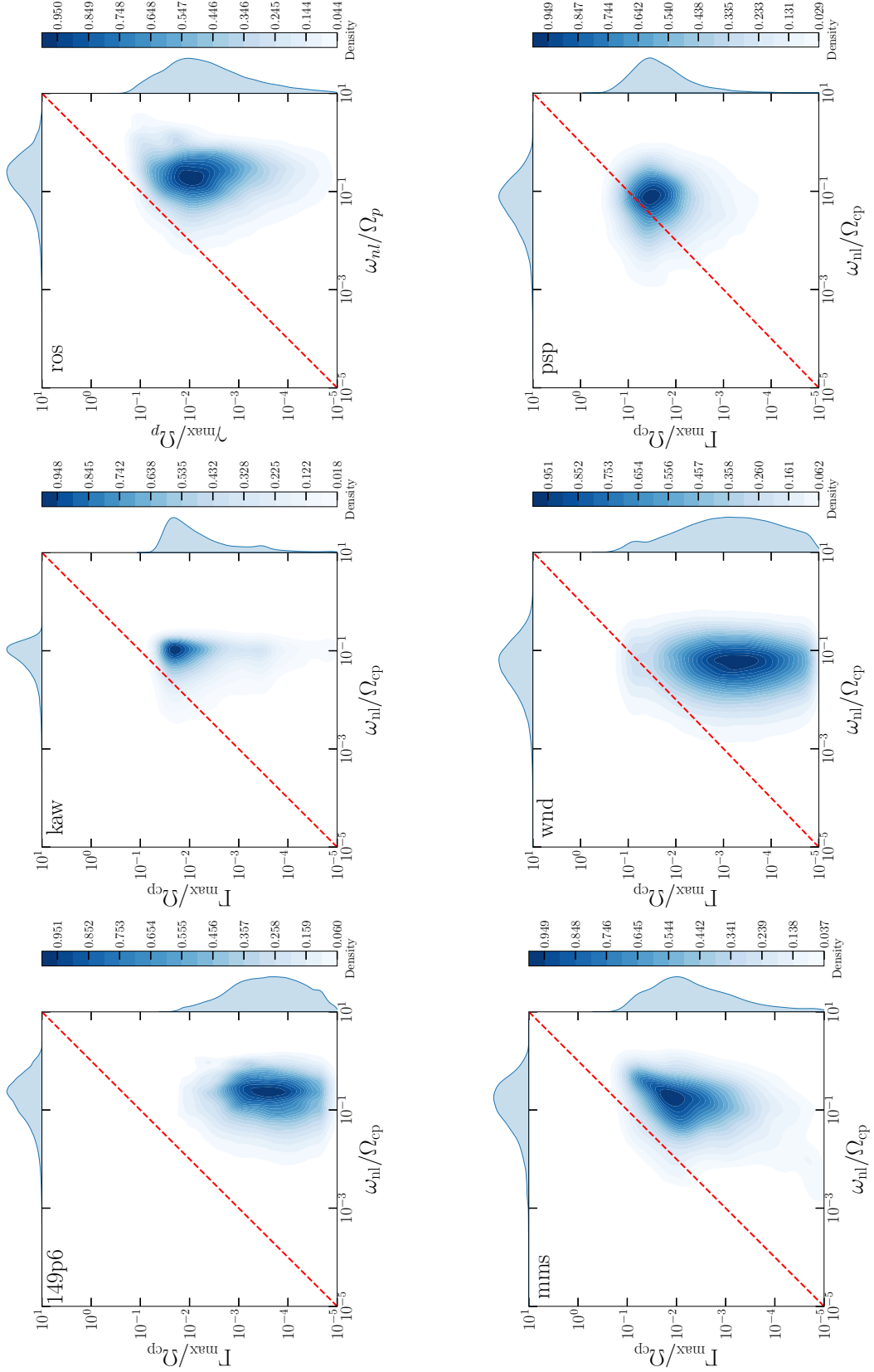


Figure 7.5: Kernel density plot for all six datasets used in this study. For all the cases the centroid of distribution is well below the  $\Gamma_{\max} = \omega_{nl}$  line, shown as dashed-red line, implying the dominance of non-linear processes over linear ones in all kind of plasmas.

in the fourth panel. As expected the region along the edges which is most susceptible to instability is where most of the instability is present. What is interesting to note is the distribution of  $\Gamma_{\max}/\omega_{nl}$  along the edges. For all the three spacecraft data, ratio of the two frequencies is increasing as we move outside from the centroid (as seen in the first panel) distribution. This is evident in all three cases, specially for the solar wind at 1 au (Figure 7.7) and near the Sun (Figure 7.8) it appears that linear time scales are a lot faster than their non-linear counterpart. Signifying that though in most cases  $\Gamma_{\max} < \omega_{nl}$ , it is greater than  $\omega_{nl}$  where it needs to be (along the periphery of  $(R_p, \beta_{\parallel p})$ -plots), and thus is quite efficient at limiting the exertion of plasma population to high anisotropy regions at high  $\beta_{\parallel p}$ .

## 7.5 Discussions

We investigated the competition between linear and non-linear time scales for 6 different datasets. We observed that non-linear processes arising because of turbulence dominate linear ones overwhelmingly (Figures 7.1 to 7.4). This would imply that the linear processes are of little consequence as far as dynamics and statistical properties of a turbulent plasmas is concerned. Yet, in-situ observations of space plasmas present strong evidence that linear microinstabilities regulate ion temperature anisotropy. Multiple studies of in-situ observations (Gary, 1991; Gary et al., 1994, 2001; Gary & Karimabadi, 2006; Kasper et al., 2002; Hellinger et al., 2006; Maruca et al., 2011, 2012; Maruca et al., 2018), have found that the distribution of plasma over the  $(R_p, \beta_{\parallel p})$  plane well restricted by thresholds predicted by linear Vlasov theory one must conclude that linear theory works. Observations made in Figures 7.6 to 7.8 provide further evidence. We observed that though  $\omega_{nl} > \Gamma_{\max}$  for most part, along the lines of threshold where microkinetic instabilities are most active, linear processes disrupt the turbulence cascade and dominate. However, as we saw in Figure 7.6 even when the two processes have comparable values along the edges, it still gave rise to expected  $(R_p, \beta_{\parallel p})$  plot (Maruca et al., 2018). Recent studies have shown that regions of extreme temperature anisotropy are produced because of generation of sharp gradients

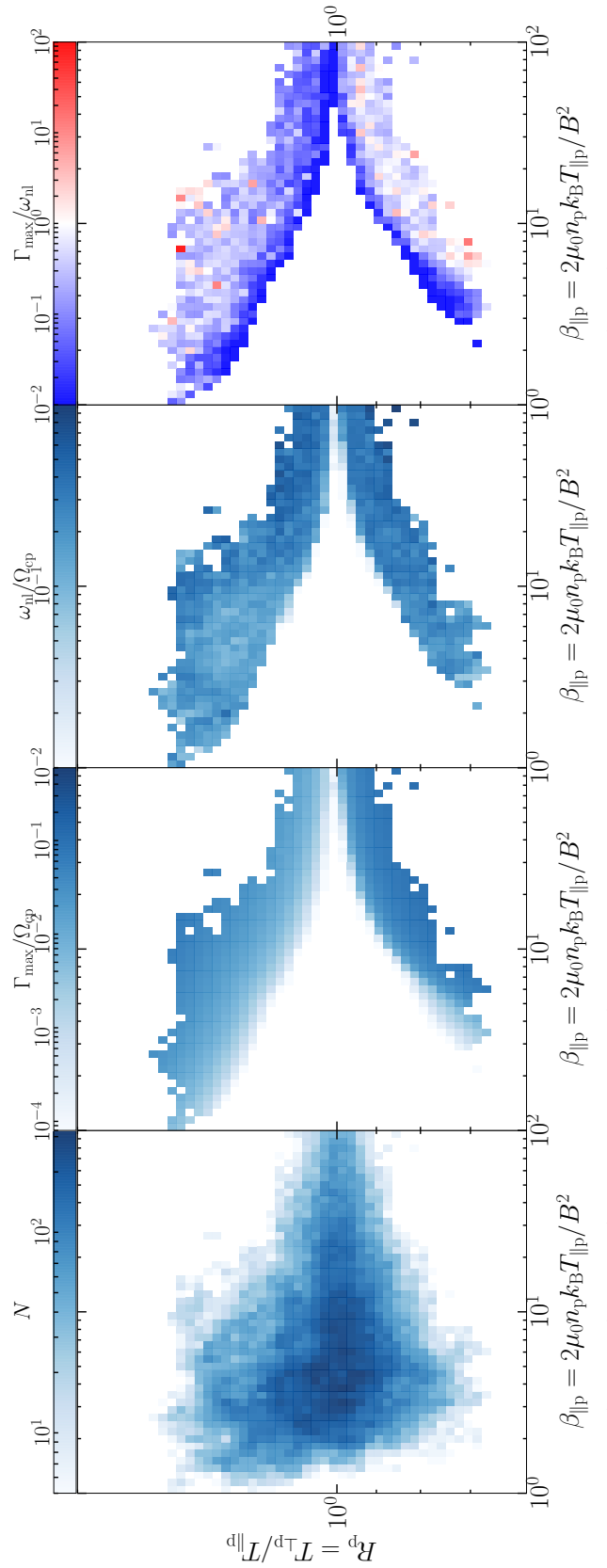


Figure 7.6: ( $R_p, \beta_{\parallel p}$ ) plots (from left to right) of distribution of data, maximum linear growth rate ( $\Gamma_{\max}$ ), nonlinear frequency ( $\omega_{\text{nl}}$ ), and their ratio ( $\Gamma_{\max}/\omega_{\text{nl}}$ ) for earth's magnetosheath.

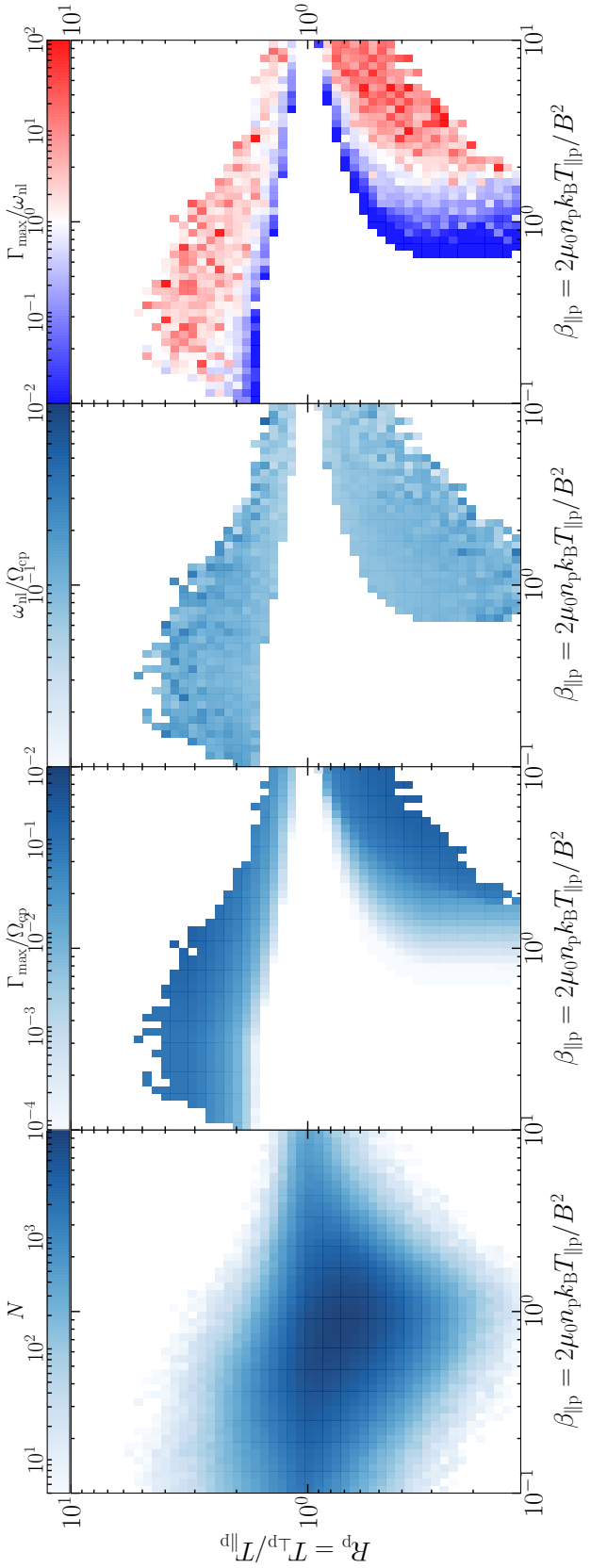


Figure 7.7: ( $R_p, \beta_{\parallel p}$ ) plots (from left to right) of distribution of data, maximum linear growth rate ( $\Gamma_{\max}$ ), nonlinear frequency ( $\omega_{\text{nl}}$ ), and their ratio ( $\Gamma_{\max}/\omega_{\text{nl}}$ ) for solar wind at 1-au.

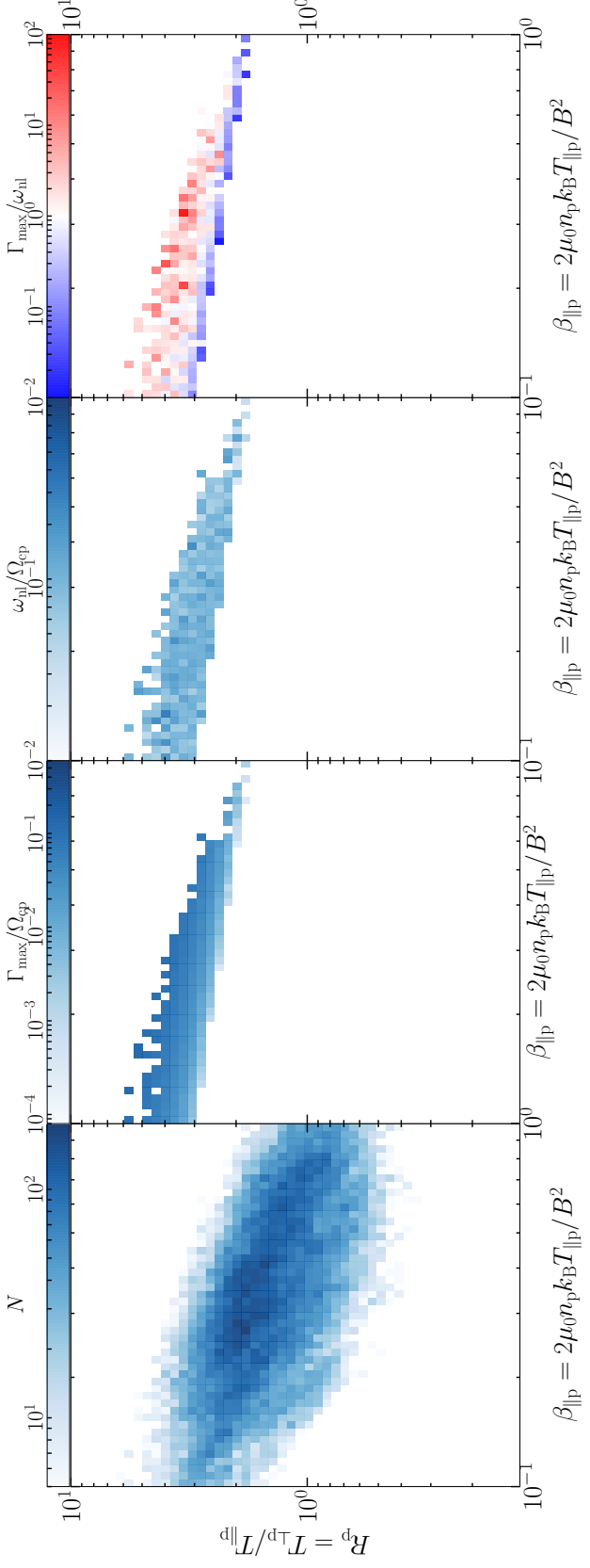


Figure 7.8:  $(R_p, \beta_{\parallel p})$  plots (from left to right) of distribution of data, maximum linear growth rate ( $\Gamma_{\max}$ ), nonlinear frequency ( $\omega_{nl}$ ), and their ratio ( $\Gamma_{\max}/\omega_{nl}$ ) for solar wind close to the Sun.

by turbulence (Osman et al., 2011; Greco et al., 2012; Valentini et al., 2014; Parashar & Matthaeus, 2016), and we know that kinetic microinstabilities are most active where  $R_p$  deviates significantly from unity. Osman et al. (2013) showed that turbulence cascade rates are highest along the edges as well. All this indicates a complicated interplay between turbulent and microkinetic phenomena.

In this chapter we compared linear growth rates derived using linear dispersion relation under the assumption of homogeneity of background fields. An ideal method would involve computation of  $\gamma$  based on theory which takes such inhomogeneities as are present in plasmas into account. Understanding the kind of turbulence present in the system can further assist us in an accurate computation of  $\omega_{nl}$ . Since it is extremely difficult to gauge the kind of turbulence present in a system without the knowledge of magnetic structure a full 3-D image of magnetic field can help substantially. Though development of linear theory based on inhomogeneities has been deferred to future work, in Chapter 8 we discuss a probable future mission and proof of concept for measuring full 3-D structure of magnetic field from kinetic to mesoscales at 1 au.

## Chapter 8

# MAGNETIC FIELD TOPOLOGY RECONSTRUCTION USING MACHINE LEARNING ALGORITHM

### 8.1 Overview

Machine learning, over the last decade has become increasingly relevant in data and image analysis. Both, image reconstruction and data imputation, specifically in a time series, have increasingly relied on machine learning techniques and algorithm (Wang et al., 2018; Bertsimas et al., 2017). In this chapter we apply one such algorithm/technique to a synthetically generated time series dataset of the magnetic field derived from a fully kinetic 3-D simulation of space plasma. This work serves as a proof of concept for a future mission consisting of multiple spacecraft that would map out the topology of the solar-wind's magnetic field.

Section 8.2 motivates the multi-spacecraft observation of space plasmas and the reconstruction of 3-D magnetic field structure. Section 8.3 presents the current state of the field. Synthetic data generation is discussed in Section 8.5 and Section 8.4 discusses the methodology used in detail. Section 8.7 presents the results of the implemented algorithm. The conclusion of the study is summarized in Section 8.8 along with some discussion and suggestions of future works<sup>1</sup>.

### 8.2 Introduction

Over the last 7 decades in-situ observation of solar wind has been carried by different spacecraft starting with Sputnik in 1957 and on going with the most recent mission Solar Orbiter which was launched in 2020. Majority of such missions launched

---

<sup>1</sup> Part of this study was published in Maruca et al. (2021).

a single spacecraft. Observations from these missions have vastly improved and enhanced our understanding of solar wind and its dynamics, thanks to ever increasing, more precise and detailed observations. However, single spacecraft missions cannot differentiate between a temporal and spatial fluctuation. This also means we do not have detailed information of the full 3-D structure of the interplanetary magnetic field. To address this, a few missions have flown with 4 or 5 spacecraft (e.g., Cluster, THEMIS-ARTEMIS, and MMS), and missions with even more spacecraft have been proposed (Klein et al., 2019). Though work done by Fu et al. (2015) and Torbert et al. (2020) using MMS data are promising, they are limited to a single scale. Methodology employed by Fu et al. (2015) also becomes inaccurate if the distance between spacecraft is of the order of ion-inertial length ( $d_i$ ). Given the multi-scale nature of solar wind (Verscharen et al., 2019) we must have a system where we can study the magnetic field by reconstructing it at multiple scales. So far no mission has succeeded in generating a full three dimensional image of the magnetic vector field in the solar wind, mostly because of large number of spacecraft required to carry out such a task and at various length scales. A full 3-D image would provide magnetic field vector at every point within the area being imaged and thus will be able to trace the interplanetary magnetic field lines. It will also get us information related to structure and topology, which are extremely important for understanding turbulence and its evolution in space plasmas, especially how energy is stored in and transported through the plasma.

Though an active field of research, not much work has been done in this from the vantage point of machine learning. In this study we present a proof of concept of magnetic field's topology reconstruction using multi-point observation in a 3-D simulation box. For multi-point observation, we fly a constellation of virtual spacecraft through a simulation box (see Section 8.5), and carry out the interpolation on observed vector data in the 3-D space along its trajectory using Gaussian Processes Regression in machine learning. The study also explores the number of spacecraft, the relative separation between them, and their configuration required for resolving structures of various scales.

### 8.3 Background

Spacecraft make regular in-situ measurement as plasma convects over them. Reconstructing the full 3-D topology of interplanetary magnetic field thus requires interpolating the data from the finite set of spacecraft observations. Different interpolation techniques can be used to achieve this result. Since solar wind is multi-scale in nature ([Verscharen et al., 2019](#)) we will need sufficiently large number of observations to reliably construct the magnetic field at various different scales. For a planar configuration of a constellation of spacecraft where normal to the plane of orientation is in parallel (or anti-parallel) to the solar wind direction, as employed in this study (see Section 8.5 and Figure 8.1), we can make more observations in the parallel flow direction by increasing the cadence of measuring instrument, whereas in the direction perpendicular to the flow, same effect can be achieved by increasing the number of spacecraft.

For interpolation between the observation points, because of the presence of non-linear structures (see Chapter 5) and sharp discontinuities (see Chapter 6), linear interpolation techniques might not be best suited. We thus turn to machine learning algorithms in an effort to minimize the number of spacecraft needed and maximize the feasibility of such a space mission. Several such machine learning methods for the purpose of data imputation have been explored in literature ([Lin & Tsai, 2019](#); [Bertsimas et al., 2017](#); [Wang et al., 2018](#)). As discussed in [Lin & Tsai \(2019\)](#), the best solution or the most appropriate method depends largely on the domain of the problem. What works for one kind of dataset might completely fail for a slightly different one, as we will see in this study as well. For our purpose, we decided to explore GP and develop an algorithm based on it. The rest of this section gives a brief description of GP, some of its salient features, and its key advantages and disadvantages.

#### 8.3.1 Gaussian Processes Regression

Gaussian Processes (GP) as a generic term means that a dataset with finite number of observation is modelled as if it were a multivariate normal distribution

(Gramacy, 2020). It is a probability distribution over possible functions that fit a given finite dataset. Just as a Gaussian distribution is fully characterised by its mean ( $\mu$ ) and covariance ( $\Sigma$ ), a GP is completely defined by (1) a mean function  $m(x)$  indicating the mean at any point of the input space and (2) a covariance function  $K(x, x')$  that sets the covariance between input pairs  $\mathbf{x}$  and  $\mathbf{x}'$  (Rasmussen & Williams, 2006). These can be written as:

$$\begin{aligned} m(\mathbf{x}) &= \mathbb{E}[f(\mathbf{x})] \\ k(\mathbf{x}, \mathbf{x}') &= \mathbb{E}[(f(\mathbf{x}) - m(\mathbf{x}))(f(\mathbf{x}') - m(\mathbf{x}'))] \end{aligned} \quad (8.1)$$

and Gaussian processes can be written as:

$$f(\mathbf{x}) \sim \mathcal{GP}(m(\mathbf{x}), k(\mathbf{x}, \mathbf{x}')) \quad (8.2)$$

The covariance matrices in Equation (8.1) can be computed using a predefined function, which are referred as kernels in GP. This sets a prior to the set of functions which must be considered for a given dataset and the type of kernel chosen defines the characteristics of this prior.

There are several standard kernels (see Section 8.4). For this study, we tried a few which were available through one the Python packages and selected the one most suitable for our dataset.

One of the advantages of using GP in this application is that it is non-parametric and thus, doesn't require a priory fit function to model the input data. It is particularly relevant to our case since we do not have much information about the structure of the solar wind. Rather than relying on fit function, GP look at every possible model and probabilistically explore the space to find the most optimal one for a given dataset. Naively, it will appear that there are infinite functions to be considered here since the probabilistic approach used in GP considers all possible functions. In reality, this is not the case since each function is assigned a prior and the infinite number of functions are defined by their statistics, making the whole method a lot more manageable. Another advantage of GP is its computational tractability (Rasmussen & Williams, 2006).

Selection of an appropriate kernel, though important to the whole process is not critical, as even if we choose a random kernel it often does a decent job of data imputation. Recent development in Deep GP in fact do away with the issue of pre-defining a kernel since it is designed to learn the kernel which works best for a given dataset (Bui et al., 2016). Well calibrated predictive uncertainty estimates and ease of generalization, for both regression and classification analyses, are other benefits of using GP.

As with any method, there are some disadvantages associated with it. One of the major drawback of GP is its computational cost. Since inversion of matrices is required, which makes the method of  $\mathcal{O}(n^3)$ , it is computationally very expensive to run for large number of data points ( $n > 2000$ ) (Gramacy, 2020).

#### 8.4 Kernels in Gaussian Processes

For this study we implemented GP using SciKit Learn package available in Python (Pedregosa et al., 2011). SciKit has a few default kernels implemented in the package, we list out some of them here:

1. Constant Kernel (CK)
2. Radial-basis Function Kernel (RBF)
3. Matérn Kernel (MK)
4. Rational Quadratic Kernel (RQ)
5. Exponential-Sine-Squared Kernel (ESS)

For our study we used these five kernels either individually or in combination with each other. We briefly discuss each of the aforementioned kernels here. A more in-depth discussion of each kernel can be found in Rasmussen & Williams (2006) or on the SciKit Learn web-page<sup>2</sup>.

---

<sup>2</sup> [https://scikit-learn.org/stable/modules/gaussian\\_process.html#kernels-for-gaussian-processes](https://scikit-learn.org/stable/modules/gaussian_process.html#kernels-for-gaussian-processes)

**1. Constant Kernel:** By definition this is simply a constant number or a vector for all points in the space. This is largely useful in combination with other kernels where either modification of magnitude (Product kernel) or change of mean (Sum kernel) is required. The kernel can be written as:

$$k(x_i, x_j) = \text{constant\_value} \quad \forall x_i, x_j \quad (8.3)$$

**2. Radial-basis Function kernel:** The RBF kernel is also known as “squared exponential kernel”. The kernel has one length parameter ‘ $l$ ’ which can be set to either a scalar or something which has same dimension as the input ( $x_i$ ). The length parameter controls the smoothness of the kernel. The kernel is stationary, meaning its covariance function is invariant under translation, and it is infinitely differentiable resulting in smooth outputs. The kernel is given as follows:

$$k(x_i, x_j) = \exp\left(-\frac{d(x_i, x_j)^2}{2l^2}\right) \quad (8.4)$$

where  $d(x_i, x_j)$  is the Euclidean distance between the two points.

**3. Matérn Kernel:** Matérn kernel is the generalized form of RBF with an additional parameter ‘ $\nu$ ’ which controls the smoothness of the resulting function. As  $\nu \rightarrow \infty$ , Matérn kernel approaches RBF. Generally since ‘ $\nu$ ’ is set to some finite value, the resulting output may not be very smooth. However, it gives a mode to control the smoothness of the output. The Matérn kernel is given as:

$$k(x_i, x_j) = \frac{1}{\Gamma(\nu)2^{\nu-1}} \left(\frac{\sqrt{2\nu}}{l}d(x_i, x_j)\right)^\nu K_\nu\left(\frac{\sqrt{2\nu}}{l}d(x_i, x_j)\right) \quad (8.5)$$

where  $K_\nu(\cdot)$  is a modified Bessel function and  $\Gamma(\cdot)$  is the gamma function. For most cases we set ‘nu’ to 3/2 or 5/2 for once or twice differentiability respectively.

**4. Rational Quadratic Kernel:** The kernel is an infinite sum of RBF with various length scales. Just like RBF, RQ has the ‘ $l$ ’ parameter. It also has an additional parameter ‘ $\alpha$ ’ which is the scale mixture parameter. The kernel can be written as:

$$k(x_i, x_j) = \exp\left(-\frac{d(x_i, x_j)^2}{2\alpha l^2}\right)^{-\alpha} \quad (8.6)$$

**5. Exponential-Sine-Squared Kernel:** The kernel has two parameters, length scale ‘ $l$ ’ and periodicity ‘ $p$ ’ consequently making it most suitable for modelling functions with some kind of periodic nature. The kernel can be written as:

$$k(x_i, x_j) = \exp\left(-\frac{2 \sin^2(\pi d(x_i, x_j)/p)}{l^2}\right) \quad (8.7)$$

For our purpose, we mostly used kernels in combination with each other, since most kernels can be added or multiplied to others. After Using several kernels, we observed that a combination of constant and Matérn kernels gave the best result for circular configuration, as shown in Figure 8.1, whereas for grid-like distribution (see Figure 8.2) of spacecraft we found that constant and RQ kernels gave the best result. Thus, the final kernel used to obtain results reported in this study were:

- For a grid-like configuration,

$$\text{kernel}_{\blacksquare} = \text{CK}(2, (10^{-2}, 10^2)) + \text{CK}(2, (10^{-2}, 10^2)) \cdot \text{RQ}(l = 2, \alpha = 0.1) \quad (8.8)$$

- For a circular configuration,

$$\text{kernel}_{\bullet} = \text{CK}(5, (10^{-2}, 10^2)) + \text{CK}(5, (10^{-2}, 10^2)) \cdot \text{MK}(l = [2, 2, 6], \nu = 5/2) \quad (8.9)$$

Where the symbols have the same meaning as defined for Equations (8.3) to (8.7).

## 8.5 Synthetic Data Generation

For implementing the GP as discussed in Section 8.3.1, we would need observation dataset from a constellation of spacecraft. However, since we do not have

such a constellation we use the output from a fully kinetic 3-D simulation, `ros` (see Section 4.2.3 for more details). This enables us to test the effect of various number of spacecraft and their relative orientation and positioning on the quality of reconstructed image. For the ease of computation we down-sampled the original data to have resolution of  $1 d_i$  in the  $xy$ -plane and  $\sim 1/3 d_i$  along the  $z$ -axis. To generate synthetic data from the simulation data, we flew constellations of different number of spacecraft (4 to 36) in different configurations through the simulation box. Figure 8.1 shows one such configuration (radial and planar) for 24 spacecraft. Note that all 24 spacecraft are in one plane and record the time series as plasma passes by at typical solar wind speed ( $\sim 500$  km/s). We simulate the observation at a cadence of  $\sim 13$  Hz which is comparable to modern instruments (see Chapter 4). Under the assumption of Taylor's hypothesis (Taylor, 1938), which lets us convert from a time scale to length scale using the speed of the plasma, solar-wind speed corresponds to consecutive data points separated by approximately  $0.3 d_i$  along the  $z$ -axis. This spacing is small compared to distance between spacecraft ( $2 - 22 d_i$ ) and thus reconstruction along  $z$ -axis is limited by the cadence of observation, whereas along  $xy$ -plane the number of spacecraft limits the resolution.

## 8.6 Methodology

Simulation box size is  $41.9 d_i$ , and thus it takes the constellation roughly 10 seconds to cross the whole box and each spacecraft makes 128 measurement in one flight. We use the synthetic time series data generated from the virtual spacecraft trajectory to train our GP model (see Section 8.4 and Appendix C). If we have  $N$  spacecraft in a given configuration and we have 128 observation along the  $z$ -axis. For one configuration we get  $128 \times N$  data points for each component of the magnetic field to train our model. Once the training is complete, we feed in the coordinates of every point inside the disk of size  $28 d_i$  (a few  $d_i$ 's larger than the size of the constellation) for all the different planes, a total of 128 planes. This means for any number of spacecraft we must make predictions at  $\sim 28 \times 28 \times 128$  points. This implies that greater number

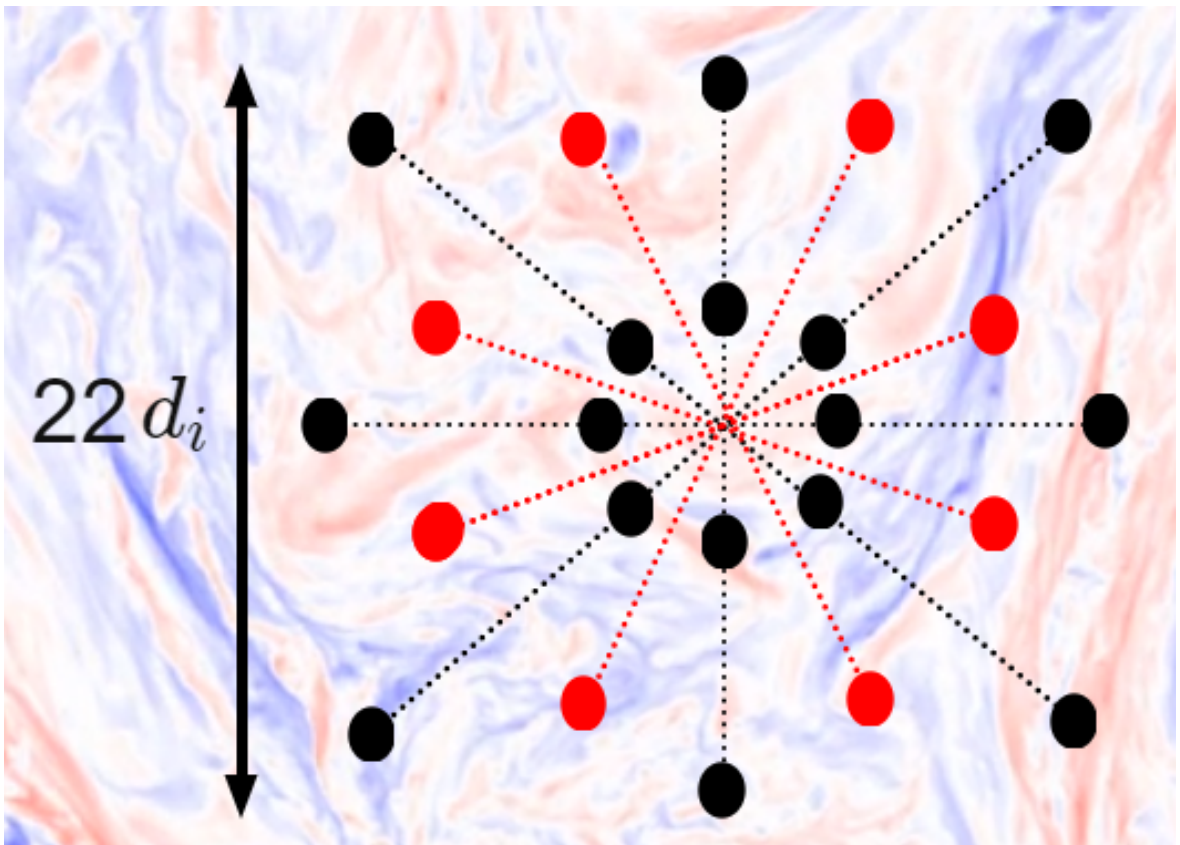


Figure 8.1: One of the many configuration of spacecraft for 24 spacecraft. The inner black circles represent spacecraft at a distance of  $2 d_i$  from the center whereas the outer ones are at  $11 d_i$ . The red dots are the spacecraft at  $7 d_i$  from the center.

of spacecraft in any given configuration will give us better result since it will increase the amount of data used to train the model. However, as with any machine learning algorithm, there is a limit to how well trained a given model can be no matter the amount of input data. We discuss this in further detail in next section.

Once we have the time series data, we trained the specified model on the observed data providing it one component at a time. Once the model is trained and the parameters of the model are learned based on the training set, we provide the model with all the locations in 3-D space where we need to find the value of magnetic field. Appendix C gives the detail of implementation and also provide the code for the same.

## 8.7 Results

Figures 8.2 to 8.5 show one of the slice along xy-plane of the actual simulation data in Panel (a) (down sampled to  $1 d_i$  resolution) and the reconstructed field corresponding to different number of spacecraft employed (4 to 36, represented by the black dots) for observation (Panels b to f). For these figures, as discussed in Section 8.4 reconstructed field were generated using kernel as defined in Equation (8.8). The configurations with 4 and 9 spacecraft poorly reproduce the original simulated field. Only when we have at least 16 spacecraft some structure is captured. Only for a constellation of 25 or more spacecraft does the reconstructed field closely resemble the original field structure. Though there is slight improvement in how well the original field is being captured when we from 25 to 36 spacecraft (as expected), whether this is worth additional expense of adding 11 more spacecraft need further investigation and a quantitative comparison.

Results from circular configurations of spacecraft, for which the kernel in Equation (8.9) was used, are shown in Figures 8.6 to 8.9. As discussed for the previous figures, Panel (a) shows the original data, whereas Panels (b) to (h) show reconstructed field corresponding to different number of spacecraft. The spacecraft are distributed around a common center such that irrespective of the number of spacecraft employed, maximum distance between two spacecraft is always  $22 d_i$  so that they all cover equal

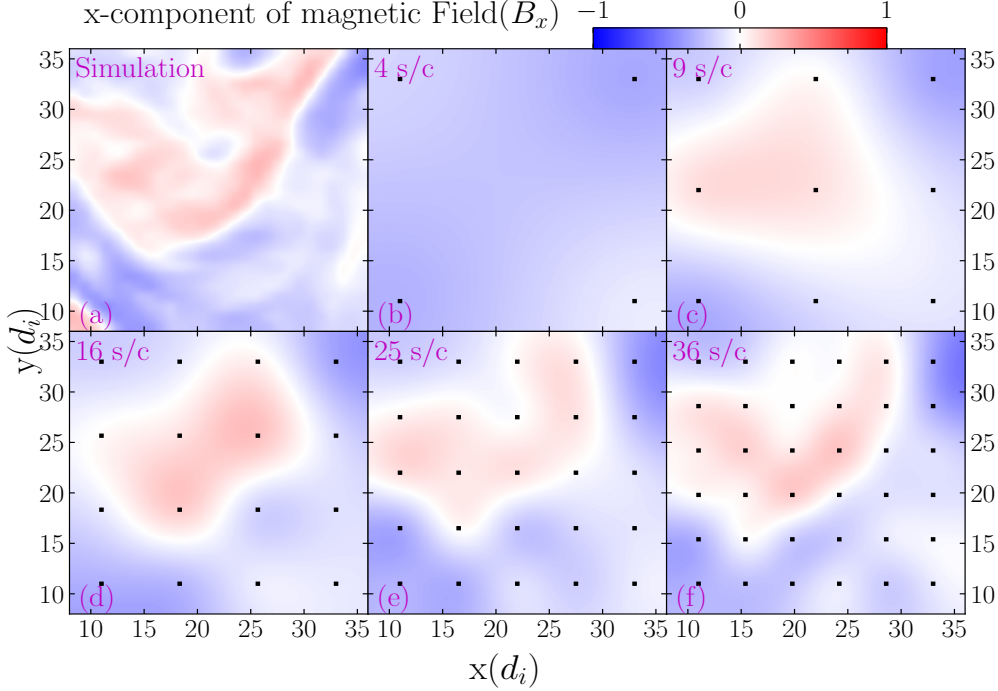


Figure 8.2: x-component of magnetic field from simulation (Panel **a**) and reconstructed field corresponding to different number of spacecraft (Panels **b** to **f**)

volume of space in any given amount of time. As was the case for grid-like configuration, reconstructed fields do not capture any meaningful structure for 4 or 8 spacecraft. Some structure does show up for 16 spacecraft however it is only when we employ 24 or more spacecraft that we get the structure of the field which looks similar to the original input (more on this later).

For 24 spacecraft, we also randomized the position of each spacecraft, such that each spacecraft could be anywhere in a circle of radius  $2 d_i$  from its starting position (see Panel **g**). Reconstructed data, even for randomized position, continue to capture the actual structure of the original field. This observation considerably lessens the burden of having precisely defined orbits of each spacecraft. As long as individual spacecraft can communicate with each other regarding their relative position, reconstruction is not effected in a significant way.

Given that we have a large number of spacecraft, at least 24, for this observation, a scenario might arise where one or more of them fail to function properly, either

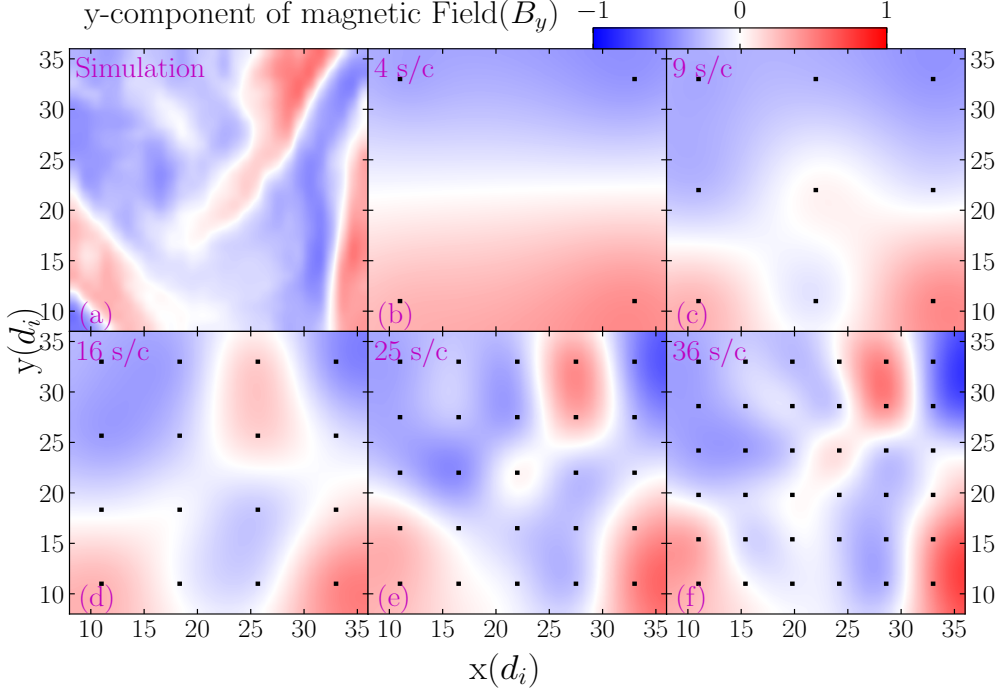


Figure 8.3: y-component of magnetic field from simulation (Panel **a**) and reconstructed field corresponding to different number of spacecraft (Panels **b** to **f**)

because of partial or full failure of instruments or for any other conceivable reason. We considered this scenario in the following way. We record the position of all spacecraft as shown in Panel **(g)** of Figures 8.6 to 8.9 and randomly remove two spacecraft, as shown in Panel **(h)** of the same figures. We then carry out GP on the modified data. Results from such reconstruction are shown in Panel **(h)** of each figure. As one can see, though the quality of reconstruction deteriorates a bit, compared to 24 spacecraft (Panel **e**) it still manages to capture most of the structure present. These two observations (randomized location of spacecraft and random failing of 2 out of 24 spacecraft) shows the robustness of algorithm.

Based on the results we have shown so far, we thus conclude that if such an algorithm were to be applied, we will need at least 24 spacecraft in different configuration.

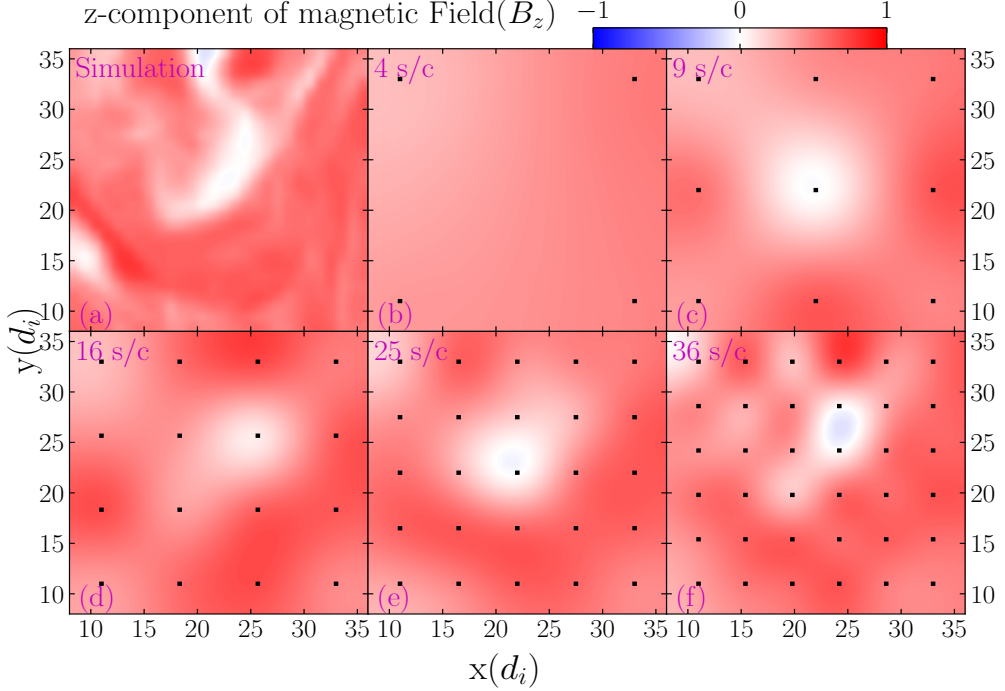


Figure 8.4: z-component of magnetic field from simulation (Panel **a**) and reconstructed field corresponding to different number of spacecraft (Panels **b** to **f**)

## 8.8 Discussions

The unknown nature of turbulence in the solar wind has given rise to competing theories to explain the structure and evolution of the interplanetary magnetic field and how energy is transferred from one scale to another. Measurements from a single spacecraft cannot differentiate between temporal and spatial fluctuations in the field and thus cannot conclusively support or reject any one of these theories. Measurements of the field's complete 3-D morphology and topology will enable us to understand the true nature of solar-wind turbulence. This study thus focused on determining the baseline number of spacecraft required to produce 3-D images of the IMF from in-situ magnetic field measurements.

Using fully kinetic 3-D PIC simulation data, we demonstrated magnetic field topology reconstruction from synthetic time series in 3-D space using Gaussian Processes, a machine learning algorithm. Our results indicate that 24 spacecraft would be required for the satisfactory reconstruction of 3-D IMF structure. We also showed that

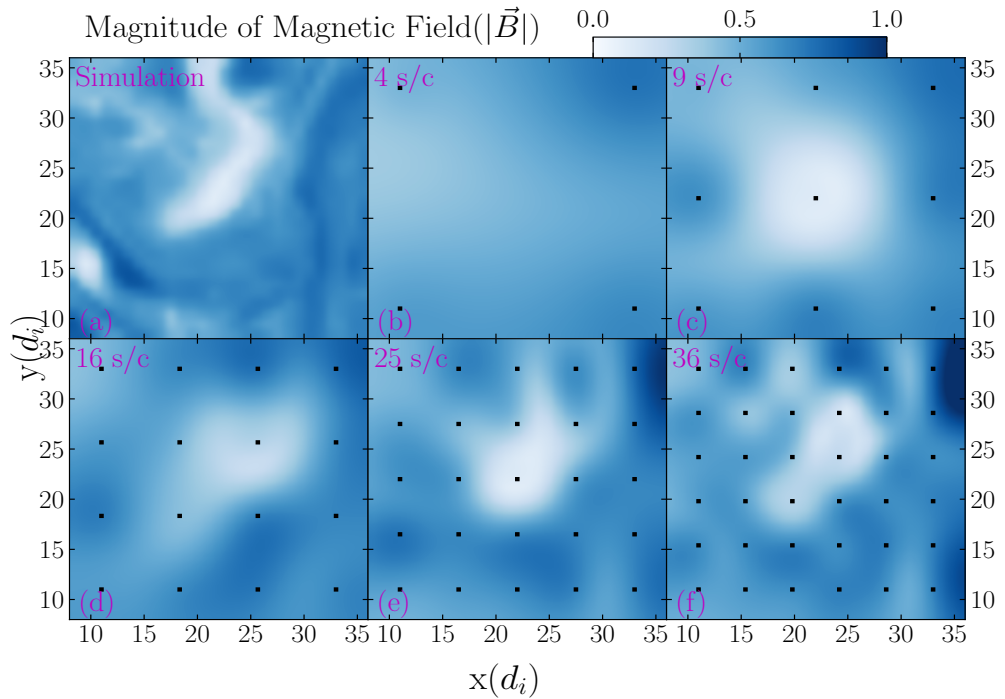


Figure 8.5: Magnitude of magnetic field from simulation (Panel **a**) and reconstructed field corresponding to different number of spacecraft (Panels **b** to **f**)

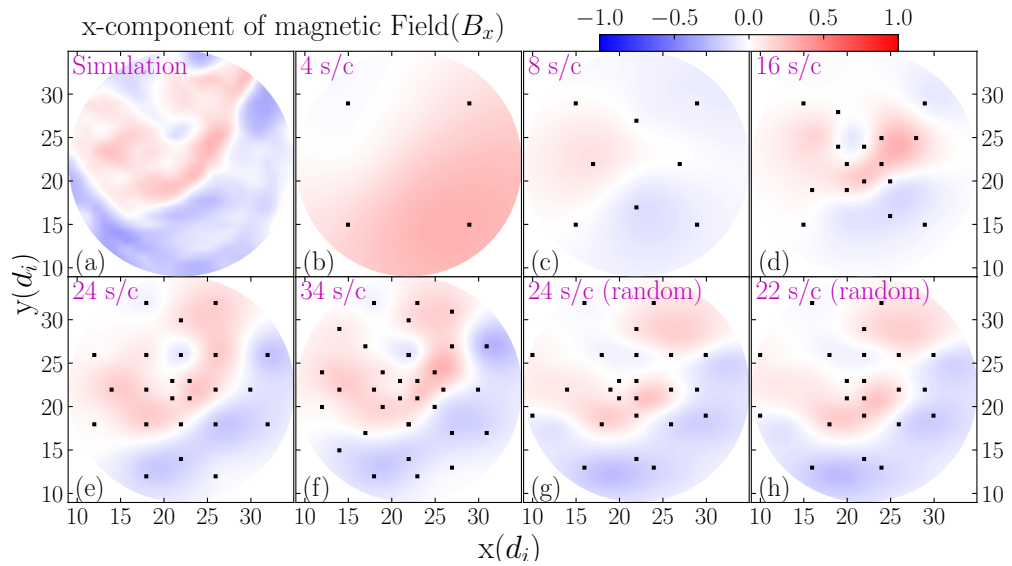


Figure 8.6: x-component of the magnetic field from simulation (a) and various different number for circular configuration of spacecraft (b to h)

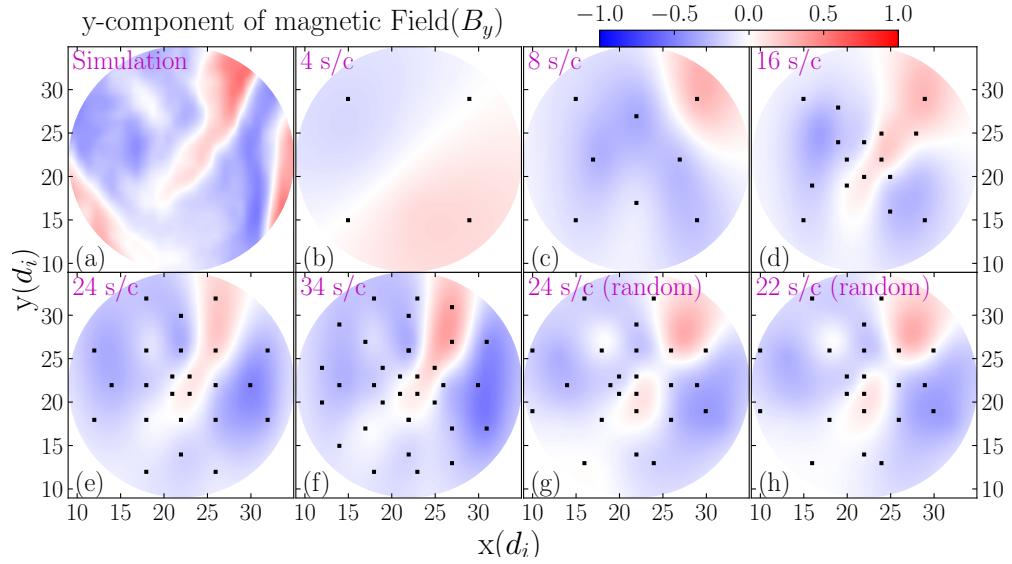


Figure 8.7: y-component of the magnetic field from simulation (a) and various different number for circular configuration of spacecraft (b to h)

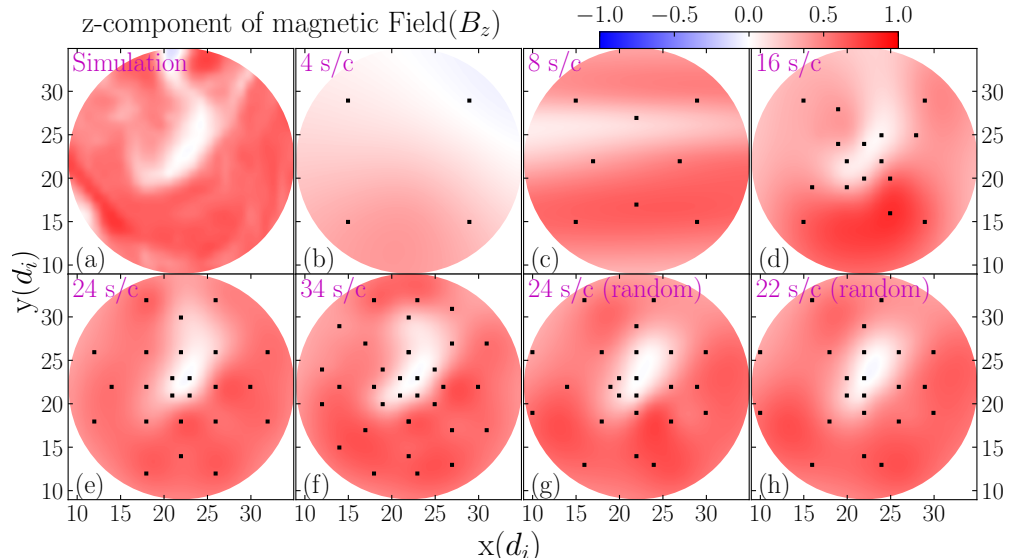


Figure 8.8: z-component of the magnetic field from simulation (a) and various different number for circular configuration of spacecraft (b to h)

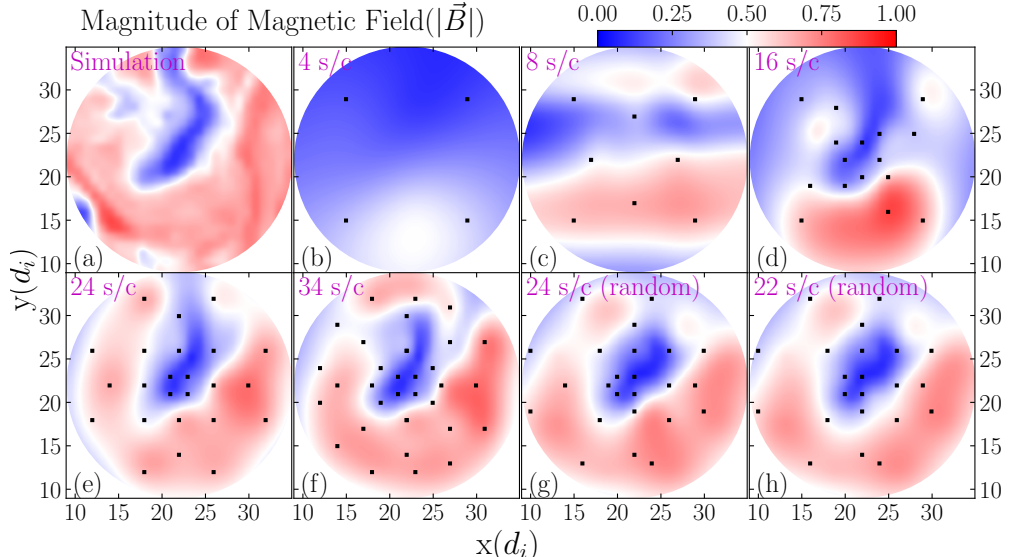


Figure 8.9: Total magnetic field from simulation (a) and various different number for circular configuration of spacecraft (b to h)

precise control of spacecraft trajectory is not required for such a mission so long as the spacecraft positions are known. A baseline of 24 spacecraft even allows for unfavorable alignment of some spacecraft, though substantially fewer spacecraft (e.g., 16) fail to produce consistently adequate IMF reconstructions.

Nevertheless, this study is still very much a work in progress and much needs to be done before we can reach a final version of the algorithm. As stated in Section 8.4, we applied GP to each component of the field individually, ignoring the other two components. In reality the magnetic field components are not fully independent since the magnetic field must be divergence-less. In principle, a kernel could be implemented that would process all three components simultaneously and even enforce the requirement of a divergence-less field (for a 2-D example of this, see [Narcowich et al., 2007](#); [Wahlström et al., 2013](#)). Alternatively a divergence cleaning algorithm could be applied after the GP algorithm has run.

We are also investigating alternative machine learning techniques. For example Deep GP ([Bui et al., 2016](#)) can generate the best kernel for a given dataset rather than requiring the user to select one.

More study is also required of how the arrangement of a given number of spacecraft affects the accuracy of magnetic reconstruction. A key component of this would be developing quantitative metrics for assessing reconstruction quality. A simple point by point comparison cannot take into account the benign distortion and blurring which arises because of reconstruction using a finite number of spacecraft. Instead, we are focusing on physically relevant parameters of magnetic structures: e.g., the connectivity of magnetic fields and the aspect ratios and orientations of regions of weak/strong magnetic field.



## Chapter 9

# CONCLUSION

### 9.1 Broader Context

Space plasmas such as the solar wind and terrestrial magnetosheath are highly structured and dynamic systems. Over the last few decades, two different theoretical frameworks have been developed to study their formation and evolution. The first uses linear Vlasov theory to explore micro-scale phenomena: the effects of waves and the constraints imposed by microinstabilities on the plasmas. The second includes the larger mesoscales and focuses on non-linear processes such as turbulence and the coherent structures it generates.

Though both these frameworks have strong observational supports (see Section 2.3), they are incompatible as traditionally formulated. Linear theory explicitly assumes a homogeneous background for the linear fluctuations that it studies. In contrast, turbulence produces strong inhomogeneities at all scales — including those of linear theory. Reconciling these incongruous theories has motivated the work of this thesis.

We focused our work on ion temperature-anisotropy and heating. Many previous studies have identified the heating of solar wind and magnetosheath to be ubiquitous but strongly inhomogenous (see Section 3.2). The rate of heating varies across time and space and is often highly anisotropic which leads to strong temperature-anisotropies ( $T_{\perp}/T_{\parallel} \neq 1$ ). The observations and simulations strongly indicate that turbulence produces inhomogeneous and anisotropic heating (see Sections 5.4 and 6.5). Likewise, the predicted constraints of linear Vlasov theory align well with the observed distribution of ion temperature-anisotropy (see Section 2.3). Despite their contradictory assumptions,

both turbulence and microinstabilities seem to substantially affect ion-temperature in space plasmas. We conjectured that though turbulence produces inhomogeneities, the plasma remains sufficiently homogeneous at the kinetic micro-scales for the fastest modes of linear instability to develop.

## 9.2 Summary of Key Results

In Chapter 5 we reported our analysis on the interplay of temperature-anisotropy driven linear microkinetic instabilities and intermittency arising as a consequence of turbulence. We showed that the two processes occur in close physical space. We also found the indication that the linear instabilities occur in discrete regions or intervals in different kinds of simulations as well as in in-situ data from space plasmas (see Figures 5.1 to 5.5).

In Chapter 6 we studied how intermittent structures affect the heating of the nascent solar wind and the terrestrial magnetosheath.. We used PVI to quantify intermittency. Study ([Osman et al., 2012b](#)) using the same technique at 1 au shows similar result thereby suggesting the ubiquitous nature of PVI heating. While we observed strong positive correlation between PVI and radial proton-temperature for the solar wind, magnetosheath plasma show little correlation. As discussed in Section 6.5 some of the reasons for poor correlation might be the lower average value of PVI in magnetosheath as compared to the solar wind, small duration of observations as well as the relatively longer duration of the PVI events might be other contributing factors. In any case, this remains poorly understood and rather surprising given the positive correlation observed between PVI and the electron temperature ([Chasapis et al., 2018](#)). For the solar wind, we also found elevated value of conditionally averaged radial temperature up to one correlation length away from the point of a PVI event (see Figure 6.5).

In Chapter 7 we compare the characteristic time scales of microinstabilities to those of turbulence at the same size scales for 6 different datasets. We observed that for the vast majority of data points/regions where the conditions were unstable, turbulence time scale is shorter than linear time scale (see Figures 7.1 to 7.5). This

means that linear instabilities rarely have enough time to grow and affect the plasma before turbulence changes the plasma conditions driving the instability. However, since anisotropy is well regulated by the instability thresholds, we looked at the relative values of two time scales along the edges of Brazil plot. We found that along the edges linear instabilities do become faster than their turbulence counterpart and thus are able to regulate the extreme values of anisotropy (see Figures 7.6 to 7.7).

At present we cannot image full structure of the interplanetary magnetic field using a few spacecraft. However, constellations with larger and larger number of spacecraft are becoming increasingly common with several possible missions to be launched in near future. Thus with a view towards the future, we carried out a study in Chapter 8 to reconstruct the 3-D topology and morphology of the interplanetary magnetic field from observations made by such a constellation with finite number of spacecraft. Using Gaussian Processes in machine learning for different configurations of number and arrangement of spacecraft, we showed that we need a baseline of 24 spacecraft to successfully carry out such a process. A complete 3-D image of the magnetic field will significantly advance our understanding of turbulence in space plasmas and shed light on the exact process of turbulence cascade.



## BIBLIOGRAPHY



## BIBLIOGRAPHY

- Acuna, M. H., Ogilvie, K. W., Baker, D. N., et al. 1995, Space Science Reviews, 71, 5, doi: [10.1007/bf00751323](https://doi.org/10.1007/bf00751323)
- Alerman, B. L., Kasper, J. C., Stevens, M. L., & Koval, A. 2018, The Astrophysical Journal, 864, 112, doi: [10.3847/1538-4357/aad23f](https://doi.org/10.3847/1538-4357/aad23f)
- Bale, S. D., Kasper, J. C., Howes, G. G., et al. 2009, Physical Review Letters, 103, 211101, doi: [10.1103/PhysRevLett.103.211101](https://doi.org/10.1103/PhysRevLett.103.211101)
- Bale, S. D., Goetz, K., Harvey, P. R., et al. 2016, Space Science Reviews, 204, 49, doi: [10.1007/s11214-016-0244-5](https://doi.org/10.1007/s11214-016-0244-5)
- Bale, S. D., Badman, S. T., Bonnell, J. W., et al. 2019, Nature, 576, 237, doi: [10.1038/s41586-019-1818-7](https://doi.org/10.1038/s41586-019-1818-7)
- Bandyopadhyay, R., Matthaeus, W. H., Parashar, T. N., et al. 2020a, The Astrophysical Journal Supplement Series, 246, 61, doi: [10.3847/1538-4365/ab6220](https://doi.org/10.3847/1538-4365/ab6220)
- Bandyopadhyay, R., Qudsi, R. A., Matthaeus, W. H., et al. 2020b, arXiv e-prints, arXiv:2006.10316. <https://arxiv.org/abs/2006.10316>
- Baumjohann, W., & Treumann, R. A. 1996, Basic space plasma physics (Imperial College Press), doi: [10.1142/p015](https://doi.org/10.1142/p015)
- Bertsimas, D., Pawlowski, C., & Zhuo, Y. D. 2017, The Journal of Machine Learning Research, 18, 7133
- Boulos, M. I., Fauchais, P., & Pfender, E. 1994, in Thermal Plasmas (Springer US), 1–47, doi: [10.1007/978-1-4899-1337-1\\_1](https://doi.org/10.1007/978-1-4899-1337-1_1)

- Bui, T. D., Hernández-Lobato, D., Li, Y., Hernández-Lobato, J. M., & Turner, R. E. 2016, arXiv e-prints, arXiv:1602.04133. <https://arxiv.org/abs/1602.04133>
- Burch, J. L., Moore, T. E., Torbert, R. B., & Giles, B. L. 2016, Space Science Reviews, 199, 5, doi: [10.1007/s11214-015-0164-9](https://doi.org/10.1007/s11214-015-0164-9)
- Burlaga, L. F. 1968, Solar Physics, 4, 67, doi: [10.1007/BF00146999](https://doi.org/10.1007/BF00146999)
- Chandran, B. D. G., & Hollweg, J. V. 2009, The Astrophysical Journal, 707, 1659, doi: [10.1088/0004-637x/707/2/1659](https://doi.org/10.1088/0004-637x/707/2/1659)
- Chapman, S. 1916, Philosophical Transactions of the Royal Society of London Series A, 216, 279, doi: [10.1098/rsta.1916.0006](https://doi.org/10.1098/rsta.1916.0006)
- . 1918, Philosophical Transactions of the Royal Society of London. Series A, Containing Papers of a Mathematical or Physical Character, 217, 115, doi: [10.1098/rsta.1918.0005](https://doi.org/10.1098/rsta.1918.0005)
- Chasapis, A. 2021, TBD
- Chasapis, A., Retinò, A., Sahraoui, F., et al. 2015, The Astrophysical Journal, 804, L1, doi: [10.1088/2041-8205/804/1/L1](https://doi.org/10.1088/2041-8205/804/1/L1)
- Chasapis, A., Matthaeus, W. H., Parashar, T. N., et al. 2018, The Astrophysical Journal Letters, 856, L19, doi: [10.3847/2041-8213/aaadf8](https://doi.org/10.3847/2041-8213/aaadf8)
- Chhiber, R., Goldstein, M. L., Maruca, B. A., et al. 2020, The Astrophysical Journal Supplement Series, 246, 31, doi: [10.3847/1538-4365/ab53d2](https://doi.org/10.3847/1538-4365/ab53d2)
- Clerk Maxwell, J. 1867, Philosophical Transactions of the Royal Society of London Series I, 157, 49
- Coleman Jr, P. J. 1968, The Astrophysical Journal, 153, 371
- Cranmer, S. R. 2014, The Astrophysical Journal Supplement Series, 213, 16, doi: [10.1088/0067-0049/213/1/16](https://doi.org/10.1088/0067-0049/213/1/16)

- Cranmer, S. R., & van Ballegooijen, A. A. 2005, The Astrophysical Journal Supplement Series, 156, 265, doi: [10.1086/426507](https://doi.org/10.1086/426507)
- . 2012, The Astrophysical Journal, 754, 92, doi: [10.1088/0004-637x/754/2/92](https://doi.org/10.1088/0004-637x/754/2/92)
- Cranmer, S. R., van Ballegooijen, A. A., & Edgar, R. J. 2007, The Astrophysical Journal Supplement Series, 171, 520, doi: [10.1086/518001](https://doi.org/10.1086/518001)
- Dmitruk, P., Matthaeus, W. H., Milano, L. J., et al. 2002, The Astrophysical Journal, 575, 571, doi: [10.1086/341188](https://doi.org/10.1086/341188)
- Drake, J. F., Shay, M. A., & Swisdak, M. 2008, Physics of Plasmas, 15, 042306, doi: [10.1063/1.2901194](https://doi.org/10.1063/1.2901194)
- Echim, M. M., Lemaire, J., & Lie-Svendsen, Ø. 2010, Surveys in Geophysics, 32, 1, doi: [10.1007/s10712-010-9106-y](https://doi.org/10.1007/s10712-010-9106-y)
- Elsasser, W. M. 1956, Rev. Mod. Phys., 28, 135, doi: [10.1103/RevModPhys.28.135](https://doi.org/10.1103/RevModPhys.28.135)
- Enskog, D. 1917, Kinetische Theorie der Vorgaenge in maessig verduennten Gasen. I. Allgemeiner Teil
- ErdőS, G., & Balogh, A. 2008, Advances in Space Research, 41, 287, doi: [10.1016/j.asr.2007.04.036](https://doi.org/10.1016/j.asr.2007.04.036)
- Feldman, W. C., Asbridge, J. R., & Bame, S. J. 1974, Journal of Geophysical Research, 79, 2319, doi: [10.1029/JA079i016p02319](https://doi.org/10.1029/JA079i016p02319)
- Feldman, W. C., Asbridge, J. R., Bame, S. J., & Montgomery, M. D. 1973a, Journal of Geophysical Research, 78, 2017, doi: [10.1029/JA078i013p02017](https://doi.org/10.1029/JA078i013p02017)
- . 1973b, Journal of Geophysical Research, 78, 6451, doi: [10.1029/JA078i028p06451](https://doi.org/10.1029/JA078i028p06451)
- Feldman, W. C., Asbridge, J. R., Bame, S. J., & Montgomery, M. D. 1974, Reviews of Geophysics and Space Physics, 12, 715, doi: [10.1029/RG012i004p00715](https://doi.org/10.1029/RG012i004p00715)

- Fox, N. J., Velli, M. C., Bale, S. D., et al. 2015, Space Science Reviews, 204, 7, doi: [10.1007/s11214-015-0211-6](https://doi.org/10.1007/s11214-015-0211-6)
- Fu, H. S., Vaivads, A., Khotyaintsev, Y. V., et al. 2015, Journal of Geophysical Research: Space Physics, 120, 3758, doi: <https://doi.org/10.1002/2015JA021082>
- Gary, S. P. 1991, Space Science Reviews, 56, 373, doi: [10.1007/BF00196632](https://doi.org/10.1007/BF00196632)
- . 1993, Theory of Space Plasma Microinstabilities (Cambridge University Press), 193
- Gary, S. P., Anderson, B. J., Denton, R. E., Fuselier, S. A., & McKean, M. E. 1994, Physics of Plasmas, 1, 1676, doi: [10.1063/1.870670](https://doi.org/10.1063/1.870670)
- Gary, S. P., Bandyopadhyay, R., Qudsi, R. A., et al. 2020, The Astrophysical Journal, 901, 160, doi: [10.3847/1538-4357/abb2ac](https://doi.org/10.3847/1538-4357/abb2ac)
- Gary, S. P., & Cairns, I. H. 1999, Journal of Geophysical Research, 104, 19835, doi: [10.1029/1999JA900296](https://doi.org/10.1029/1999JA900296)
- Gary, S. P., Jian, L. K., Broiles, T. W., et al. 2016, Journal of Geophysical Research: Space Physics, 121, 30, doi: [10.1002/2015JA021935](https://doi.org/10.1002/2015JA021935)
- Gary, S. P., & Karimabadi, H. 2006, Journal of Geophysical Research (Space Physics), 111, A11224, doi: [10.1029/2006JA011764](https://doi.org/10.1029/2006JA011764)
- Gary, S. P., Lavraud, B., Thomsen, M. F., Lefebvre, B., & Schwartz, S. J. 2005, Geophysical Research Letters, 32, L13109, doi: [10.1029/2005GL023234](https://doi.org/10.1029/2005GL023234)
- Gary, S. P., Skoug, R. M., Steinberg, J. T., & Smith, C. W. 2001, Geophysical Research Letters, 28, 2759, doi: [10.1029/2001GL013165](https://doi.org/10.1029/2001GL013165)
- Gary, S. P., & Wang, J. 1996, Journal of Geophysical Research: Space Physics, 101, 10749, doi: [10.1029/96JA00323](https://doi.org/10.1029/96JA00323)
- Gingell, P. W., Burgess, D., & Matteini, L. 2015, The Astrophysical Journal, 802, 4, doi: [10.1088/0004-637x/802/1/4](https://doi.org/10.1088/0004-637x/802/1/4)

Goldstein, S. 1969, Annual Review of Fluid Mechanics, 1, 1, doi: [10.1146/annurev.fl.01.010169.000245](https://doi.org/10.1146/annurev.fl.01.010169.000245)

Gramacy, R. B. 2020, Surrogates: Gaussian Process Modeling, Design and Optimization for the Applied Sciences (Boca Raton, Florida: Chapman Hall/CRC)

Greco, A., Chuychai, P., Matthaeus, W. H., Servidio, S., & Dmitruk, P. 2008, Geophysical Research Letters, 35, L19111, doi: [10.1029/2008GL035454](https://doi.org/10.1029/2008GL035454)

Greco, A., Matthaeus, W. H., Perri, S., et al. 2018, Space Science Reviews, 214, 1, doi: [10.1007/s11214-017-0435-8](https://doi.org/10.1007/s11214-017-0435-8)

Greco, A., Matthaeus, W. H., Servidio, S., Chuychai, P., & Dmitruk, P. 2009, The Astrophysical Journal, 691, L111, doi: [10.1088/0004-637X/691/2/L111](https://doi.org/10.1088/0004-637X/691/2/L111)

Greco, A., & Perri, S. 2014, The Astrophysical Journal, 784, 163, doi: [10.1088/0004-637x/784/2/163](https://doi.org/10.1088/0004-637x/784/2/163)

Greco, A., Perri, S., Servidio, S., Yordanova, E., & Veltri, P. 2016, The Astrophysical Journal, 823, L39, doi: [10.3847/2041-8205/823/2/139](https://doi.org/10.3847/2041-8205/823/2/139)

Greco, A., Valentini, F., Servidio, S., & Matthaeus, W. H. 2012, Physical Review E, 86, 066405, doi: [10.1103/PhysRevE.86.066405](https://doi.org/10.1103/PhysRevE.86.066405)

Gringauz, K. I., Bezrokokikh, V. V., Ozerov, V. D., & Rybchinskii, R. E. 1960, Soviet Physics Doklady, 5, 361

Gutynska, O., Šafránková, J., & Němeček, Z. 2008, Annales Geophysicae, 26, 2503, doi: [10.5194/angeo-26-2503-2008](https://doi.org/10.5194/angeo-26-2503-2008)

Hannesson, C., Johnson, C. L., Mittelholz, A., Asad, M. M. A., & Goldblatt, C. 2020, Journal of Geophysical Research: Space Physics, 125, doi: [10.1029/2019ja027139](https://doi.org/10.1029/2019ja027139)

He, J., Marsch, E., Tu, C., Yao, S., & Tian, H. 2011, The Astrophysical Journal, 731, 85, doi: [10.1088/0004-637x/731/2/85](https://doi.org/10.1088/0004-637x/731/2/85)

Hefti, S., Grünwaldt, H., Ipavich, F. M., et al. 1998, Journal of Geophysical Research, 103, 29697, doi: [10.1029/1998JA900022](https://doi.org/10.1029/1998JA900022)

Hellinger, P., Trávníček, P. M., Štverák, Š., Matteini, L., & Velli, M. 2013, Journal of Geophysical Research: Space Physics, 118, 1351, doi: [10.1002/jgra.50107](https://doi.org/10.1002/jgra.50107)

Hellinger, P., Trávníček, P., Kasper, J. C., & Lazarus, A. J. 2006, Geophysical Research Letters, 33, L09101, doi: [10.1029/2006GL025925](https://doi.org/10.1029/2006GL025925)

Hossain, M., Gray, P. C., Pontius, D. H., Matthaeus, W. H., & Oughton, S. 1995, Physics of Fluids, 7, 2886, doi: [10.1063/1.868665](https://doi.org/10.1063/1.868665)

Howes, G. G. 2015, Philosophical Transactions of the Royal Society of London Series A, 373, 20140145, doi: [10.1098/rsta.2014.0145](https://doi.org/10.1098/rsta.2014.0145)

Huang, J., Kasper, J. C., Vech, D., et al. 2020, The Astrophysical Journal Supplement Series, 246, 70, doi: [10.3847/1538-4365/ab74e0](https://doi.org/10.3847/1538-4365/ab74e0)

Hudson, P. 1970, Planetary and Space Science, 18, 1611 , doi: [https://doi.org/10.1016/0032-0633\(70\)90036-X](https://doi.org/10.1016/0032-0633(70)90036-X)

Isaacs, J. J., Tassein, J. A., & Matthaeus, W. H. 2015, Journal of Geophysical Research (Space Physics), 120, 868, doi: [10.1002/2014JA020661](https://doi.org/10.1002/2014JA020661)

Jeans, J. H. 1905, Nature, 72, 101, doi: [10.1038/072101d0](https://doi.org/10.1038/072101d0)

Jian, L. K., Russell, C. T., Luhmann, J. G., et al. 2010, Journal of Geophysical Research (Space Physics), 115, A12115, doi: [10.1029/2010JA015737](https://doi.org/10.1029/2010JA015737)

—. 2009, The Astrophysical Journal Letters, 701, L105, doi: [10.1088/0004-637X/701/2/L105](https://doi.org/10.1088/0004-637X/701/2/L105)

Jian, L. K., Wei, H. Y., Russell, C. T., et al. 2014, The Astrophysical Journal, 786, 123, doi: [10.1088/0004-637X/786/2/123](https://doi.org/10.1088/0004-637X/786/2/123)

Karimabadi, H., Roytershteyn, V., Wan, M., et al. 2013, Physics of Plasmas, 20, 012303, doi: [10.1063/1.4773205](https://doi.org/10.1063/1.4773205)

Kasper, J. C., Lazarus, A. J., & Gary, S. P. 2002, Geophysical Research Letters, 29, 20, doi: [10.1029/2002GL015128](https://doi.org/10.1029/2002GL015128)

Kasper, J. C., Lazarus, A. J., & Gary, S. P. 2008, Physical Review Letters, 101, 261103, doi: [10.1103/PhysRevLett.101.261103](https://doi.org/10.1103/PhysRevLett.101.261103)

Kasper, J. C., Stevens, M. L., Korreck, K. E., et al. 2012, The Astrophysical Journal, 745, 162, doi: [10.1088/0004-637x/745/2/162](https://doi.org/10.1088/0004-637x/745/2/162)

Kasper, J. C., Abiad, R., Austin, G., et al. 2016, Space Science Reviews, 204, 131, doi: [10.1007/s11214-015-0206-3](https://doi.org/10.1007/s11214-015-0206-3)

Kasper, J. C., Bale, S. D., Belcher, J. W., et al. 2019, Nature, 576, 228, doi: [10.1038/s41586-019-1813-z](https://doi.org/10.1038/s41586-019-1813-z)

Kiyani, K. H., Chapman, S. C., Khotyaintsev, Y. V., Dunlop, M. W., & Sahraoui, F. 2009, Phys. Rev. Lett., 103, doi: [10.1103/PhysRevLett.103.075006](https://doi.org/10.1103/PhysRevLett.103.075006)

Klein, K. G., Alerman, B. L., Stevens, M. L., Vech, D., & Kasper, J. C. 2018, Physical Review Letters, 120, 205102, doi: [10.1103/PhysRevLett.120.205102](https://doi.org/10.1103/PhysRevLett.120.205102)

Klein, K. G., & Howes, G. G. 2015, Phys. Plasmas, 22, 032903, doi: [10.1063/1.4914933](https://doi.org/10.1063/1.4914933)

Klein, K. G., Howes, G. G., TenBarge, J. M., & Podesta, J. J. 2014, The Astrophysical Journal, 785, 138, doi: [10.1088/0004-637x/785/2/138](https://doi.org/10.1088/0004-637x/785/2/138)

Klein, K. G., Alexandrova, O., Bookbinder, J., et al. 2019, arXiv e-prints, arXiv:1903.05740. <https://arxiv.org/abs/1903.05740>

Klein, K. G., Verniero, J. L., Alerman, B., et al. 2021, The Astrophysical Journal, 909, 7, doi: [10.3847/1538-4357/abd7a0](https://doi.org/10.3847/1538-4357/abd7a0)

Kolmogorov, A. 1941a, Akademiiia Nauk SSSR Doklady, 30, 301

Kolmogorov, A. N. 1941b, Akademiiia Nauk SSSR Doklady, 32, 16

Kolmogorov, A. N. 1962, Journal of Fluid Mechanics, 13, 82?85, doi: [10.1017/S0022112062000518](https://doi.org/10.1017/S0022112062000518)

Krishna Jagarlamudi, V., Dudok de Wit, T., Krasnoselskikh, V., & Maksimovic, M. 2019, The Astrophysical Journal, 871, 68, doi: [10.3847/1538-4357/aaef2e](https://doi.org/10.3847/1538-4357/aaef2e)

Landau, L. 1936, Phys. Z. Sowjetunion, 10, 154

Langmuir, I. 1928, Proceedings of the National Academy of Science, 14, 627, doi: [10.1073/pnas.14.8.627](https://doi.org/10.1073/pnas.14.8.627)

Le, G., Russell, C. T., & Orlowski, D. S. 1993, Geophysical Research Letters, 20, 1755, doi: [10.1029/93gl01985](https://doi.org/10.1029/93gl01985)

Lepping, R. P., Acuña, M. H., Burlaga, L. F., et al. 1995, Space Science Reviews, 71, 207, doi: [10.1007/bf00751330](https://doi.org/10.1007/bf00751330)

Lin, W.-C., & Tsai, C.-F. 2019, Artificial Intelligence Review, 53, 1487, doi: [10.1007/s10462-019-09709-4](https://doi.org/10.1007/s10462-019-09709-4)

Lionello, R., Velli, M., Downs, C., et al. 2014, The Astrophysical Journal, 784, 120, doi: [10.1088/0004-637x/784/2/120](https://doi.org/10.1088/0004-637x/784/2/120)

MacBride, B. T., Smith, C. W., & Forman, M. A. 2008, The Astrophysical Journal, 679, 1644, doi: [10.1086/529575](https://doi.org/10.1086/529575)

Maksimovic, M., Pierrard, V., & Riley, P. 1997, Geophysical Research Letters, 24, 1151, doi: [10.1029/97gl00992](https://doi.org/10.1029/97gl00992)

Marsch, E. 2006, Living Reviews in Solar Physics, 3, 1, doi: [10.12942/lrsp-2006-1](https://doi.org/10.12942/lrsp-2006-1)

Marsch, E. 2010, Space Science Reviews, 172, 23, doi: [10.1007/s11214-010-9734-z](https://doi.org/10.1007/s11214-010-9734-z)

Marsch, E., Goertz, C. K., & Richter, K. 1982, Journal of Geophysical Research, 87, 5030, doi: [10.1029/JA087iA07p05030](https://doi.org/10.1029/JA087iA07p05030)

Marsch, E., Liu, S., Rosenbauer, H., & Tu, C. Y. 1992, in ESA Special Publication, Vol. 346, Study of the Solar-Terrestrial System, ed. J. J. Hunt, 315–320

Marsch, E., MÃ¶hlhÃ¶user, K.-H., Rosenbauer, H., Schwenn, R., & Neubauer, F. M. 1982a, J. Geophys. Res., 87, 35, doi: [10.1029/ja087ia01p00035](https://doi.org/10.1029/ja087ia01p00035)

Marsch, E., Schwenn, R., Rosenbauer, H., et al. 1982b, Journal of Geophysical Research, 87, 52, doi: [10.1029/JA087iA01p00052](https://doi.org/10.1029/JA087iA01p00052)

Maruca, B., Kasper, J., & Bale, S. 2011, Phys. Rev. Lett., 107, 201101, doi: [10.1103/PhysRevLett.107.201101](https://doi.org/10.1103/PhysRevLett.107.201101)

Maruca, B. A. 2012a, PhD thesis, Harvard University. <http://nrs.harvard.edu/urn-3:HUL.InstRepos:9547903>

—. 2012b, PhD thesis, Harvard. <https://dash.harvard.edu/handle/1/9547903>

Maruca, B. A., Bale, S. D., Sorriso-Valvo, L., Kasper, J. C., & Stevens, M. L. 2013, Physical Review Letters, 111, 241101, doi: [10.1103/PhysRevLett.111.241101](https://doi.org/10.1103/PhysRevLett.111.241101)

Maruca, B. A., Kasper, J. C., & Gary, S. P. 2012, The Astrophysical Journal, 748, 137, doi: [10.1088/0004-637X/748/2/137](https://doi.org/10.1088/0004-637X/748/2/137)

Maruca, B. A., Chasapis, A., Gary, S. P., et al. 2018, The Astrophysical Journal, 866, 25, doi: [10.3847/1538-4357/aaddfb](https://doi.org/10.3847/1538-4357/aaddfb)

Maruca, B. A., Agudelo Rueda, J. A., Bandyopadhyay, R., et al. 2021, Frontiers in Astronomy and Space Sciences, 8, 108

Matteini, L., Landi, S., Hellinger, P., et al. 2007, Geophysical Research Letters, 34, 20105, doi: [10.1029/2007GL030920](https://doi.org/10.1029/2007GL030920)

Matthaeus, W. H. 2021, Physics of Plasmas, 28, 032306, doi: [10.1063/5.0041540](https://doi.org/10.1063/5.0041540)

Matthaeus, W. H., & Goldstein, M. L. 1982, Journal of Geophysical Research, 87, 6011, doi: [10.1029/ja087ia08p06011](https://doi.org/10.1029/ja087ia08p06011)

Matthaeus, W. H., & Lamkin, S. L. 1986, The Physics of Fluids, 29, 2513, doi: [10.1063/1.866004](https://doi.org/10.1063/1.866004)

Matthaeus, W. H., & Montgomery, D. 1980, Annals of the New York Academy of Sciences, 357, 203, doi: [10.1111/j.1749-6632.1980.tb29687.x](https://doi.org/10.1111/j.1749-6632.1980.tb29687.x)

Matthaeus, W. H., & Velli, M. 2011, Space Science Reviews, 160, 145, doi: [10.1007/s11214-011-9793-9](https://doi.org/10.1007/s11214-011-9793-9)

Matthaeus, W. H., Wan, M., Servidio, S., et al. 2015, Philosophical Transactions of the Royal Society of London Series A, 373, 20140154, doi: [10.1098/rsta.2014.0154](https://doi.org/10.1098/rsta.2014.0154)

Matthaeus, W. H., Zank, G. P., Oughton, S., Mullan, D. J., & Dmitruk, P. 1999, The Astrophysical Journal, 523, L93, doi: [10.1086/312259](https://doi.org/10.1086/312259)

McComas, D. J., Christian, E. R., Cohen, C. M. S., et al. 2019, Nature, 576, 223, doi: [10.1038/s41586-019-1811-1](https://doi.org/10.1038/s41586-019-1811-1)

Narcowich, F. J., Ward, J. D., & Wright, G. B. 2007, Journal of Fourier Analysis and Applications, 13, 643

Ness, N. F., & Burlaga, L. F. 2001, Journal of Geophysical Research: Space Physics, 106, 15803, doi: [10.1029/2000JA000118](https://doi.org/10.1029/2000JA000118)

Neugebauer, M. 2006, Journal of Geophysical Research: Space Physics, 111, doi: [10.1029/2005JA011497](https://doi.org/10.1029/2005JA011497)

Neugebauer, M., & Snyder, C. W. 1962, Science, 138, 1095. <http://www.jstor.org/stable/1709487>

Nicolaou, G., Livadiotis, G., & Wicks, R. T. 2020, Entropy, 22, 212, doi: [10.3390/e22020212](https://doi.org/10.3390/e22020212)

- Ogilvie, K. W., Chornay, D. J., Fritzenreiter, R. J., et al. 1995, Space Science Reviews, 71, 55, doi: [10.1007/bf00751326](https://doi.org/10.1007/bf00751326)
- Osman, K. T., Matthaeus, W. H., Greco, A., & Servidio, S. 2011, The Astrophysical Journal, 727, L11, doi: [10.1088/2041-8205/727/1/L11](https://doi.org/10.1088/2041-8205/727/1/L11)
- Osman, K. T., Matthaeus, W. H., Hnat, B., & Chapman, S. C. 2012a, Physical Review Letters, 108, 261103, doi: [10.1103/PhysRevLett.108.261103](https://doi.org/10.1103/PhysRevLett.108.261103)
- Osman, K. T., Matthaeus, W. H., Kiyani, K. H., Hnat, B., & Chapman, S. C. 2013, Physical Review Letters, 111, 201101, doi: [10.1103/PhysRevLett.111.201101](https://doi.org/10.1103/PhysRevLett.111.201101)
- Osman, K. T., Matthaeus, W. H., Wan, M., & Rappazzo, A. F. 2012b, Physical Review Letters, 108, 261102, doi: [10.1103/PhysRevLett.108.261102](https://doi.org/10.1103/PhysRevLett.108.261102)
- Oughton, S., Priest, E. R., & Matthaeus, W. H. 1994, Journal of Fluid Mechanics, 280, 95, doi: [10.1017/s0022112094002867](https://doi.org/10.1017/s0022112094002867)
- Parashar, T. N., & Gary, S. P. 2019, The Astrophysical Journal, 882, 29, doi: [10.3847/1538-4357/ab2fc8](https://doi.org/10.3847/1538-4357/ab2fc8)
- Parashar, T. N., & Matthaeus, W. H. 2016, The Astrophysical Journal, 832, 57, doi: [10.3847/0004-637X/832/1/57](https://doi.org/10.3847/0004-637X/832/1/57)
- Parashar, T. N., Matthaeus, W. H., & Shay, M. A. 2018a, The Astrophysical Journal, 864, L21, doi: [10.3847/2041-8213/aadb8b](https://doi.org/10.3847/2041-8213/aadb8b)
- Parashar, T. N., Shay, M. A., Cassak, P. A., & Matthaeus, W. H. 2009, Physics of Plasmas, 16, 032310, doi: [10.1063/1.3094062](https://doi.org/10.1063/1.3094062)
- Parashar, T. N., Chasapis, A., Bandyopadhyay, R., et al. 2018b, Phys. Rev. Lett., 121, 265101, doi: [10.1103/PhysRevLett.121.265101](https://doi.org/10.1103/PhysRevLett.121.265101)
- Parashar, T. N., Goldstein, M. L., Maruca, B. A., et al. 2020, The Astrophysical Journal Supplement Series, 246, 58, doi: [10.3847/1538-4365/ab64e6](https://doi.org/10.3847/1538-4365/ab64e6)

- Parker, E. N. 1958, *The Astrophysical Journal*, 128, 664, doi: [10.1086/146579](https://doi.org/10.1086/146579)
- . 1960, *The Astrophysical Journal*, 132, 821, doi: [10.1086/146985](https://doi.org/10.1086/146985)
- . 1963, *Interplanetary dynamical processes*. (Interscience Publishers)
- Pedregosa, F., Varoquaux, G., Gramfort, A., et al. 2011, *Journal of Machine Learning Research*, 12, 2825
- Perez, J. C., & Chandran, B. D. G. 2013, *The Astrophysical Journal*, 776, 124, doi: [10.1088/0004-637x/776/2/124](https://doi.org/10.1088/0004-637x/776/2/124)
- Perrone, D., Alexandrova, O., Mangeney, A., et al. 2016, *The Astrophysical Journal*, 826, 196, doi: [10.3847/0004-637x/826/2/196](https://doi.org/10.3847/0004-637x/826/2/196)
- Perrone, D., Alexandrova, O., Roberts, O. W., et al. 2017, *The Astrophysical Journal*, 849, 49, doi: [10.3847/1538-4357/aa9022](https://doi.org/10.3847/1538-4357/aa9022)
- Pierrard, V., & Lazar, M. 2010, *Solar Physics*, 267, 153
- Pierrard, V., & Pieters, M. 2014, *Journal of Geophysical Research: Space Physics*, 119, 9441, doi: [10.1002/2014ja020678](https://doi.org/10.1002/2014ja020678)
- PlasmaPy Community. 2020, PlasmaPy, <http://doi.org/10.5281/zenodo.4313063>
- Podesta, J. J. 2013, *Solar Physics*, 286, 529, doi: [10.1007/s11207-013-0258-z](https://doi.org/10.1007/s11207-013-0258-z)
- Pollock, C., Moore, T., Jacques, A., et al. 2016, *Space Science Reviews*, 199, 331, doi: [10.1007/s11214-016-0245-4](https://doi.org/10.1007/s11214-016-0245-4)
- Qudsi, R. A., Bandyopadhyay, R., Maruca, B. A., et al. 2020a, *The Astrophysical Journal*, 895, 83, doi: [10.3847/1538-4357/ab89ad](https://doi.org/10.3847/1538-4357/ab89ad)
- Qudsi, R. A., Maruca, B. A., Matthaeus, W. H., et al. 2020b, *The Astrophysical Journal Supplement Series*, 246, 46, doi: [10.3847/1538-4365/ab5c19](https://doi.org/10.3847/1538-4365/ab5c19)

Rasmussen, C. E., & Williams, C. K. I. 2006, Gaussian Processes for Machine Learning (Nonw)

Reynolds, O. 1883, Philosophical Transactions of the Royal society of London, 935, doi: [10.1098/rstl.1886.0005](https://doi.org/10.1098/rstl.1886.0005)

—. 1886, Philosophical Transactions of the Royal Society of London, 177, 157, doi: [10.1098/rstl.1886.0005](https://doi.org/10.1098/rstl.1886.0005)

Roytershteyn, V., Karimabadi, H., & Roberts, A. 2015, Philosophical Transactions of the Royal Society of London Series A, 373, 20140151, doi: [10.1098/rsta.2014.0151](https://doi.org/10.1098/rsta.2014.0151)

Russell, C. T., Anderson, B. J., Baumjohann, W., et al. 2016, Space Science Reviews, 199, 189, doi: [10.1007/s11214-014-0057-3](https://doi.org/10.1007/s11214-014-0057-3)

S. Servidio, F. Valentini, F. C., & Veltri, P. 2012, Physical Review Letters, doi: [10.1103/PhysRevLett.108.045001](https://doi.org/10.1103/PhysRevLett.108.045001)

Sahraoui, F., Goldstein, M. L., Belmont, G., Canu, P., & Rezeau, L. 2010, Phys. Rev. Lett., 105, 131101, doi: [10.1103/PhysRevLett.105.131101](https://doi.org/10.1103/PhysRevLett.105.131101)

Schekochihin, A. A., Parker, J. T., Highcock, E. G., et al. 2016, Journal of Plasma Physics, 82, 905820212, doi: [10.1017/S0022377816000374](https://doi.org/10.1017/S0022377816000374)

Schwartz, S. J. 1980, Reviews of Geophysics and Space Physics, 18, 313, doi: [10.1029/RG018i001p00313](https://doi.org/10.1029/RG018i001p00313)

Servidio, S., Valentini, F., Califano, F., & Veltri, P. 2012, Phys. Rev. Lett., 108, 045001, doi: [10.1103/PhysRevLett.108.045001](https://doi.org/10.1103/PhysRevLett.108.045001)

Servidio, S., Valentini, F., Perrone, D., et al. 2015, Journal of Plasma Physics, 81, 325810107, doi: [10.1017/S0022377814000841](https://doi.org/10.1017/S0022377814000841)

Shebalin, J. V., Matthaeus, W. H., & Montgomery, D. 1983, Journal of plasma physics, 29, 525

Smith, C. W., Matthaeus, W. H., Zank, G. P., et al. 2001, Journal of Geophysical Research, 106, 8253, doi: [10.1029/2000JA000366](https://doi.org/10.1029/2000JA000366)

Sorriso-Valvo, L., Carbone, V., Veltri, P., Consolini, G., & Bruno, R. 1999, Geophysical Research Letters, 26, 1801, doi: [10.1029/1999GL900270](https://doi.org/10.1029/1999GL900270)

Sorriso-Valvo, L., Marino, R., Carbone, V., et al. 2007, Physical review letters, 99, 115001

Sorriso-Valvo, L., Catapano, F., Retinò, A., et al. 2019, Phys. Rev. Lett., 122, 035102, doi: [10.1103/PhysRevLett.122.035102](https://doi.org/10.1103/PhysRevLett.122.035102)

Stix, T. H. 1992, Waves in plasmas (AIP Press)

Taylor, G. I. 1938, Proceedings of the Royal Society of London Series A, 164, 476, doi: [10.1098/rspa.1938.0032](https://doi.org/10.1098/rspa.1938.0032)

Telloni, D., & Bruno, R. 2016, Monthly Notices of the Royal Astronomical Society: Letters, 463, L79, doi: [10.1093/mnrasl/slw135](https://doi.org/10.1093/mnrasl/slw135)

TenBarge, J. M., & Howes, G. G. 2013, The Astrophysical Journal, 771, L27, doi: [10.1088/2041-8205/771/2/127](https://doi.org/10.1088/2041-8205/771/2/127)

Terasawa, T., Hoshino, M., Sakai, J.-I., & Hada, T. 1986, Journal of Geophysical Research, 91, 4171, doi: [10.1029/ja091ia04p04171](https://doi.org/10.1029/ja091ia04p04171)

Tessein, J. A., Ruffolo, D., Matthaeus, W. H., & Wan, M. 2016, Geophysical Research Letters, 43, 3620, doi: [10.1002/2016GL068045](https://doi.org/10.1002/2016GL068045)

Torbert, R. B., Russell, C. T., Magnes, W., et al. 2016, Space Science Reviews, 199, 105, doi: [10.1007/s11214-014-0109-8](https://doi.org/10.1007/s11214-014-0109-8)

Torbert, R. B., Dors, I., Argall, M. R., et al. 2020, Geophysical Research Letters, 47, e2019GL085542, doi: <https://doi.org/10.1029/2019GL085542>

Tsurutani, B. T., & Smith, E. J. 1979, Journal of Geophysical Research: Space Physics, 84, 2773, doi: [10.1029/JA084iA06p02773](https://doi.org/10.1029/JA084iA06p02773)

Valentini, F., Vecchio, A., Donato, S., et al. 2014, The Astrophysical Journal Letters, 788, L16, doi: [10.1088/2041-8205/788/1/L16](https://doi.org/10.1088/2041-8205/788/1/L16)

Vasquez, B. J. 1995, Journal of Geophysical Research, 100, 1779, doi: [10.1029/94ja02724](https://doi.org/10.1029/94ja02724)

Vasquez, B. J., Abramenko, V. I., Haggerty, D. K., & Smith, C. W. 2007, Journal of Geophysical Research: Space Physics, 112, n/a, doi: [10.1029/2007ja012504](https://doi.org/10.1029/2007ja012504)

Velli, M. 1993, Astronomy and Astrophysics, 270, 304. <http://adsabs.harvard.edu/abs/1993A%26A...270..304V>

Velli, M., Grappin, R., & Mangeney, A. 1989, Physical Review Letters, 63, 1807, doi: [10.1103/PhysRevLett.63.1807](https://doi.org/10.1103/PhysRevLett.63.1807)

Veltri, P. 1999, Plasma Physics and Controlled Fusion, 41, A787, doi: [10.1088/0741-3335/41/3a/071](https://doi.org/10.1088/0741-3335/41/3a/071)

Verdini, A., & Velli, M. 2007, The Astrophysical Journal, 662, 669, doi: [10.1086/510710](https://doi.org/10.1086/510710)

Verdini, A., Velli, M., & Buchlin, E. 2009a, The Astrophysical Journal, 700, L39, doi: [10.1088/0004-637x/700/1/139](https://doi.org/10.1088/0004-637x/700/1/139)

Verdini, A., Velli, M., Matthaeus, W. H., Oughton, S., & Dmitruk, P. 2009b, The Astrophysical Journal, 708, L116, doi: [10.1088/2041-8205/708/2/1116](https://doi.org/10.1088/2041-8205/708/2/1116)

Verma, M., Roberts, D., & Goldstein, M. 1995, Journal of Geophysical Research: Space Physics, 100, 19839

Verscharen, D., Klein, K. G., & Maruca, B. A. 2019, arXiv e-prints, arXiv:1902.03448. <https://arxiv.org/abs/1902.03448>

- Wahlström, N., Kok, M., Schön, T. B., & Gustafsson, F. 2013, in 2013 IEEE International Conference on Acoustics, Speech and Signal Processing, 3522–3526, doi: [10.1109/ICASSP.2013.6638313](https://doi.org/10.1109/ICASSP.2013.6638313)
- Wan, M., Matthaeus, W. H., Roytershteyn, V., et al. 2015, Physical Review Letters, 114, 175002, doi: [10.1103/PhysRevLett.114.175002](https://doi.org/10.1103/PhysRevLett.114.175002)
- . 2016, Physics of Plasmas, 23, 042307, doi: [10.1063/1.4945631](https://doi.org/10.1063/1.4945631)
- Wan, M., Matthaeus, W. H., Karimabadi, H., et al. 2012, Phys. Rev. Lett., 109, 195001, doi: [10.1103/PhysRevLett.109.195001](https://doi.org/10.1103/PhysRevLett.109.195001)
- Wang, G., Ye, J. C., Mueller, K., & Fessler, J. A. 2018, IEEE Transactions on Medical Imaging, 37, 1289, doi: [10.1109/TMI.2018.2833635](https://doi.org/10.1109/TMI.2018.2833635)
- Wicks, R., Owens, M. J., & Horbury, T. 2010, Solar Physics, 262, 191, doi: [10.1007/s11207-010-9509-4](https://doi.org/10.1007/s11207-010-9509-4)
- Wilson III, L. B., Brosius, A. L., Gopalswamy, N., et al. 2021, Reviews of Geophysics, 59, e2020RG000714, doi: <https://doi.org/10.1029/2020RG000714>
- Wu, P., Perri, S., Osman, K., et al. 2013, The Astrophysical Journal, 763, L30, doi: [10.1088/2041-8205/763/2/130](https://doi.org/10.1088/2041-8205/763/2/130)
- Yang, Y., Matthaeus, W. H., Parashar, T. N., et al. 2017, Physics of Plasmas, 24, 072306, doi: [10.1063/1.4990421](https://doi.org/10.1063/1.4990421)
- Yordanova, E., Vörös, Z., Varsani, A., et al. 2016, Geophysical Research Letters, 43, 5969, doi: [10.1002/2016gl069191](https://doi.org/10.1002/2016gl069191)
- Zeiler, A., Biskamp, D., Drake, J. F., et al. 2002, Journal of Geophysical Research (Space Physics), 107, 1230, doi: [10.1029/2001JA000287](https://doi.org/10.1029/2001JA000287)

## APPENDIX



## Appendix A

### BRAZIL PLOTS

In Section 2.3 we showed Brazil-plots from dataset `wnd` (Figure 2.4) and `mms` (Figure 2.5). Here we show the Brazil-plot from rest of the datasets mentioned in Chapter 4.

We observe that for 2.5-D simulations because of low values of  $R_p$  and  $\beta_{\parallel p}$ , the instability thresholds are not very well aligned with the distribution of the plasma. However, the plasma in all cases are well confined. For the 3-D case where the propagation vector is not restrained, we do observe a Brazil plot which is very similar to that observed in space plasma data.

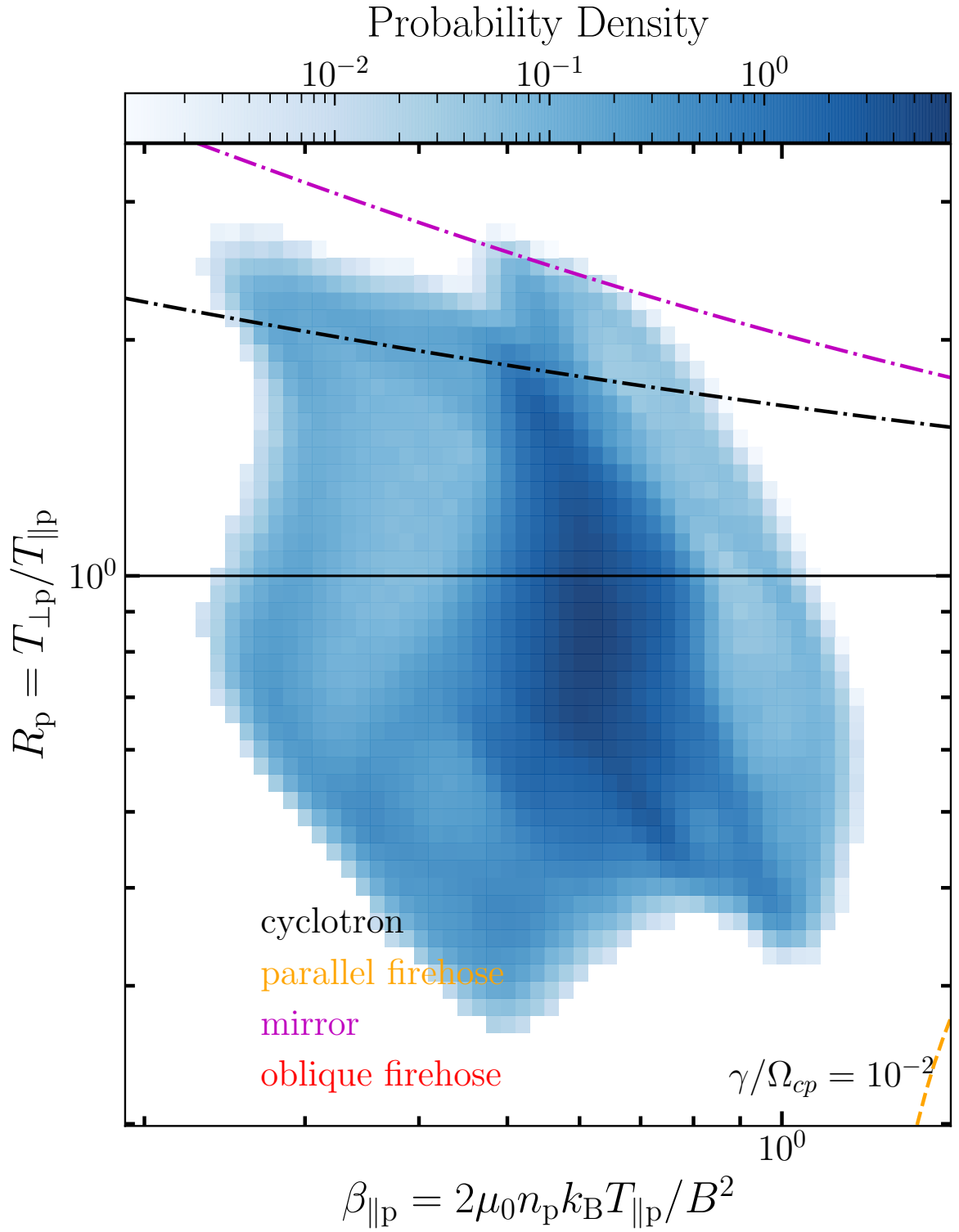


Figure A.1: Plot of estimated probability density,  $\tilde{p}$  of  $(R_p, \beta_{\parallel p})$  for 149p6 dataset and thresholds associated with different instabilities for threshold value of  $\gamma_{\max}/\Omega_{cp} = 10^{-3}$ .

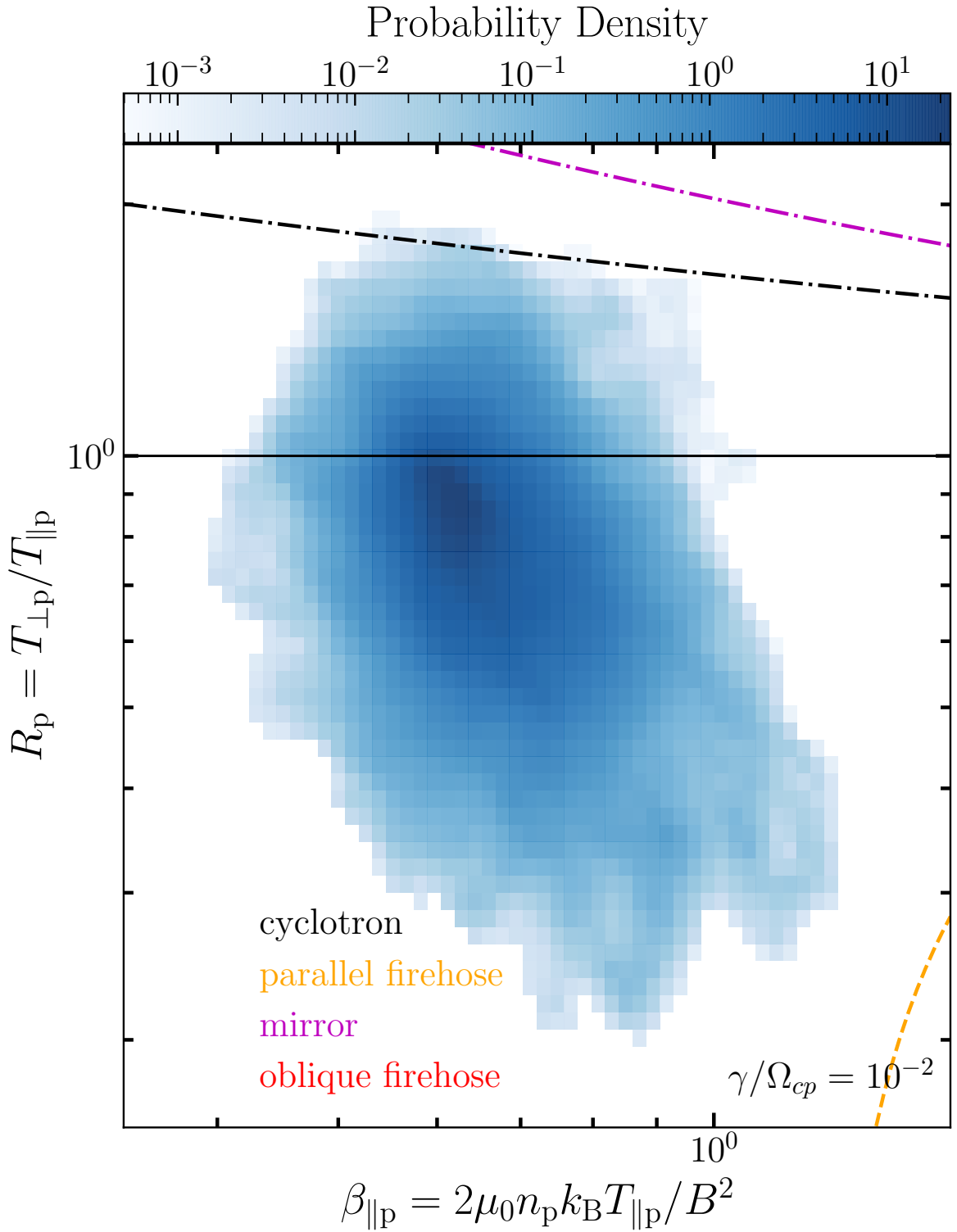


Figure A.2: Plot of estimated probability density,  $\tilde{p}$  of  $(R_p, \beta_{\parallel p})$  for `kaw` dataset and thresholds associated with different instabilities for threshold value of  $\gamma_{\max}/\Omega_{cp} = 10^{-3}$ .

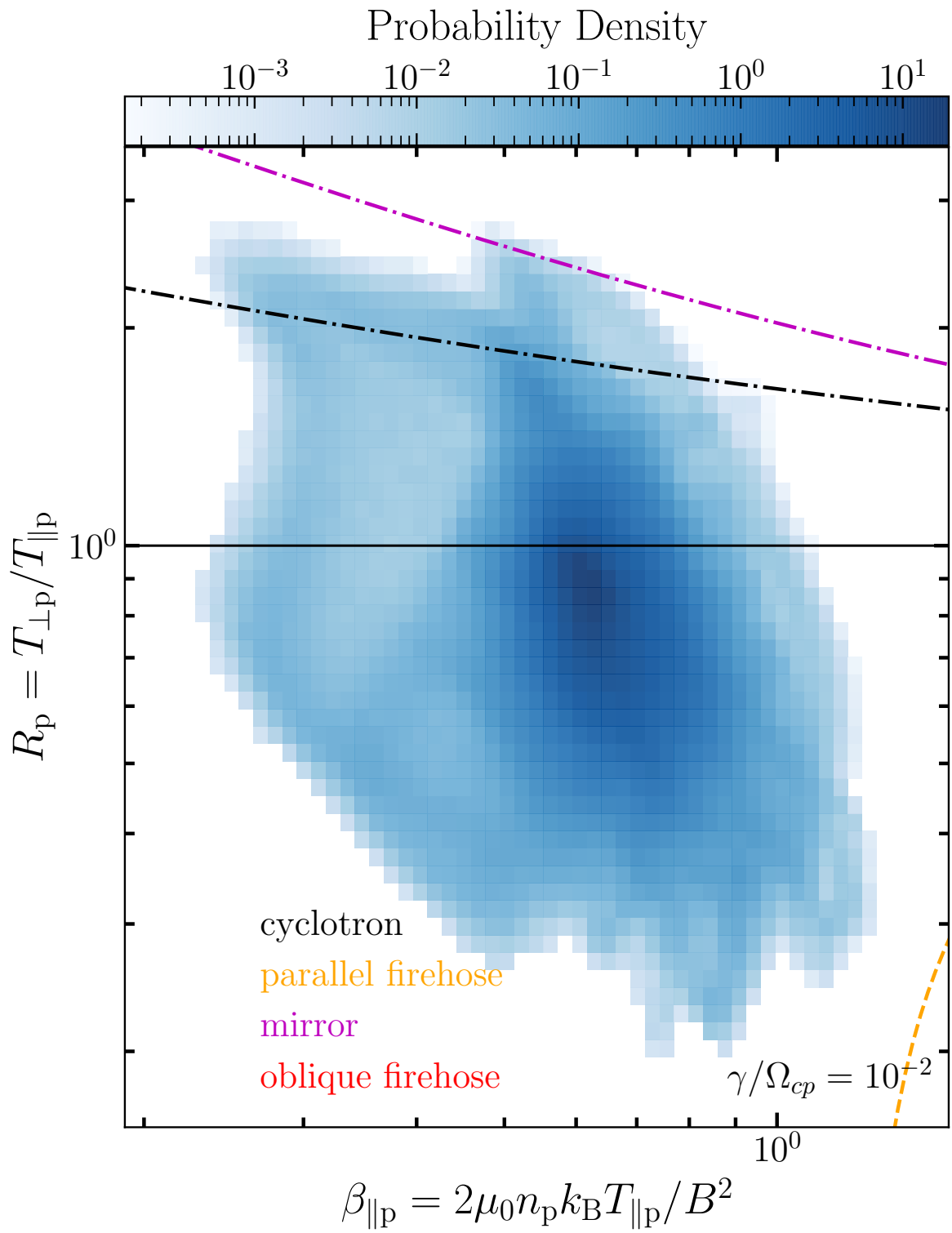


Figure A.3: Plot of estimated probability density,  $\tilde{p}$  of  $(R_p, \beta_{\parallel p})$  for combination of 149p6 and **kaw** dataset and thresholds associated with different instabilities for threshold value of  $\gamma_{\max}/\Omega_{cp} = 10^{-3}$ .

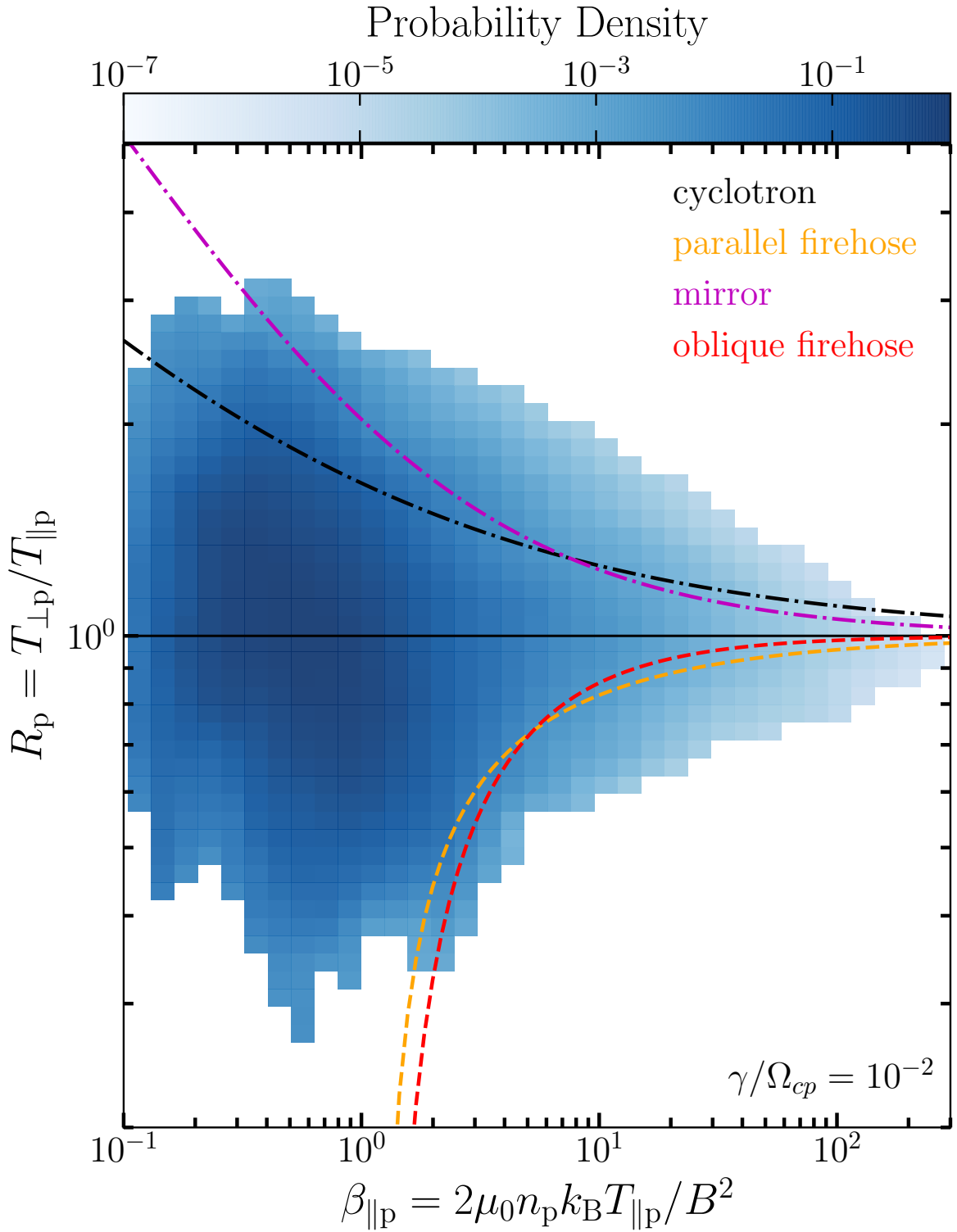


Figure A.4: Plot of estimated probability density,  $\tilde{p}$  of  $(R_p, \beta_{\parallel p})$  for **ros** dataset and thresholds associated with different instabilities for threshold value of  $\gamma_{\max}/\Omega_{cp} = 10^{-1}$ .

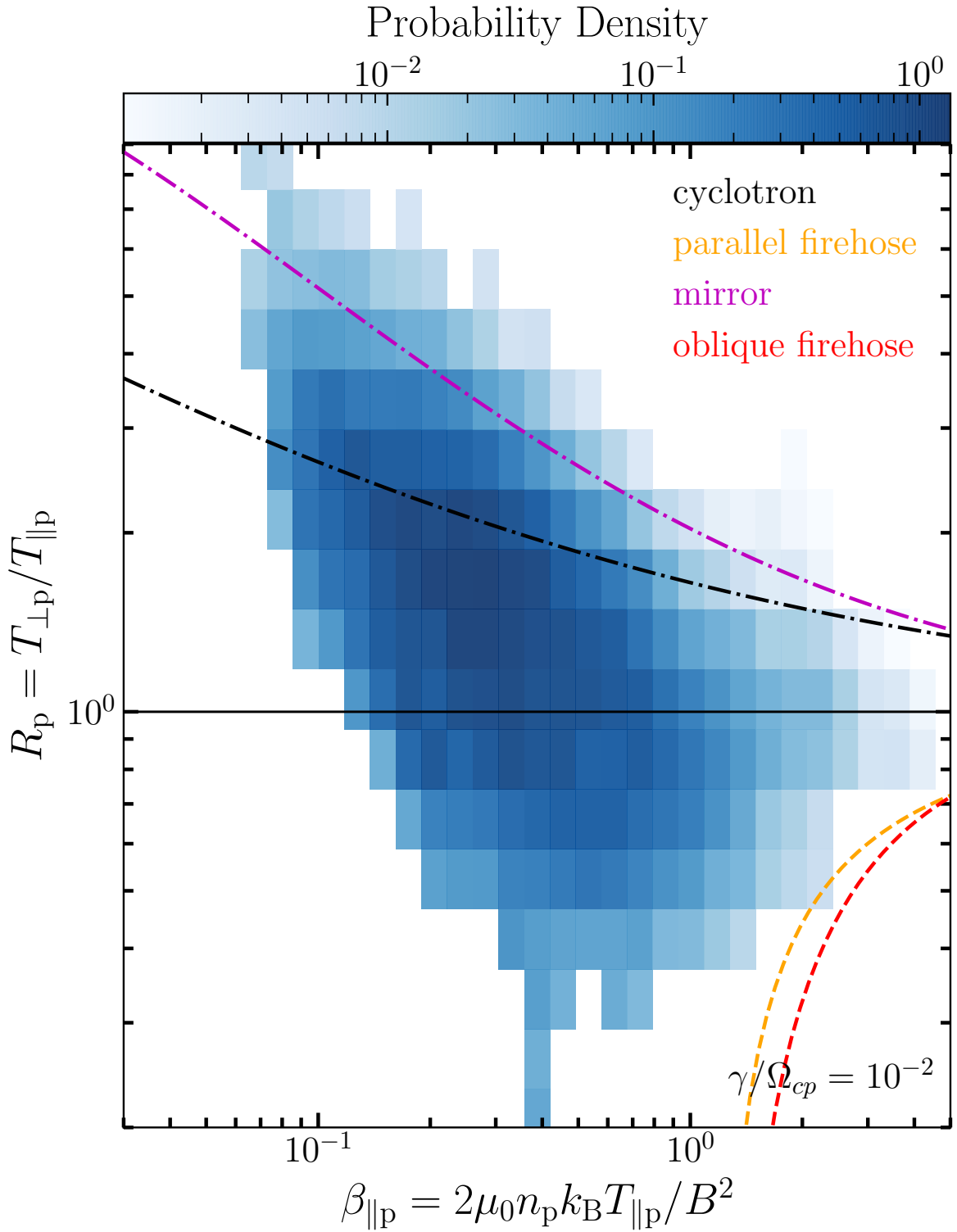


Figure A.5: Plot of estimated probability density,  $\tilde{p}$  of  $(R_p, \beta_{\parallel p})$  for psp dataset and thresholds associated with different instabilities for threshold value of  $\gamma_{\max}/\Omega_{cp} = 10^{-1}$ .

## Appendix B

### CGL INVARIANTS

This appendix details the Chew–Goldberger–Low (CGL) invariants as mentioned in Section 3.2.1.

As mentioned in Section 3.2.1, for a slowly changing magnetic field (compared to the ion gyroscopic time scale) we have conservation of magnetic moment ( $\mu$ ) of the particle and thus we have:

$$\frac{d\mu}{dt} = 0 \quad (\text{B.1})$$

where,  $\mu = m_p w_{\perp p}^2 / (2B)$ ,  $m_p$  is the proton mass,  $w_{\perp p}^2$  is the perpendicular thermal velocity and  $B$  is the magnitude of magnetic field. Writing Equation (B.1) in terms of proton-perpendicular temperature using Equation (2.16), we have:

$$\frac{d}{dt} \left( \frac{k_B T_{\perp p}}{B} \right) = 0 \quad (\text{B.2})$$

or:

$$T_{\perp p} \propto B \quad (\text{B.3})$$

For the parallel case, consider the equation for parallel pressure ( $p_{\parallel}$ ), for which under similar assumptions one can write (Baumjohann & Treumann, 1996):

$$p_{\perp} \frac{dp_{\parallel}}{dt} + 2 p_{\parallel} \frac{dp_{\perp}}{dt} + 5 p_{\perp} p_{\parallel} \nabla \cdot \mathbf{v} = 0 \quad (\text{B.4})$$

Substituting for  $\nabla \cdot \mathbf{v}$  from the continuity equation (Equation (B.5)),

$$\frac{\partial n}{\partial t} + \mathbf{v} \cdot \nabla n + n \nabla \cdot \mathbf{v} = 0 \quad (\text{B.5})$$

and the fact that  $d/dt = \partial/\partial t + \mathbf{v} \cdot \nabla$ , we can rewrite Equation (B.4) as:

$$\frac{d}{dt} \left( \frac{p_{\parallel} p_{\perp}^2}{n^5} \right) = 0 \quad (\text{B.6})$$

or:

$$\frac{d}{dt} \left( \frac{p_{\parallel} B^2}{n^3} \right) = 0 \quad (\text{B.7})$$

which in terms of temperature can be written as:

$$T_{\parallel} \propto (n/B)^2 \quad (\text{B.8})$$

which is same as Equation (3.6).

Equations (B.2) and (B.7) are referred as the *Chew–Goldberger–Low* invariants.

## Appendix C

### GAUSSIAN PROCESSES ALGORITHM

This appendix details the Gaussian Processes Regression followed in Section 8.4. We start with the `ros` dataset. As discussed in Section 4.2.3 the dataset has a resolution of  $2048^3$  cells with a box size of  $\sim 42 d_i$ . Since the resolution of reconstructed image is of the order of  $d_i$ , we decided to downsample the dataset using `block_reduce` in `skimage`. We lowered the resolution to 42 cells along  $x$  and  $y$ -directions, and 128 cells along  $z$ -direction. In units of  $d_i$ , this gives us resolution of  $\sim 0.3 d_i$  in  $z$ -direction and  $1 d_i$  along the other two. The reason for different resolutions is the fact that along  $xy$ -plane, the resolution is limited by the minimum separation between two spacecraft ( $1 d_i$ ), whereas along the  $z$ -direction it is the sampling rate of our instrument which determines the resolution.

Here we list typical values of some of the parameters associated with the simulation and solar wind at 1 au:

$$d_i(1 \text{ au}) \sim 100 \text{ km}$$

$$V_{sw} \sim 500 \text{ km/sec}$$

$$X_{sim}(\text{boxsize}) \sim 40 d_i$$

$$\sim 4 \times 10^3 \text{ km}$$

$$d_{\text{spc}} \sim [1, 11] d_i$$

$$\sim [10^2, 10^3] \text{ km}$$

$$f_{\min} \sim V_{sw}/(2 \times d_{\text{spc},\min})$$

$$\sim 2.5 \text{ Hz}$$

At the assumed solar wind speed of 500 km/s, it takes the spacecraft configuration roughly 10 seconds to cross the whole box. And because of Nyquist criteria, we must have a sampling rate faster than 2.5 Hz. Because of restrictions provided by Nyquist frequency and the box size and because we wanted to have a sample at every plane along the  $z$ -direction, we chose a sampling frequency of 40 Hz. This is easily achievable for modern day magnetometers (Bale et al., 2016; Russell et al., 2016).

Once we have the sampling rate and the spacecraft configuration fixed, we virtually fly through the simulation box and collect data for each spacecraft. At the end of simulated flight we have  $n_{\text{spc}}$  (number of spacecraft) number of data points for each plane and thus  $128 \times n_{\text{spc}}$  total data points along with their positions. We then define a kernel and associated variables as:

```
pln = 'xy'
drn = 'z'
ck_len = 5
mat_len_scl = [2,2,6]
mat_nu = 5/2
sigma_0 = 0
n_restarts_optimizer = 20
kernel = CK(ck_len, (1e-2, 1e2)) + CK(ck_len, (1e-2, 1e2)) *
    Matern(length_scale=mat_len_scl, nu=mat_nu)
```

we then run the Gaussian Processes with the selected kernel:

```
gp = GaussianProcessRegressor(kernel=kernel,
    n_restarts_optimizer=n_restarts_optimizer)
```

We can then get the model based on the data collected by the spacecraft:

```
gp.fit(X, y)
```

and then provide `gp.fit` with the coordinate of all the locations at which we want

to find the value of the field:

```
y_pred, mse_pred = gp.predict(x1x2x3, return_std=True)
```

and reshape the output get the final value of field at each point:

```
Zp = np.reshape(y_pred,(indx_max - indx_min + 1,
                      indy_max - indy_min + 1, indz_max - indz_min + 1, 3))
MSE = np.reshape(mse_pred,(indx_max - indx_min + 1,
                           indy_max - indy_min + 1, indz_max - indz_min + 1))
```

Zp is the output that we have plotted in Figures 8.2 to 8.9.

## Appendix D

### PERMISSION LETTER

Permission letter from the Physical Science Publication for Figures 5.1, 5.6, 6.2, 6.3 and 6.5.

7/21/2021 University of Delaware Mail - Permission to use figures from articles!

 Ramiz Qudsi <ahmadr@udel.edu>

---

**Permission to use figures from articles!**  
2 messages

**Ramiz Qudsi** <ahmadr@udel.edu>  
To: rights@aip.org  
Tue, Jul 13, 2021 at 5:24 PM

Dear Sir/Ma'am,

I wanted to use a few figures in my PhD thesis from two of my published articles in both of which I am the first author. I have listed them below:

**Article citation:** R. A. Qudsi et al 2020 ApJS 246 46  
**Title:** Observations of Heating along Intermittent Structures in the Inner Heliosphere from PSP Data  
**Author:** Ramiz A. Qudsi  
**Journal:** The Astrophysical Journal Supplement Series, Volume 246, Number 2  
**Permission to use figures:** Figure 1, Figure 2 and Figure 3

**Article citation:** Ramiz A. Qudsi et al 2020 ApJ 895 83  
**Title:** Intermittency and Ion Temperature-Anisotropy Instabilities: Simulation and Magnetosheath Observation  
**Author:** Ramiz A. Qudsi  
**Journal:** The Astrophysical Journal, Volume 895, Number 2  
**Permission to use figures:** Figure 1 and Figure 3.

Thesis will be published online on my University's Library's website by the end of August, 2021.

--

Regards

Ramiz A. Qudsi  
Department of Physics and Astronomy  
University of Delaware  
Newark, DE-19716  
Ph: (302) 831-6277

---

AIPRights Permissions <Rights@aip.org>  
To: Ramiz Qudsi <ahmadr@udel.edu>  
Wed, Jul 21, 2021 at 1:54 PM

Dear Dr. Qudsi:

You are permitted to include material from your published article in your thesis, provided you also include a credit line referencing the original publication.

Our preferred format is (please fill in the citation information):

"Reproduced from [FULL CITATION], with the permission of AIP Publishing."

If the thesis will be available electronically, please include a link to the version of record on AIP Publishing's site.

Please let us know if you have any questions.

Sincerely,

<https://mail.google.com/mail/u/1/?ik=617bf2dfa0&view=pt&search=all&permthid=thread-a%3Ar3864515244625312975&simpl=msg-a%3Ar3386034054...> 1/2